



Norwegian University of  
Science and Technology

# Numerical Simulations of Shell-Side Two-Phase Flow in Spiral-Wound Heat Exchanger

for Natural Gas Liquefaction

**Dan-Hermann S Thue**

Master of Science in Mechanical Engineering

Submission date: December 2015

Supervisor: Trygve Magne Eikevik, EPT

Norwegian University of Science and Technology  
Department of Energy and Process Engineering



EPT-P-2015-12



**MASTER THESIS**

for

Dan-Hermann Schmeling Thue

Autumn 2015

*Numerical simulations of shell-side two-phase flow in spiral wound heat  
exchanger for natural gas liquefaction*

*Strømningsmodeller av skall-siden i en*

*Spiral-tvunnet varmeveksler for produksjon av  
flytende naturgass*

**Background and objective**

When remote and small scale gas fields are to be exploited, liquefied natural gas (LNG) is a major solution to the problem of transportation, as opposed to using pipelines. LNG also has a transportation cost advantage over long distances compared to pipelines. The global demand for LNG is expected to rise in the following years, especially in Asia, which increases the importance of researching the liquefaction process. One of the most critical components of the process is the spiral wound heat exchanger (SWHE). However, little research about the design basis of the SWHE is openly available as there are few manufacturers. Especially on the shell-side.

The objective of this thesis is concentrated on making use of a simulation model approach of the falling film flow on the shell-side of the heat exchanger using ANSYS software. In the two-phase flow, the mass flow rate, the different velocities of liquid and gas and the vapor fraction can be measured to see how it influences the flow pattern.

**The following tasks are to be considered:**

1. Literature study of spiral wound heat exchangers and the cryogenic liquefaction section of liquefying natural gas using a mixed refrigerant
2. Create and simulate a simplified 3D model of the SWHE
3. Test the 3D model under different vapor fractions and flow rates and then check influence on flow patterns
4. Compare results of measured void fractions with the best prediction model available
5. Compare flow pattern results with the lab experiment
6. Proposal of further work

-- “ --

The project work comprises 15 ECTS credits.

The work shall be edited as a scientific report, including a table of contents, a summary in Norwegian, conclusion, an index of literature etc. When writing the report, the candidate must emphasize a clearly arranged and well-written text. To facilitate the reading of the report, it is important that references for corresponding text, tables and figures are clearly stated both places.

By the evaluation of the work the following will be greatly emphasized: The results should be thoroughly treated, presented in clearly arranged tables and/or graphics and discussed in detail.

The candidate is responsible for keeping contact with the subject teacher and teaching supervisors.

Risk assessment of the candidate's work shall be carried out according to the department's procedures. The risk assessment must be documented and included as part of the final report. Events related to the candidate's work adversely affecting the health, safety or security, must be documented and included as part of the final report. If the documentation on risk assessment represents a large number of pages, the full version is to be submitted electronically to the supervisor and an excerpt is included in the report.

According to “Utfyllende regler til studieforskriften for teknologistudiet/sivilingeniørstudiet ved NTNU” § 20, the Department of Energy and Process Engineering reserves all rights to use the results and data for lectures, research and future publications.

The report shall be submitted to the department in 3 complete, bound copies.

An executive summary of the thesis including title, student's name, supervisor's name, year, department name, and NTNU's logo and name, shall be submitted to the department as a separate pdf file. The final report in Word and PDF format, scientific paper and all other

material and documents should be given to the academic supervisor in digital format on a DVD/CD-rom or a memory stick at the time of delivery of the project report.

Submission deadline: *January 19, 2016.*

Work to be done in lab (Water power lab, Fluids engineering lab, Thermal engineering lab)

Field work

Department for Energy and Process Engineering, 22 August 2014.

---

Prof. Olav Bolland

Department Head

---

Prof Trygve M. Eikevik

Academic Supervisor

e-mail: [Trygve.m.eikevik@ntnu.no](mailto:Trygve.m.eikevik@ntnu.no)

Research Advisor(s):

e-mails

Prof. G.L. Ding (SJTU)

[glding@sjtu.edu.cn](mailto:glding@sjtu.edu.cn)

Prof Trygve M. Eikevik (NTNU)

[Trygve.m.eikevik@ntnu.no](mailto:Trygve.m.eikevik@ntnu.no)

N.N

## **Preface**

The program is a joint-research venture collaboration between The Norwegian University of Science and Technology (NTNU) and Shanghai Jiao Tong University (SJTU). This thesis was written at SJTU and results in a degree from both universities. The dissertation topic is issued by Institute of Refrigeration and Cryogenics and the period of the project spans from September 2014 to December 2015. Professor 丁国良 (Ding GuoLiang) is the academic supervisor from SJTU and Professor Trygve Magne Eikevik is the supervisor from NTNU. Lab experiments were sponsored by Chinese National Offshore Oil Corporation (CNOOC). I also want to thank DingChao and LiJanRui for the theoretical discussions and support in the matters Chinese.

Dan-Hermann Thue

Shanghai, Dec. 2015

## Abstract

Heat transfer coefficients and pressure drop of evaporating heat exchangers such as the spiral wound heat exchanger depend on the distribution of the refrigerant fluid. However little open research is available in the study of Spiral wound heat exchangers (SWHE) flow for LNG liquefaction. Only a handful of producers have the most experience in the production of such heat exchangers. The number of studies on two-phase liquid-gas flows on shell side of heat exchangers are still limited compared to in tube two phase flows. Most studies already done have focused on air water mixtures and some CFC refrigerants, which are now banned in most countries. In addition, the most commonly covered mass flows are in a larger range than typically used in refrigeration systems, in which typical systems use a range of 5 to 60 kg/m<sup>2</sup>s.

A method of flow patterns study of two phase liquid-gas flow over a horizontal tube bundle has been developed. The tube bundle is comparable, although simplified, to the geometry in the spiral wound heat exchanger tested in the laboratory at Shanghai Jiao Tong University. Liquid-vapor two-phase shell side flow phenomena is simulated in 3D using ANSYS ICEM for meshing, Fluent for calculations and CFD-Post data accumulation software. Flow patterns and data are observed mainly at vapor qualities between 0.1 and 0.7 and mass flux range of 10 – 50 kg/m<sup>2</sup>s.

A method for measuring void fractions is established and then compared according to established theory. The Feenstra-Weaver-Judd method is so far the most advanced prediction model and the best fitting for the largest part of the range studied. The higher the mass flux and vapor quality the better the prediction is compared to the model.

A close relationship between void fraction, and transition to new flow patterns was discovered. Especially in differences between spray flow and falling film flow.

The measured void fractions were found to vary when increasing the vertical distance of the tubes. When increasing from 1mm to 4mm at a constant mass flux, the void fractions were consistently higher and the transition to a new flow regime thus came faster and at a lower vapor quality.

The model is compared against the findings of the laboratory test at SJTU with propane, and the correlation of flow patterns fit well with the simulations.

The CFD models flow pattern results were compared to results from lab experiments. The geometry in the CFD model is simplified compared to the SWHE model in the lab. Despite this there was good agreement with the flow pattern findings between simulation and lab results.

Different fluids and geometries can be tested using this model. In this report, Propane was used as refrigerant fluid and material properties were obtained using REFPROP software at saturation point for 0.3 MPa.

## Sammendrag

Studien av 2-fase strømningsmønstre i skall siden av spiral-tvunnede varmevekslere har stor betydning for virkningsgraden, varmeoverføringen og trykktapet. Lite åpen forskning er tilgjengelig på området ettersom det er få aktører på markedet som produserer slike varmevekslere. Antallet to-fase studier gjort på skall siden av varmevekslere er svært få til sammenlikning med studier på strømning i rør. I tillegg er de fleste eksisterende studier fokusert på vann-luft blandinger og har ofte massestrømmer utenfor det området som er aktuelt for SWHE for LNG produksjon, nemlig mellom 5 – 60 kg/m<sup>2</sup>.s.

Det ble utviklet en metode for å studere vertikal strømningsmodus til to-fase strømning med Propan over en horisontal rørbunt, som ofte er å finne i varmevekslere. Geometrien til denne rørbunten er liknende geometrien til en modell av en SWHE som testes i laboratoriet ved Shanghai Jiao Tong Universitetet under liknende tilstander.

En sammenlikning ble ført mellom lab-testene og simuleringene. Det ble funnet god overensstemmelse hva gjelder strømningskart og strømningsmoduser ved de aktuelle massefluksene og gasskvalitetene.

Simuleringsmetoden ble utviklet som en del av oppgaven og under veiledning fra SJTU. ANSYS programvare ble benyttet, ICEM for å lage mesh, Fluent for å beregne og CFD Post for å behandle data.

Simuleringen er gjort i 3D ved bestemte verdier for gasskvalitet og massestrøm. Massestrømmen varierte mellom 10 – 50 kg/m<sup>2</sup>.s og gass kvaliteten mellom 0.1 og 0.7. Propan ved 3 bar fordampningstemperatur er benyttet og termodynamiske data hentet fra REFPROP programvare.

Data lest fra målingene var gass-volumfraksjonen og arealfraksjonen i bestemte utsnitt i 3D modellen, samt individuelle gass og væske hastigheter ved nevnte utsnitt. Dette ble brukt til sammenlikning med teoretiske prediksjonsmetoder utarbeidet av tidligere forskere. Feenstra-Weaver-Judd modellen viste seg å være den mest nøyaktige prediksjonsmodellen, men hadde problemer ved samtidig lave massestrømmer og gasskvaliteter. Nøyaktigheten økte ved økning av disse parameterne.

Gassvolumfraksjonen økte når den vertikale distansen mellom rørene ble økt. Tester mellom 1mm, 2mm og 4mm vertikal distanse ble simulert.

Simuleringsmodellens strømningsmønstre ble sammenliknet med strømningsmønstrene observert ved lab forsøk ved SJTU. Det ble funnet god overensstemmelse med resultatene for disse. Propan ble brukt ved simulering og lab sammenlikning. Simuleringsmodellen er en forenklet modell av lab modellen.

Denne simuleringsmetoden kan dermed være svært nyttig for å simulere forskjellige to-fase blandinger på skall siden over rør bunter og kan testes for forskjellige geometrier hurtig og effektivt sammen.

## Table of Contents

Preface .....	I
Abstract .....	II
Sammendrag .....	III
1. Background and Motivation.....	2
1.1 Liquid Natural Gas (LNG) .....	2
1.2 LNG status 2014 .....	3
1.3 LNG Prospects 2014-2016.....	4
1.4 Spiral wound heat exchanger (SWHE).....	6
1.5 Dimensions of SWHE .....	8
1.6 LNG liquefaction cycles.....	9
1.6.1 APCI propane precooled mixed refrigerant process .....	9
1.6.2 Philips optimized cascade LNG process.....	9
1.6.3 PRICO process .....	10
1.6.4 Statoil/Linde mixed fluid cascade process .....	10
2. Literature Review: State of the Art.....	10
2.1 Flowrate, Film flowrate and Reynolds number .....	11
2.2 Falling film flow over open horizontal tubes .....	11
2.3 Capillary influence and surface tension .....	13
2.4 Falling flow over Horizontal tube bundles.....	14
2.4.1 Flow Pattern estimations.....	14
2.4.1 Void fractions .....	16
2.5 Horizontal tube CFD simulations .....	21
2.6 Falling flow in SWHE .....	22
2.7 Flow patterns influence on heat transfer .....	23
2.7.1 Factors influencing the heat transfer coefficient .....	25

3.	CFD model setup .....	26
3.1	CFD Governing Equations .....	26
3.1.1	Continuity equations .....	26
3.1.2	Momentum equation .....	26
3.1.3	Surface tension .....	27
3.1.4	Material properties .....	27
3.1.5	Energy Equation .....	27
3.2	2D and 3D models .....	27
3.3	Geometry .....	28
3.4	Meshing .....	30
3.5	Fluent solver solution setup.....	31
3.6	Solution Models .....	32
3.6.1	Multiphase flow simulation: The volume of fluid model (VOF).....	32
3.6.2	Viscous and turbulence model: Shear stress transport (SST) k- $\omega$ .....	33
3.6.3	Energy equation.....	34
3.7	Materials and phases.....	34
3.7.1	Materials .....	34
3.7.2	Phases.....	35
3.8	Boundary conditions.....	35
3.8.1	Inlet .....	35
3.8.2	Outlet.....	36
3.8.3	Tube walls.....	36
3.8.1	Left and right sides.....	36
3.8.2	Front and back sides.....	36
3.9	Solution Methods:.....	36
3.10	Calculation Activities .....	37
4.	Methodology .....	38

4.1	Determining the inlet void fraction.....	38
4.2	Determining Inlet vapor and liquid velocities.....	38
4.2.1	Variables .....	39
4.3	Test for Mesh independent solution .....	39
4.3.1	Operating conditions .....	40
4.3.2	Quality 0.1 .....	40
4.3.3	Quality 0.3 .....	42
4.3.3.1	Coarse mesh:.....	42
4.4	Verifying Mass flow integrity of simulations .....	44
4.5	Extracting measurements on the simulation models .....	45
5.	Results and Discussion .....	46
5.1	Flow patterns.....	46
5.1.1	Capillary length influence: .....	48
5.1.2	Droplet flow with water-air Simulation.....	48
5.2	Slip ratio results .....	51
5.3	Void fraction results .....	52
5.3.1	Shear flow results $0.9 \leq \epsilon \leq 1$ .....	54
5.3.2	Intermittent flow/transition flow regimes $0.75 \leq \epsilon \leq 0.9$ .....	55
5.3.3	Falling film flow regime $\epsilon \leq 0.80$ .....	56
5.4	Comparison with Void fraction prediction models .....	58
5.5	Results from 4mm tube gap .....	62
5.6	Comparison with results from laboratory experiment.....	64
5.7	Sources of error .....	65
5.7.1	CFD Model .....	65
6.	Conclusions.....	66
7.	Recommendations for future work .....	67
	References .....	68

## Table of Figures

FIGURE 1-1 NATURAL GAS MAJOR TRADE MOVEMENTS 2012 (CHEN, 2014) .....	3
FIGURE 1-2 TRADE BALANCE IN GLOBAL MARKETS OF LNG IN MEGATONNES BETWEEN 2013 AND 2014. (BG-GROUP, 2014).....	4
FIGURE 1-3- PRICE DEVELOPMENT AND PREDICTIONS OF MAJOR LNG REGIONAL MARKETS.(BG-GROUP, 2014).	5
FIGURE 1-4 PRODUCTION STEPS OF CWHE.....	7
FIGURE 1-5 MUTISTREAM SWHE .....	8
FIGURE 1-6 CROSS SECTION ILLUSTRATING THE INNARDS OF AN SWHE .....	8
FIGURE 2-1 – SIMPLIFIED MODEL OF FALLING FILM FLOW (FERNÁNDEZ-SEARA AND PARDIÑAS, 2014) (HALF TUBE).....	11
FIGURE 2-2 MITROVIC, J. INFLUENCE OF TUBE SPACING AND FLOW RATE ON HEAT TRANSFER FROM A HORIZONTAL TUBE TO A FALLING LIQUID FILM. (MITROVIC, 1986) .....	12
FIGURE 2-3 - FLOW MODE TRANSITIONS WHEN NEGLECTING HYSTERESIS (HU AND JACOBI, 1996) .....	13
FIGURE 2-4 – FLOW REGIME MAP DEVELOPED BY (NOGHREHKAR ET AL., 1999) FOR A) IN-LINE TUBE ARRANGEMENT AND B) STAGGERED . VERTICAL UPWARD FLOW ACROSS TUBE BUNDLES WITH AN AIR-WATER TWO PHASE FLOW.....	15
FIGURE 2-5 -- FLOW PATTERNS IN VERTICAL DOWN-FLOW ACROSS A HORIZONTAL TUBE BUNDLE: (A) FALLING FILM FLOW; (B) INTERMITTENT FLOW; (C) ANNULAR FLOW; (D) BUBBLY FLOW (XU ET AL., 1998) .....	16
FIGURE 2-6 COMPARISON OF DIFFERENT VOID FRACTION PREDICION MODELS IN HORIZONTAL FLOW SHELL SIDE TUBE BUNDLE FLOW, BY (JOHN R. THOME, 2010).....	19
FIGURE 2-7 EXPERIMENTAL RESULTS FROM (XU ET AL., 1998) DOWNWARD FLOW WITH AIR-WATER. IN LINE SQUARE ARRANGEMENT WITH A PITCH TO DIAMETER RATIO OF 1.28 VOID FRACTION MEASURED IS VOLUMETRIC. ....	20
FIGURE 2-8- 3 TUBE HORIZONTAL TUBES MODEL WITH DOWNWARD FLUID FLOW, CUT ALONG THE MIDDLE AND MIRRORED ALONG THE VERTICAL AXIS.....	21
FIGURE 2-9 – WU ET AL. MODEL OF SWHE.....	22
FIGURE 2-10 – FLOW MAP OF FALLING FILM FLOW: (FF) FILM FLOW; (IN) INTERMITTENT (XU ET AL., 1998) .....	23
FIGURE 3-1- INVENTOR SKETCHES (X-Y-PLANE) OF THE 1MM AND 4 MM VERTICAL TUBE SPACING MODEL GEOMETRIES. FOR 3D MODELLING AN EXTRUSION OF 10MM DEPTH IS USED IN BOTH CASES. ....	29
FIGURE 3-2- ILLUSTRATION OF WHAT THE TUBE BUNDLES LOOK LIKE WITH ALL DIMENSIONS FROM TABLE 1 INCLUDED. ....	29
FIGURE 3-3- .....	30
FIGURE 3-4 – MESH OF TUBE BUNDLE MODEL WITH 3 TUBES. LEFT: 1MM VERTICAL TUBE GAP (P/D=1.08). RIGHT: 4MM VERTICAL TUBE GAP (P/D) 1.33. ....	31
FIGURE 3-5 – OVERVIEW OF THE SOFTWARE USED IN ANSYS WORKBENCH, FROM LEFT ICEM CFD, FLUENT AND CFD POST. ....	32

FIGURE 3-6 -- VOF MODELLING OF A FLUID-FLUID SURFACE (A) REPRESENTS THE REAL SURFACE, (B) THE VOLUME FRACTION CALCULATED BY THE VOF MODEL AND (C) IS THE VOF MODELS LINEAR RECONSTRUCTION OF THE SURFACE.....	33
FIGURE 3-7 BOUNDARY LAYER IN THE MIDDLE AND TUBE INTERIOR AT LEFT. EXTRA FINE MESH DENSITY. RED LAYER IS LIQUID. BOUNDARY LAYER THICKNESS MODELED AT 0.2MM.....	34
FIGURE 3-8 SOLUTION METHODS USED FOR SIMULATIONS .....	37
FIGURE 4-1 -- COMPARISON OF MESH SOLUTIONS FOR VAPOR QUALITY $X=0.1$ . FROM TOP: COARSE MESH, MEDIUM MESH AND FINE MESH. AT THE RIGHT SIDE, A ZOOMED PERSPECTIVE OF THE OUTLET IS SHOWN.....	41
FIGURE 4-2 A) COARSE MESH AT 0.4 SECONDS B) MEDIUM MESH AT 0.4S.....	42
FIGURE 4-3 – FINE MESH SOLUTION AT SEEN FROM FRONT AT TIME 0.4 SECONDS (LEFT), AND SEEN FROM THE BACK SIDE AT 0.6 SECONDS WHEN ONE SIDE HAS BECOME ALMOST SYMMETRICAL IN THE X-Y PLANE(RIGHT).....	43
FIGURE 4-4 -- EXTRA FINE MESH AT 0.4S TWIST PHENOMENA OCCURRING.....	43
FIGURE 4-5 – MEASUREMENT LOCATIONS OF VAPOR AND LIQUID VELOCITIES AND AREA FRACTIONS USED TO CALCULATE SUPERFICIAL VELOCITIES. BLACK CUT PLANE AND PURPLE CUT PLANE WAS USED AND AVERAGED. QUALITY $X_0.1$ AND FLOWRATE G30 USED AS EXAMPLE HERE. ....	46
FIGURE 5-1 FLOW MAP INDICATING FLOW MODE TRANSITIONS BASED ON VAPOR QUALITY AND MASS FLUX OVER THE IN LINE TUBE BUNDLE WITH 1MM VERTICAL TUBE SPACING. ....	47
FIGURE 5-2 – WATER AIR SIMULATION DO INDUCE DROPLET FLOW. $X=0.0001$ AND $G=0.75$ $KG/M^2S$ . $RE_L = 25$ ..	48
FIGURE 5-3: ATTEMPT TO HAVE WETTED TUBE WALLS AND DROPLET FLOW. $X=0.0001$ AND $G=1.75$ . $RE_L = 50$ 50	
FIGURE 5-4 SLIP FACTORS S FOR ALL 1MM VERTICAL TUBE GAP SIMULATIONS ARRANGED AFTER MEASURED VOLUMETRIC VOID FRACTIONS.....	52
FIGURE 5-5 – VOLUMETRIC VOID FRACTION MEASUREMENTS FOR 1MM VERTICAL TUBE SPACING CASE .....	53
FIGURE 5-6 – FILM THICKNESS MEASURED AT THE LOWEST TUBE AT THE THINNEST CROSS SECTIONAL AREA AND WHERE THE VELOCITY AND THUS FILM THICKNESS WERE USUALLY THINNEST. MEASUREMENTS FOR 1MM VERTICAL TUBE SPACING CASE.....	54
FIGURE 5-7 – SHEAR FLOW CASE EXAMPLE. SIMULATION VAPOR QUALITY $X = 0.7$ AND MASS FLOWRATE $G = 40$ $KG/M^2S$ .....	55
FIGURE 5-8 – QUALITY 0.7 MASS FLUX 20 $KG/M^2S$ – LIQUID FILM THICKNESS IS VERY LOW ON THE SIDES BUT LIQUID AGGREGATES BETWEEN THE TUBES IN A LARGER DEGREE. OCCASIONAL DRY SPOTS ON THE LOWER TUBE. ....	56
FIGURE 5-9 – A) AND B) FALLING FILM FLOW REGIME $G 30$ $KG/M^2S$ AND QUALITY $X = 0.1$ . C) COMPARED TO INTERMITTENT FLOW REGIME WITH HIGH GAS VELOCITIES REPRESENTED BY $G 20$ $KG/M^2S$ $X = 0.7$ .....	57
FIGURE 5-10 FALLING FILM FLOW. $G50$ AND $X0.1$ TOP FRONT AND SIDE VIEW AT $T=0.66S$ .....	58
FIGURE 5-11 - COMPARISONS OF VOID FRACTION PREDICTION METHODS FOR 1MM TUBE GAP CASE, BLACK LINES AND POINTS ARE RESULTS OBTAINED FROM SIMULATIONS COLORED ARE ESTIMATIONS: .....	59

FIGURE 5-13 COMPARISON OF VOID FRACTION PREDICTION METHODS FOR 4MM TUBE GAP CASE .....	63
FIGURE 5-14 A COMPARISON OF THE FLOW MODES OBSERVED AT SPECIFIC VAPOR QUALITIES AND MASS FLUXES. THE 1MM VERTICAL TUBE GAP SIMULATIONS FIT WELL WITH THE 2MM LAB EXPERIMENT OBSERVATIONS.....	64
FIGURE 5-15 – LEFT: FALLING FILM FLOW AND RIGHT: INTERMITTENT FLOW. PROPANE AT 4.5 BAR FROM OBSERVATIONS AT THE LAB SET UP IN SJTU. ....	65

## TABLES

TABLE 2-1. OVERVIEW OF PARAMETERS INFLUENCING THE HEAT TRANSFER COEFFICIENT, TABLE AND CONTENT CREDIT TO MASTER THESIS OF (JOHN G. BUSTAMENTE, 2014) .....	26
TABLE 3-1 MODEL GEOMETRIES .....	28
TABLE 3-2 SATURATION POINTS AT EQUILIBRIUM FOR PROPANE FROM 0.1MPA TO 1MPA, GENERATED USING REFPROP COMPUTER SOFTWARE.- NIST REFERENCE FLUID PROPERTIES.....	35
TABLE 5-1 – RESULTS AND PREDICTIONS OF VELOCITY RATIOS/SLIP RATIOS IN THE SIMULATED RANGE. FLOW MODES MARKED WITH DIFFERENT COLORS: GREEN FIELDS ARE FF, ORANGE FIELDS ARE TRANSITION AREA (IN), AND RED IS SPRAY FLOW (SH).....	51
TABLE 5-2 – VOID FRACTION MEASUREMENT RESULTS .....	52
TABLE 5-3 PERCENTAGE DIFFERENCE BETWEEN MEASURED VOLUMETRIC VOID FRACTIONS AND THE FEENSTRA-WEAVER-JUDD PREDICTION MODEL. ....	59

## NOMENCLATURE

$A$	Total cross sectional area,	$[m^2]$
$\alpha_l$	Volume fraction liquid phase,	dimensionless
$\alpha_v$	Volume fraction vapor phase,	dimensionless
$D$	Tube Diameter,	$[m]$
$E$	Energy,	$[J]$
$\varepsilon$	Void fraction, dimensionless,	$[Vol\ gas/total\ vol]$
$F_r$	Froude number	dimensionless
$G$	Mass flux,	$[kg/sm^2]$
$k_{eff}$	Effective thermal conductivity	$[W/m.K]$

$\dot{m}$	Mass flow rate	$[kg/s]$
$P$	Pitch of tubes (vertical distance between tube centers)	$[m]$
$p$	Pressure,	$[N/m^2]$
$\rho$	Density,	$[kg/m^3]$
$\rho_v$	Density vapor phase,	$[kg/m^3]$
$\rho_l$	Density liquid phase,	$[kg/m^3]$
$Q$	Volumetric flowrate,	$[m^3/s]$
$Ri$	Richardson number,	dimensionless
$S$	Slip factor, dimensionless,	$[U_{GS}/U_{LS}]$
$S_h$	Source term (containing radiation)	
$T$	Temperature,	$[K]$
$u$	Velocity,	$[m/s]$
$U_{vs}$	Superficial velocity gas, $(U_{vs} = u_v \epsilon)$	$[m/s]$
$U_{ls}$	Superficial liquid velocity, $(U_{ls} = u_l(1 - \epsilon))$	$[m/s]$
$X$	Vapor fraction / Vapor quality,	dimensionless

## ABBREVIATIONS AND SUBSCRIPTS

CNG	-	Compressed Natural Gas
FLNG	-	Floating liquefied natural gas facilities
FSRU	-	Floating storage and regasification unit
GS	-	Gas Superficial
LNG	-	Liquid Natural Gas
Mtpa	-	Megatonnes or million tonnes per annum
NG	-	Natural gas
SWHE	-	Spiral Wound Heat Exchanger

- UDF - User defined function
- VOF - Volume of fluid method (in fluent)

# **1. Background and Motivation**

## **1.1 Liquid Natural Gas (LNG)**

LNG is a means for storage and transportation of natural gas. The natural gas is cooled down to about  $-162^{\circ}\text{C}$  and condenses to liquid at atmospheric pressure. At this state the NG is reduced in volume some 600 times compared to normal state conditions. The alternatives for LNG are compressed natural gas (CNG) or transport through pipelines. However a pipeline requires a more stable customer and supplier relationship and is a less flexible solution to the transportation problem of gas. In addition, many countries lack a developed pipeline distribution system.

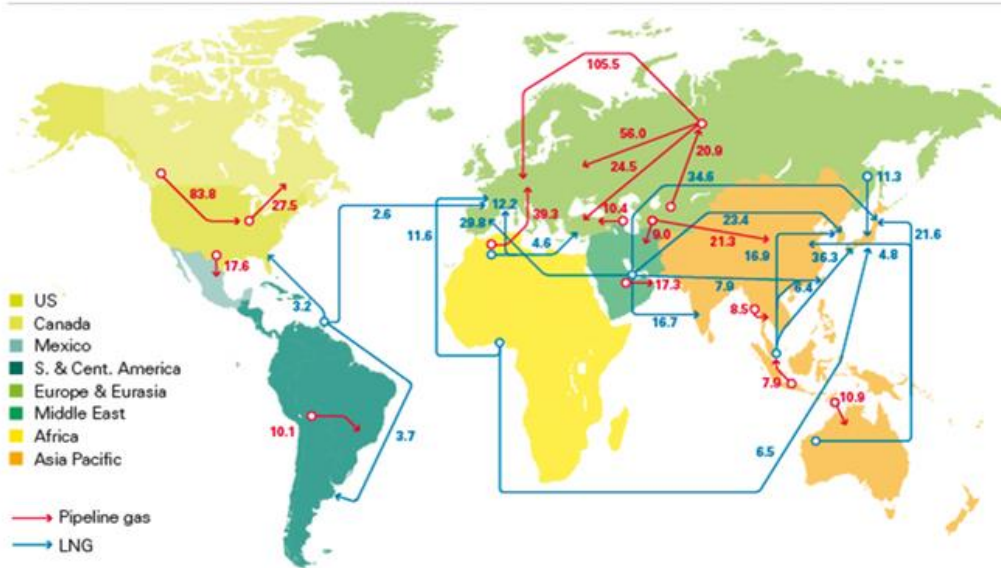
LNG plants can vary in size and efficiency. Different liquefaction cycles are used based on the size of the liquefaction facility. The LNG is transported onboard insulated tank-vehicles or LNG carrier ships. Pipelines are usually more economical over intermediate land distances, while LNG is often the most economical option over greater distances. LNG can be especially cost effective when a long sea pipeline is the alternative. LNG also has an advantage in obtaining NG from smaller fields or associated gas in oil fields, where building a pipeline would not be economically feasible. The alternative today is often to flare the gas or leave it in the ground. With the introduction of floating liquefied natural gas facilities (FLNG), the liquefaction facilities can be moved to new gas fields when the former is depleted.

NG pipelines needs land space and does in some instances cross through whole countries to reach their market. The impact on land usage for LNG is merely at the liquefaction and receiving facility and the end user network. If FSRUs and FLNGs are used, the impact on land use is even smaller.

When a country decides to buy NG, constructing LNG receiving terminals can be quicker and a less capital intensive option than pipelines. Less political work is needed, as bilateral agreements for pipeline construction is circumvented. Faster still is the implementation of FSRUs or FLNG. With LNG, the buyer is not constrained to only a few neighboring NG-pipeline providers. Safety aspects are now constrained to the LNG carriers, receiving terminals and liquefaction units.

Figure 1-1 shows the major Natural gas trade movements in pipelines and by LNG carriers for 2012. It is evident that most NG is sold and transported through pipeline connections for shorter distances while LNG is the only option for long trans-oceanic NG trade.

**Natural gas major trade movements 2012**  
Trade flows worldwide (billion cubic metres)



Market Realist<sup>®</sup>

Source: Cedigaz, CISStat, GIGNL, IHS CERA, Poten, Waterbourne, BP Statistics

*Figure 1-1 Natural gas major trade movements 2012 (Chen, 2014)*

### 1.2 LNG status 2014

In 2014 the total LNG deliveries amounted to 243 million tonnes, accounting for 33% of gas internationally traded and around 10% of total gas consumption. Figure 1-2 shows that 2014 saw a growing import demand for LNG in Asia and Latin America and a lower demand in US and Europe.

One new market for LNG was opened when Lithuania started operating the new import terminal vessel “Independence FSRU”. Becoming the 28, country to import LNG. Worldwide a total of 6 new import terminals came online. Apart from the one in Lithuania, the rest were built in Asia, two of them in China. After 2014 China had 13 import terminals and 3 more under construction. Japan, which had fully phased out nuclear by 2014, experienced an import increase and is still the biggest importer with 89 Mtpa and Korea is the second with 38 Mtpa, China followed with 20 Mtpa and then India with 15 Mtpa. Asia represented 75 % of all imports. (BG-group, 2014)

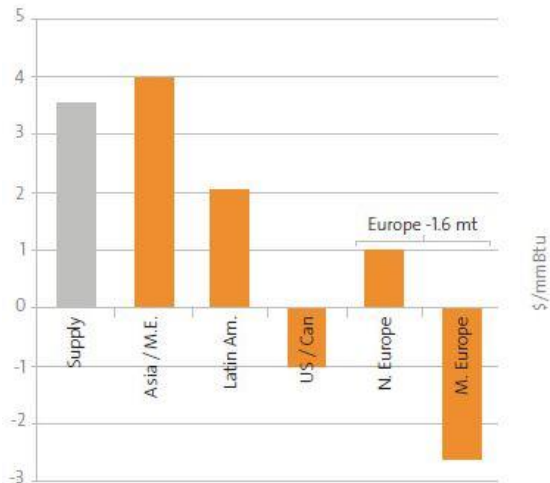


*Figure 1-2 Trade Balance in global markets of LNG in megatonnes between 2013 and 2014. (BG-group, 2014)*

On the supply side the 2014 levels were similar to 2011. Papua New Guinea became the 19<sup>th</sup> nation to start exports of LNG. At full capacity its LNG plant produces 6.9 Mtpa.

### 1.3 LNG Prospects 2014-2016

The price of natural gas /Million Btu varies greatly between geographical areas in today's markets. Japan has historically paid the most premium price while USA has had a much lower cost for gas due to a lot of domestic shale gas production. This is an example of a drive force for potential increase of LNG exports from America to Asia-Pacific. However, as the infrastructure of LNG terminals for export and import is improved and completed globally, it

is expected that the price gap in the different regional gas markets will shrink, as shown in Figure 1-3.



Figure 1-3- Price development and predictions of major LNG regional markets. (BG-group, 2014)

In addition, the Asian LNG and Gas prices are linked to the crude oil price, and prices have seen a substantial drop after the fall of the crude prices during 2014. The crude prices dropped from a record high in 1. Quarter 2014 and ending in a record 3 year low by 3. Quarter. (BG-group, 2014)

LNG suppliers face more challenges in mature LNG markets as Japan begins to re-open their nuclear power plants, weakening the demand for gas. The first of Japans 43 nuclear power plants restarted in August 2015. (Thomlinson, 2015). Korea, a traditionally large buyer of LNG is increasing its use of nuclear power and coal power.

South East Asian markets, Indonesia and Philippines are developing and it is expected that demand for energy, LNG included is rising. China is thought to have the largest potential for creating the new demand in LNG, followed by India.

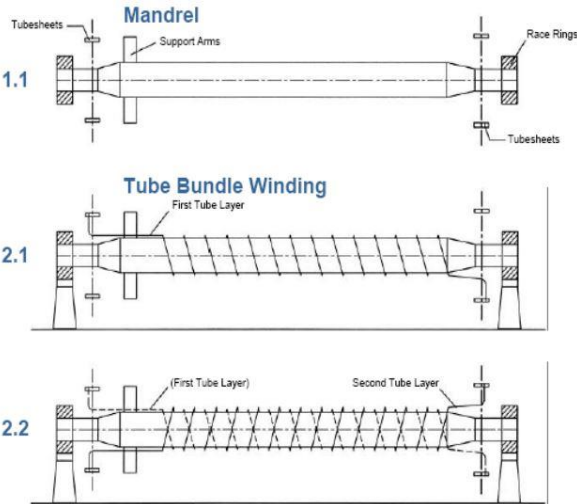
Sub-Saharan Africa’s demand for NG is constrained by a lack of gas infrastructure and low incomes. Therefore export of the gas as LNG can be a more viable solution with less infrastructure investment needs. This gas could contribute to meet the demand for gas in the Asia-Pacific region. By the shores of northern Africa however, markets such as Egypt and Jordan are in the market to buy LNG.

In order to reduce emissions of CO2, NOx, particulates, sulfur and improve general air quality, natural gas power plants is expected to take over for coal plants, especially in China. As a

response to increasing penalties for SO<sub>x</sub> and NO<sub>x</sub> emissions, the shipping industry is also increasingly more interested in using LNG for ship fuel, rather than investing in end of pipe gas treatment solutions or paying the penalties.

**1.4 Spiral wound heat exchanger (SWHE)**

SWHE can handle a very large thermal duty in one single unit. It is the preferred heat exchanger in most large scale LNG production plants and FLNG ships. It is specialized for use in cryogenic processes and can have different modes of operation. The most common operation is to use a vaporizing mixed refrigerant feed from the top shell-side which evaporates over the spiral wound tubes transporting the hot stream/streams. It is also possible to have the refrigerant in gas phase all along. An additional advantage of the SWHE is the ability to cover a wide temperature span. The SWHE consists of several thin tubes spun around a central mandrel tube. As seen in Figure 1-4, small tubes are spun at an angle and in several layers around the mandrel. The bundles of the tubes are contained within a shell to contain the pressure and refrigerant. The single cold stream is introduced from the top shell side, and the possibly multiple hot streams from the bottom tube side. The refrigerant needs particular attention to distribute evenly on the tubes to avoid dry areas. Therefore the two-phase refrigerant is introduced from nozzles as a spray on the top. The two-phase refrigerant enters the top with a low vapor fraction and is driven by gravity at first.



As vaporization ensues from the heat load, the vapor quality of the refrigerant rises, and the flow is increasingly shear driven, with higher vapor content and velocity. At the end of the shell side all of the refrigerant is vaporized.

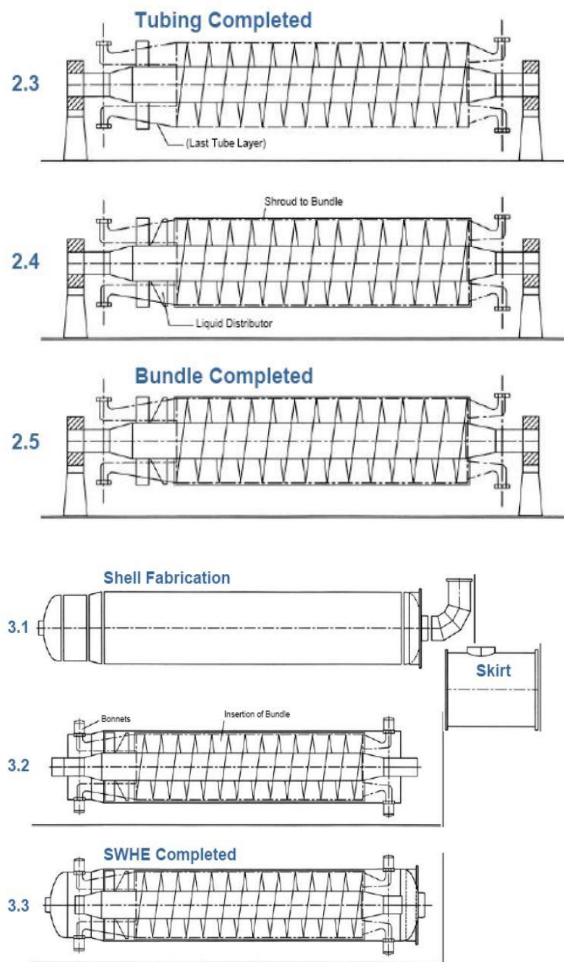


Figure 1-4 Production steps of CWHE

The design of the SWHE is complicated, especially for the mixed refrigerant version. It is complicated due to the two phase flows and large property changes along the heat exchanger and the shift from gravity controlled to shear driven flow. The tube side flow could either be one phase all along for sub cooling of LNG or refrigerant, or vapor phase that condensates upwards in the tubes.

There are a limited number of manufacturers of SWHE worldwide, mainly Air Products International, Linde and Statoil, and the knowledge of the design and operation of SWHE is of some proprietary nature. Meaning that knowledge of best practices is not openly shared between competitors and indeed the public.

The main advantages of the SWHE is its ability to handle a large thermal duty in one single unit and its robustness due to its radial design, as opposed to the plate fin heat exchanger (PFHE).

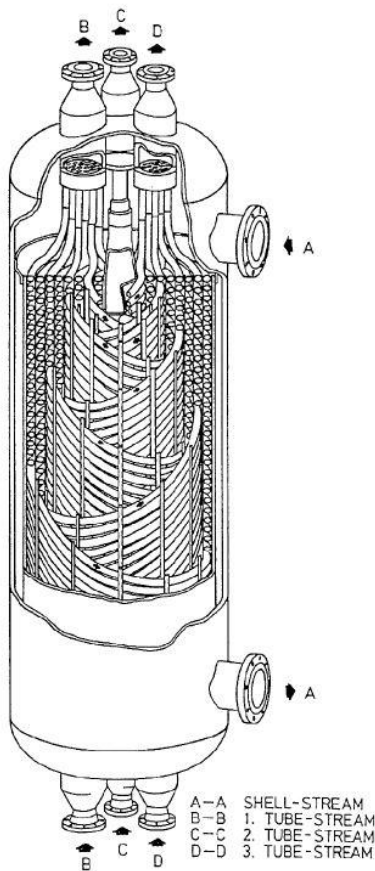


Figure 1-5 Mutistream SWHE

### 1.5 Dimensions of SWHE

Up to...

- 10 000 tubes
- 30000 m<sup>2</sup> heating surface area
- 20 m in height
- 5 m in Diameter

This makes it able to withstand larger thermal stresses, thus being able to expand and contract without damage. Disadvantages include long lead time for production, lack of openness and non-modularity. PFHE can receive added heat exchanging area by adding more plates, while the SWHE is rigid. It is also limited to a single cold stream although it can have several hot streams (Pettersen, 2012). Another complication of the SWHE is the maintenance in case of a leakage in the tubes. It can be very costly if one has to open up, locate and reassemble the HE.

Figure 1-5 depicts a multi-stream SWHE. As shown the cold stream is introduced at the shell side through inlet A to exit A, while the hot streams enter from the bottom tube side at B, C and D.

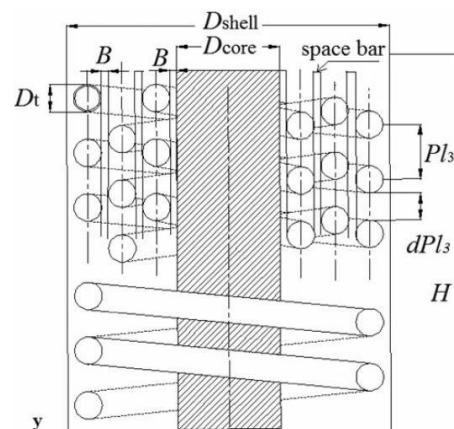


Figure 1-6 Cross section illustrating the innards of an SWHE

Figure 1-6 Shows important geometric parameters, which can influence flow and heat transfer in the SWHE. However simplifications have been made in the following simulations.

## 1.6 LNG liquefaction cycles

LNG is liquefied by compressors introducing work on a refrigerant which then can absorb heat from the warm natural gas (in an evaporator) and reject it to a cooling medium, typically air or water, in a condenser. There are two main strategies for LNG liquefaction, in order to reduce irreversible heat exchange losses. They provide a solution for the refrigerant heating curve to lie close to the natural gas cooling curve with a low temperature difference in the heat exchanger/s. These are the cascade cycle and the mixed refrigerant cycle.

The cascade cycle's efforts to reduce the irreversible heat is done by dividing the refrigeration duty on several cycles with different refrigerants that evaporate at different but constant temperatures. This method is simple technology-wise, and is a well proven technology. It is mostly used in large plants to take advantage of economies of scale.

The mixed refrigerant cycles rely on a refrigerant mixture specifically designed to mimic the cooling curve of the natural gas. This reduces the number of compressors and heat exchangers needed, but needs more knowhow in order to find a suitable refrigerant composition. However these two principles can be combined to make use of their strengths and weaknesses.

### *1.6.1 APCI propane precooled mixed refrigerant process*

Developed by air products international, and the most widely used to date with about 75 % of the market (Mokhatab, 2013) This cycle utilizes the cascade concept in the first steps using propane as refrigerant until about  $-35^{\circ}\text{C}$ , and a second cycle with mixed refrigerant (nitrogen, methane, ethane and propane) for the liquefaction and sub cooling in the main cryogenic heat exchanger, usually a SWHE. At the end of the sub cooling the NG is flashed across Joule-Thomson valves and becomes liquid at atmospheric pressures. Maximum LNG capacity more than 7.8 Mtpa (Mokhatab, 2013)

### *1.6.2 Philips optimized cascade LNG process*

This system uses propane, ethylene and multiple methane cycles. The propane is the coolant for refrigerating the ethylene, methane and feed gas to an intermediate temperature, then the ethylene refrigerates feed gas and the methane cycle, and finally the methane cycle sub cools the feed gas to the appropriate temperature before J-T flash. Capacity of these types of plants are less than 5 Mtpa (Mokhatab, 2013)

### *1.6.3 PRICO process*

Black and Veatch Pritchard's process using a single mixed refrigerant for simplicity and low equipment count. Typically used for peak shaving or smaller scale plants due to its simplicity but lower energy efficiency. It consists of a cold box with low pressure refrigerant as cold stream, and higher pressure refrigerant and feed gas as the hot streams. After the refrigerant has absorbed heat in the cold box it is run through the compressor, then rejects heat in a condenser before it is again introduced to the cold box as a hot stream. After it is cooled down, it goes through the J-T valve and becomes the cold stream. The cold box functions as a recuperator regaining most of the cold from the exiting refrigerant cold stream, this makes the process able to transport heat between distant temperatures more effectively.

### *1.6.4 Statoil/Linde mixed fluid cascade process*

This technology was pioneered in the Snøhvit LNG plant at Melkøya in Hammerfest Northern Norway. This process is a blend of the cascade process and the mixed refrigerant process resulting in a Mixed Fluid Cascade technology. The single refrigerants in the cascade process is replaced with multicomponent refrigerants and will thereby improve the thermodynamic efficiency and possibly the flexibility of the plant. The precooling is done by PFHE while the liquefaction and subcooling utilize SWHEs. The only MFC plant to date, the Melkøya plant in Hammerfest, Norway, has a capacity of 4.3 MTPA (Mokhatab, 2013).

## **2. Literature Review: State of the Art**

Here, a review of falling film flow over horizontal tubes will be presented. Other researchers have made extensive, and somewhat overlapping, reviews in the area of falling film flow over horizontal tubes. However, the area of two phase flow with vapour-liquid shear is still not extensively researched. Great accuracy of model predictions and experimental observations is generally not the case and few flow mode transition maps have been made and none that includes all factors of falling film flow. An inherent problem arises as the value of the observations are subjective since human judgement is needed to determine what flow modes are occurring.

In the research area of flow patterns in SWHE, little literature is publically available due to few manufacturers of SWHEs (Linde and Air Products International) and the proprietary nature of the design process.

## 2.1 Flowrate, Film flowrate and Reynolds number

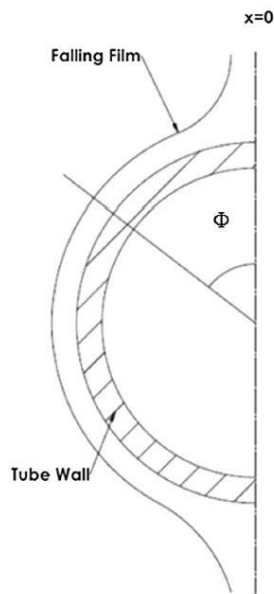


Figure 2-1 – Simplified model of falling film flow (Fernández-Seara and Pardiñas, 2014) (half tube)

The total flowrate is described by  $G = \left[ \frac{kg}{s \cdot m^2} \right]$ , or also named mass flux. This value includes the vapor and liquid flows. However many falling film studies neglect vapor shear effects and calculate the film Reynolds number based on liquid flowrate and dynamic viscosity. The liquid film flowrate is defined  $\Gamma = \left[ \frac{kg}{s \cdot m} \right]$  in words: mass flow per unit length of tube. Depending on their definition of the film flow rate, researchers have confusingly differed in the definition of the Reynolds number. The flowrate  $\Gamma$  can be defined as liquid flowrate over *one side (half)* of the tube or over *both sides* of the tube. This gives Reynolds numbers defined as

$$Re_L = \frac{4\Gamma}{\mu} \quad \text{Equation 2-1}$$

and

$$Re_L = \frac{2\Gamma}{\mu} \quad \text{Equation 2-2}$$

depending on which definition is used (Mitrovic, 2005).

Most Reynolds numbers studied on flow over horizontal open tubes tend to be in the low range as it is necessary to have a low Reynolds number to observe droplet and jet flow modes. This means either a low liquid flowrate or a high liquid viscosity.

## 2.2 Falling film flow over open horizontal tubes

When a liquid, under the influence of gravity, flows from a horizontal tube and down to the next below, the flow may take different forms. Falling film flow is dominated by gravitational, viscous and surface tension effects. (Mitrovic, 1986) did experiments on falling film flow over horizontal tubes. Flow rates, tube spacing and significance of flow patterns on heat transfer was studied. It was found that for low flow rates, the liquid formed droplets and as the flow rate was

increased, a transition between droplets and column flow was established. When the flowrate was further increased, the flow congregated into columns, jets or pillars between the two tubes. The final state was the sheet flow where all the columns were so close together that they merge into a continuous sheet. These main flow modes are depicted in Figure 2-2. (Hu and Jacobi, 1996) confirmed the three main flow patterns and elaborated extensively on the transitional modes and their influence on heat transfer. However because these experiments was done in open systems the influence of vapor flow was not taken into account.

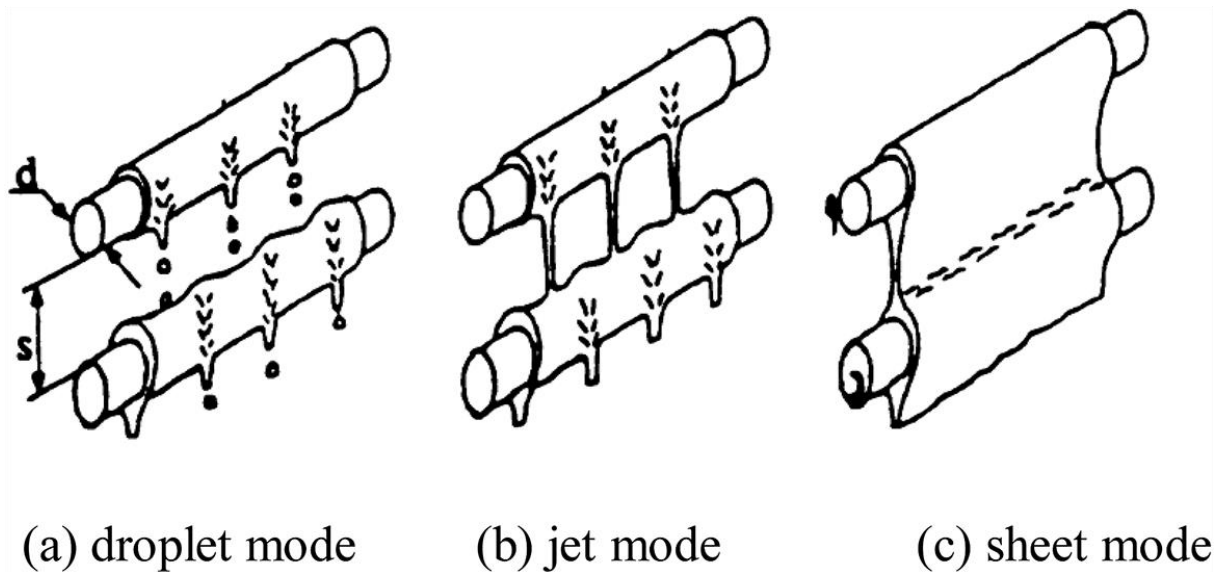


*Figure 2-2 Mitrovic, J. Influence of tube spacing and flow rate on heat transfer from a horizontal tube to a falling liquid film. (Mitrovic, 1986)*

(Armbruster and Mitrovic, 1994) Studied water and isopropyl alcohol and found a general relation that mode transitions could be expressed in the form  $Re = AGa^{0.25}$ . where A was determined empirically.

(Hu and Jacobi, 1996) Reviewed and extended upon previous terminology by (Mitrovic, 1986) in describing falling film flow phenomena. Their focus was on refrigeration purposes. In addition to droplet, jet and sheet flow, transitional flow patterns were also labelled and defined by Hu and Jacobi. In between droplet and jet mode, both droplet flow and jet flow could occur simultaneously, giving rise to the definition of droplet-jet flow and jet-sheet flow. In addition Hu and Jacobi found a hysteresis effect when decreasing flowrate and when the flowrate was increased. Using a dimensional analysis with the Buckingham Pi theorem the dimensionless numbers and factors governing the flow mode transitions were identified as being the liquid Reynolds number  $Re_L = \frac{2\Gamma}{\mu}$ , a modified version of Galileo number:  $Ga^* =$

$\frac{\rho\sigma^3}{\mu^4g}$ , Ohnesorge number:  $Oh = \frac{\rho\sigma d}{\mu^2}$  and Dimensionless tube spacing:  $\frac{s}{d}$  where s is the shortest distance between one tube surface and the next.

In the low Re range, the  $Ga^*$  was found most influential for flow mode transitions, and a linear relation between  $Ga^{*0.25}$  and flow mode transition was shown, Figure 2-3.

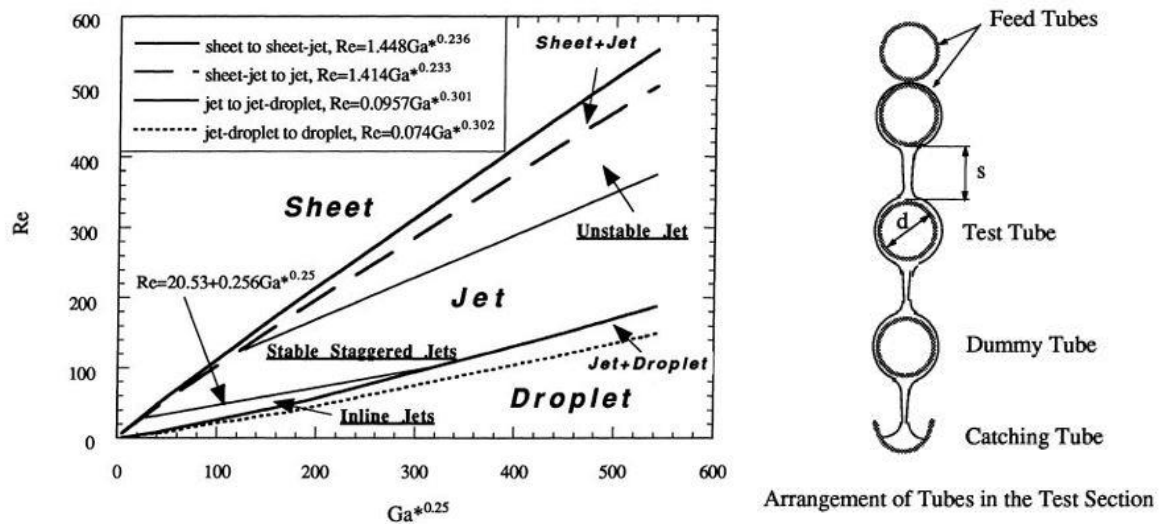


Figure 2-3 - Flow mode transitions when neglecting hysteresis (Hu and Jacobi, 1996)

“A vapor flow can affect the evaporator performance in the following ways: it can change the flow mode and promote the deflection of the liquid flow, droplet atomization and droplet drag; it can affect the film velocity profile and promote waves on the film surface” (Ribatski and Jacobi, 2005)

(Fernández-Seara and Pardiñas, 2014) made a review on falling film evaporators for its use in refrigeration heat exchangers as alternative to pool boiling evaporators. Focus was put on earlier research on horizontal tube falling film flow.

### 2.3 Capillary influence and surface tension

The capillary length is an important parameter for determining the transition from droplet flow to jet flow as it determines droplet size. And may play an important role in the simulations as the tube diameters are quite small. The capillary length is defined as:

$$\lambda_c = \sqrt{\frac{\sigma}{\rho_l g}}$$

Equation 2-3

The effect of surface tension on the shape of a liquid/vapor interface is likely to dominate the effect of gravity when the interface's radius of curvature is much less than the capillary length, and *vice versa*. Therefore a drop of liquid may not fully form and drop to an underlying surface if the space in between is shorter than the capillary length.

## 2.4 Falling flow over Horizontal tube bundles

Higher flowrates and shorter tube spacing is usually the case in experiments on flow over tube bundles compared to experiments on free standing horizontal tubes. Less work has been done on these types of experiments and the challenge arises of visually confirming flow patterns and the possibility of locally different flow patterns along the walls and in the middle of the bundle are hard to predict. Models for predicting flow modes independent of fluid type are also limited.

### 2.4.1 Flow Pattern estimations

(Grant and Chisholm, 1979) used a segmentally baffled and transparent model of a heat-exchanger with a rectangular cross section in an equilateral triangular shape with a P/D (Pitch to diameter) ratio of 1.25. Fluids used were air and water, and the flow regimes were determined visually. They identified bubbly, intermittent and dispersed (spray) flow regimes and proposed a flow map based on dimensionless superficial gas and liquid velocity.

(KONDO and NAKAJIMA, 1980) who experimented with air-water cross-flow in a staggered tube bundle identified and named the flow modes into bubbly, slug, froth and spray flows. However their experiments were limited to very low liquid flow rates ( $G < 5\text{kg/m}^2\text{s}$ ).

(Noghrehkar et al., 1999) Investigated the flow patterns for Air-Water in different geometrical arrangements of tube bundles (staggered or in line) with P/D of 1.47 and 12.7 mm tubes. A resistivity void probe was used to measure the local void fraction. However, only upward flow was considered whereas in a SWHE downward flow is the case. Their findings was made into a flow map as seen in Figure 2-4 based on vapor and liquid velocities.

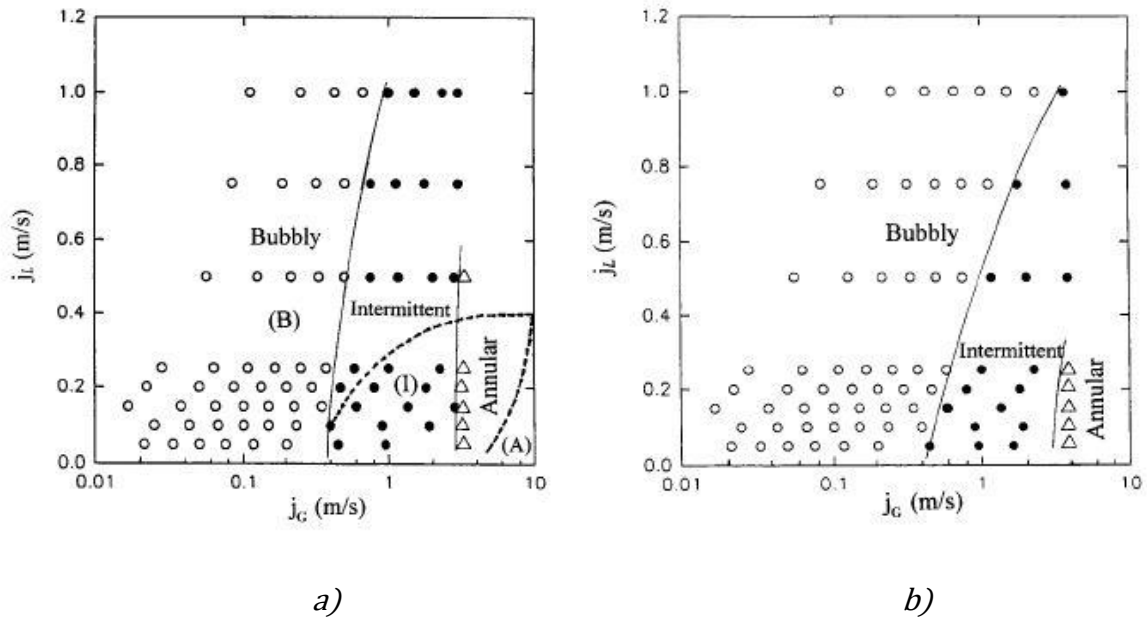


Figure 2-4 – Flow regime map developed by (Noghrehkar et al., 1999) for a) In-line tube arrangement and b) staggered. Vertical upward flow across tube bundles with an Air-Water two phase flow.

For the SWHE accurate flow pattern maps are scarce. However (Xu et al., 1998) did experiments at different superficial gas and liquid velocities in down flow across horizontal tube bundle with air-water mixtures. Their ratio of tube center vertical spacing (Pitch to diameter) was 1.25. They discovered four distinct flow patterns; falling film flow (FF), intermittent flow (IN), annular flow and bubbly flow.

- a) Falling film flow was observed at low mass flows when the superficial velocities of gas and liquid were low. The liquid formed a continuous film around the tube walls with the gas flowing between the tubes. Almost no droplets were entrained in the gas phase and no gas bubbles in the liquid. The surface of the film was wavy, Figure 2-5 a).
- b) Intermittent flow. At higher gas velocities they observed the intermittent flow. The gas-liquid interface was disturbed by waves travelling in the flow direction, the continuous liquid film was intermittently cut off between the tubes by the gas. When the velocity of liquid was increasing, the gas phase was entrained as bubbles in the liquid, Figure 2-5 b).

- c) Annular flow. They discovered that the tube wall and the inside wall of the shell were covered by an annular liquid film and that at a high gas velocity, some liquid was entrained as droplet in the gas, Figure 2-5 c).
- d) Bubbly flow. It was discovered that this flow pattern was similar to the falling film flow, but the liquid film became thicker and contained small dispersed air bubbles. In addition the film was moving faster, Figure 2-5 d). (Xu et al., 1998)

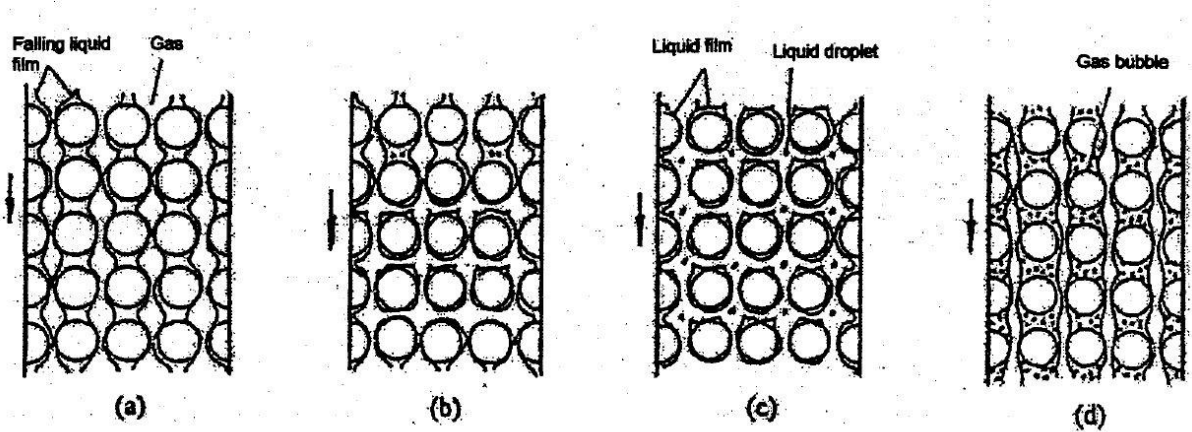


Figure 2-5 -- Flow patterns in vertical down-flow across a horizontal tube bundle: (a) falling film flow; (b) intermittent flow; (c) annular flow; (d) bubbly flow (Xu et al., 1998)

#### 2.4.1 Void fractions

Void fraction is defined as the part of a control volume that is occupied by the gas phase divided by the total control volume. The void fraction is an important parameter for determining and estimating in advance the average fluid density and superficial velocities at a particular location in the bundle. The void fraction is also needed to calculate hydrostatic and acceleration pressure drop of the flow and is the most important parameter since frictional pressure drop is small compared to the static head of the two-phase liquid (John R. Thome, 2010). The homogeneous model for determining void fraction is the simplest one, which all researchers have compared their own models with. However it grossly over predicts the value of the void fractions for the given vapor qualities as is shown in Figure 2-6.

$$\epsilon = \frac{x/\rho_v}{\left(\frac{1-x}{\rho_l}\right) + \left(\frac{x}{\rho_v}\right)} \quad \text{Homogeneous void fraction model} \quad \text{Equation 2-4}$$

Different researchers developed new models closer to reality. Some results still conflict with each other, however their discrepancies in results can also be attributed to different measurement techniques by different researchers. Take (Schrage et al., 1988) and (Noghrehkar et al., 1999) as an example, where Schrage measures the volumetric void fraction by quick closing plates and then checking liquid level, Noghrehkar uses a continuous local measurement method with sensors.

It is important to keep in mind that the void fraction is different at local measurements either being cross sectional (2D) or at different control volumes (3D) depending on the geometry of the tube bundle. This effect is also not taken into account in the homogeneous model.

(KONDO and NAKAJIMA, 1980) found that the void fraction in cross flow tube bundles increases with increased superficial gas velocity, while the superficial liquid velocity has negligible effect on void fraction. Their study did only test very low mass fluxes ( $G \leq 5 \text{ kg/m}^2\text{s}$ )

(Schrage et al., 1988) found that for a fixed vapor quality  $X$  the volumetric void fraction was found to increase by increasing mass flux. The same result was found by (Xu et al., 1998). However, the significance of the effect varied by the fixed vapor qualities.

The range of mass flows and qualities they tested were:

Schrage:

Xu:

$$0,0003 \leq x \leq 0,68$$

$$0,001 \leq x \leq 0,68$$

$$54 \leq G \leq 683$$

$$54 \leq G \leq 683$$

$$1 - 3 \text{ atm}$$

$$1 - 2 \text{ atm}$$

Schrage et al. (1988) proposed an empirical method for predicting the volumetric void fraction by applying a multiplier to the homogeneous void fraction. A non-dimensional version was made by using R-113 refrigerant data (John R. Thome, 2010):

$$\frac{\varepsilon_{vol}}{\varepsilon_{hom}} = 1 + 0.123 \left( \frac{\ln x}{F_r^{0,191}} \right) \quad \text{Equation 2-5}$$

using Froude number defined by the outer tube diameter:

$$F_r = \frac{G}{\rho_l \sqrt{gD}} \quad \text{Equation 2-6}$$

(Xu et al., 1998) made a prediction model for void fraction based on determining the Martinelli parameter  $X_{tt}$ . However their expressions needs many empirical constants to fit in order to work for different fluids and may thus vary between different fluid types and conditions.

(Feenstra et al., 2000) Did experiments and concentrated on determining the void fraction in flow over horizontal tube bundles by making an empirical expression for the parameter  $S = u_v/u_l$ . Then use S in the eventual expression for void fraction that obeys the boundary conditions at  $x=0$  and  $x=1$ . They argue that S is the most problematic to estimate and also most important for the void fraction. In addition the model should fit any fluid or tube geometry. However the model does not take into account tube geometric arrangement like in-line or staggered arrangement of the tube bundles.

Equations developed for void fraction determination for two phase flows across tube bundles by Feenstra et al., (2000):

$$\text{Void fraction } \varepsilon = \left( 1 + S \frac{\rho_v}{\rho_l} \left( \frac{1}{x} - 1 \right) \right)^{-1} \quad \text{Equation 2-7}$$

And S is calculated by

$$S = 1 + 25.7 (Ri \text{ Cap})^{0.5} \left( \frac{P}{D} \right)^{-1} \quad \text{Equation 2-8}$$

$$Ri = \frac{(\rho_l - \rho_v)^2 g (P - D)}{G^2} \quad \text{Equation 2-9}$$

The Richardson number represents the ratio between the buoyancy force and the inertia force. And the Capillary number (Cap) represents the ratio between the surface tension and the viscous force and is defined as:

$$\text{Cap} = \frac{\mu_l u_v}{\sigma} \quad \text{Equation 2-10}$$

The mean vapour phase velocity  $u_v$  is determined based on the resulting void fraction

$$u_v = \frac{xG}{\varepsilon \rho_v} \quad \text{Equation 2-11}$$

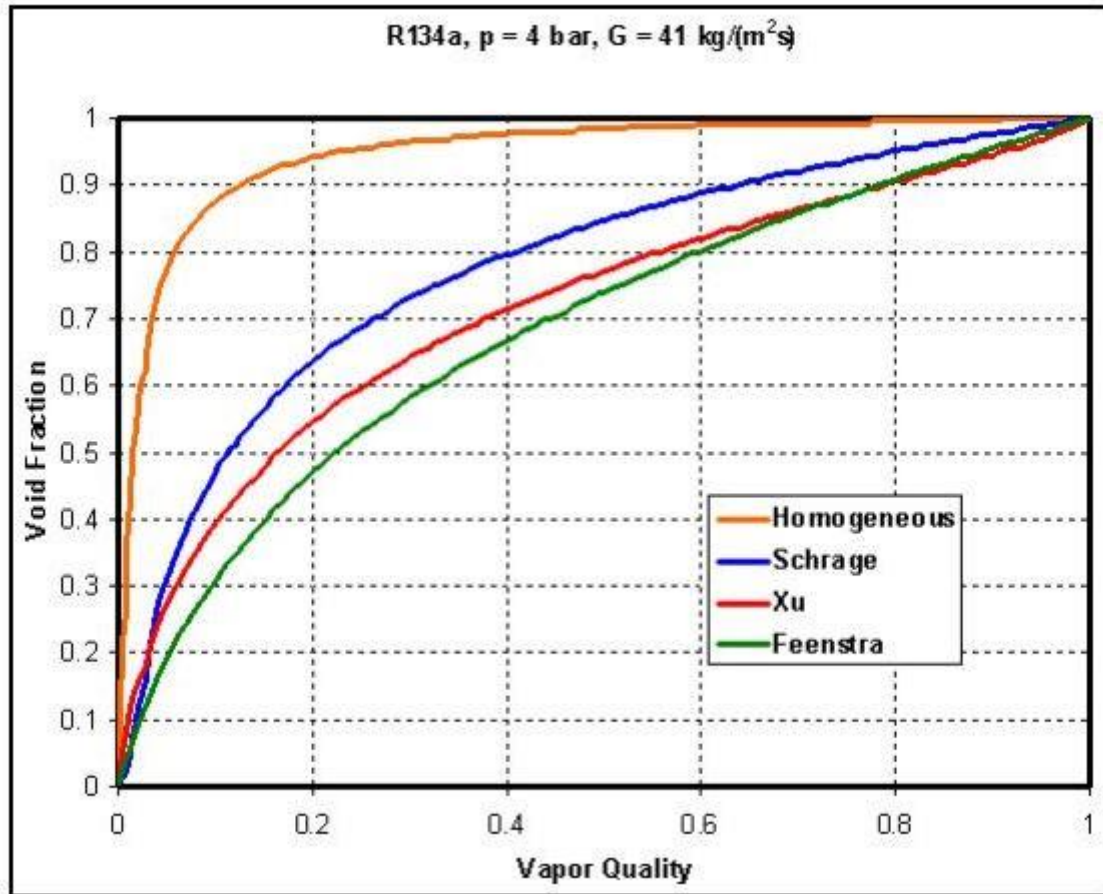


Figure 2-6 Comparison of different void fraction prediction models in horizontal flow shell side tube bundle flow, by (John R. Thome, 2010)

The homogeneous model always provides a higher result for the void fraction than real results do, one reason for this is the inherent assumption of a Slip factor of  $S = 1$ . However, in reality this assumption is never valid and the Homogeneous model serves as an upper limit for the void fraction that a given model should not exceed. Also note that when  $S > 1$  then the Volumetric void fraction should be larger than the cross sectional void fraction.

The Feenstra-Weaver-Judd model will be tested in the CFD simulations due to the fact that the model does not need any fitting of coefficients to any specific fluid, but rather it seeks to fit all fluids and also incorporates and takes into account for different P/D ratio in its application. It is also thought to be the most accurate and reliable available method for predicting void fractions in vertical two-phase flows on tube bundles as it has been successfully compared to air-water, R-11, R-113 and water steam void fraction data obtained from different sources, including the data obtained from Schrage, Hsu and Jensen (1988). It was developed from triangular and square tube arrangement data and with P/D ratios from 1.3 to 1.75 and tube diameters ranging between 6.35 to 19.05 mm. Importantly for this study this

method is found to be best for predicting static pressure drops at low mass flow rates for an 8 row tube bundle under evaporating conditions by Causolini Robinson and Thome (2006)

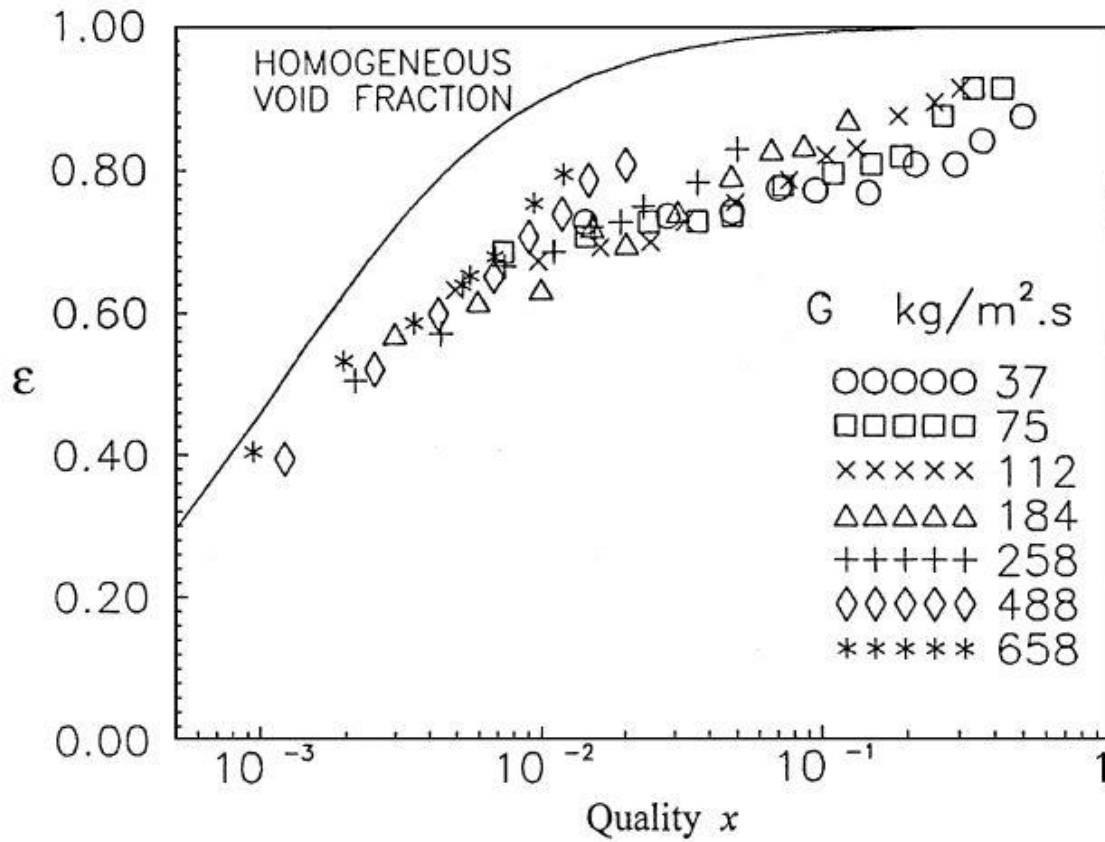


Figure 2-7 Experimental results from (Xu et al., 1998) downward flow with Air-Water. In line square arrangement with a pitch to diameter ratio of 1.28 Void fraction measured is Volumetric.

(Grant and Chisholm, 1979) used a prediction model for void fraction which Feenstra et al. expanded upon:

$$\text{Void fraction } \epsilon = 1 + S \frac{\rho_v}{\rho_l} \frac{1}{x} - 1 \quad \text{Equation 2-7}$$

However the relation for S in the Chisholm correlation is different and simpler. No pitch, diameter, mass flow surface tension gravity or liquid viscosity is taken to account in the Chisholm model compared to the Feenstra model.

$$S = \left(1 + x \frac{\rho_l - \rho_v}{\rho_v}\right)^{0,5} \quad \text{Equation 2-12}$$

## 2.5 Horizontal tube CFD simulations

(Jafar et al., 2010) Used CFD simulations to study the influence of flowrate, cylinder diameter and heat flux on the Average Nusselt number. Their numerical model came in good agreement with experimental results. They used a model of 3 circular horizontal tubes aligned vertically. In addition they utilized symmetry such that the model is split in half vertically down the middle of the tubes and mirrored over the symmetry axis. They concluded that increasing liquid flowrate (Reynolds number) increased the heat transfer coefficient. Decreasing the tube diameter increased the heat transfer coefficient. For completely wetted surfaces the heat flux had no significant impact on heat transfer coefficient.

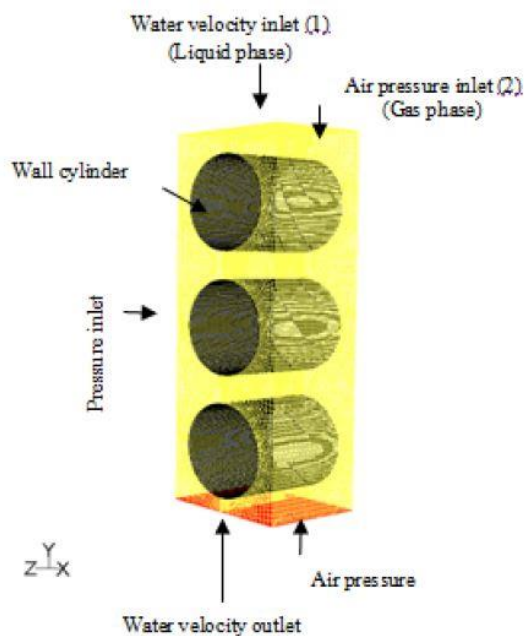


*Figure 2-8- 3 tube horizontal tubes model with downward fluid flow, cut along the middle and mirrored along the vertical axis.*

A large difference in heat transfer coefficient was confirmed between a large diameter tube bundle of 0.1m and smaller diameter tube of 0.022m, where the heat transfer coefficient were approximately doubled for the smaller diameter tubes. Heat flux had little to no effect on average heat transfer coefficient and thus Nusselt number.

A recent study from the university of Harbin by (Wu et al., 2014) simulated evaporation and flow of propane at 4 bar through a test section meant to resemble a section of a SWHE. The purpose of the study was to predict mass transfer time relaxation parameter for boiling simulation on the shell side of an LNG SWHE. The mesh was constructed by tetra/mixed

cells. To verify the required mesh density and show the grid independency three tests were performed. Eight tubes and half tubes in the side walls were used in the model depicted in Figure 2-9. The top 4 tubes and half tubes were adiabatic and for stabilizing the flow. The mass flow inlet is pure liquid refrigerant methane, ethane or propane. The geometry of the model is based on the same geometry tested by (Aunan, 2000).

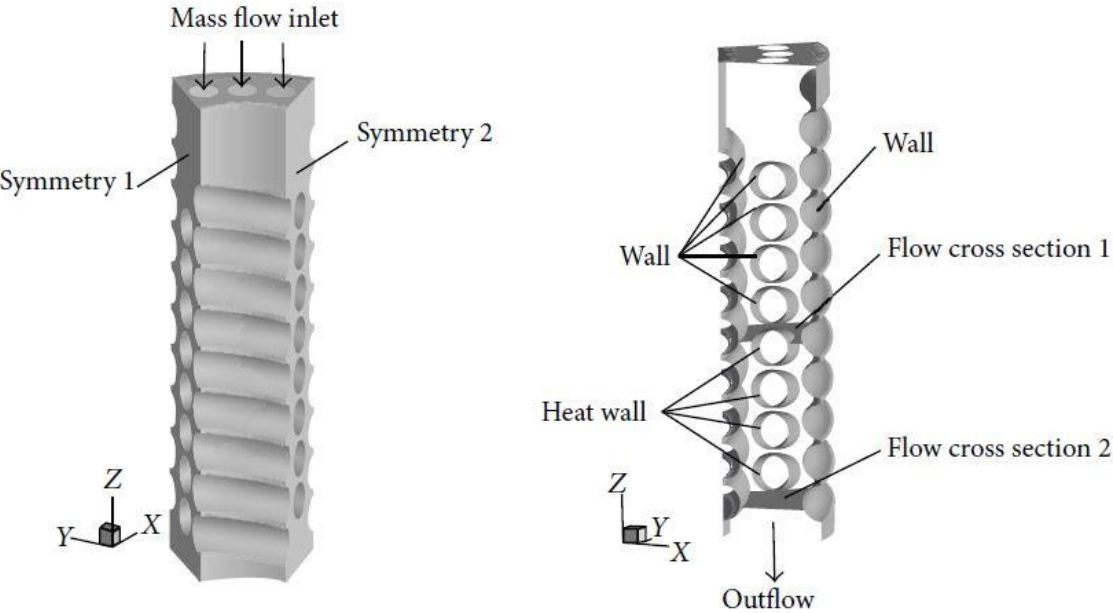


Figure 2-9 – Wu et al. model of SWHE

**2.6 Falling flow in SWHE**

The down flow in the shell side of the SWHE can relate to the flow patterns found by Xu, Tso et al. (1998). (Aunan, 2000) describes how the shell side flow through the SWHE goes through different stages based on the vapor fraction.

- At first one might assume gravity drained falling film type flow. The liquid flows in a continuous sheet between the tubes. As seen in Figure 2-2 c) and Figure 2-5 a)
- As more liquid starts to evaporate the liquid will no longer be in contact with itself from tube to tube. This is the intermittent stage between film flow and two phase shear flow. Figure 2-5 b)
- In the two phase shear flow section the liquid film around the tubes is even thinner and the gas phase is the dominant force, overcoming gravity. Annular flow as depicted in Figure 2-5 c)

- Superheated vapor flow. Finally, all liquid is evaporated before reaching the outlet, only superheated vapor remains in single phase flow.

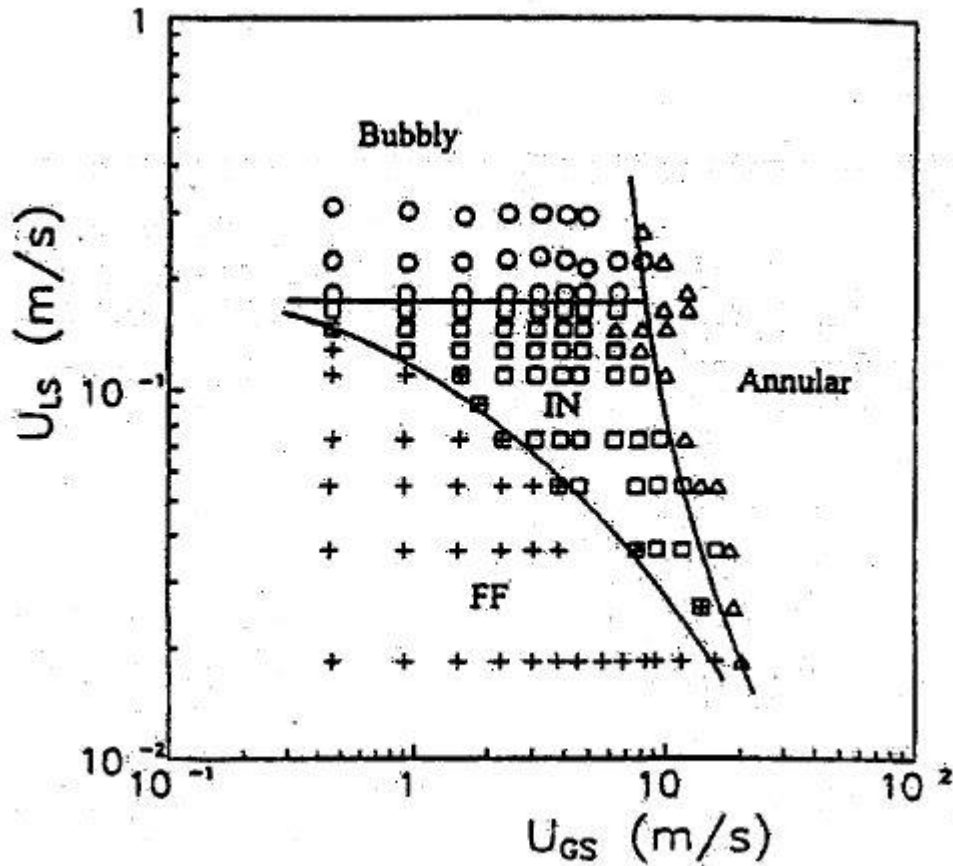


Figure 2-10 – Flow map of falling film flow: (FF) film flow; (IN) intermittent (Xu et al., 1998)

Superficial velocity is defined as

$$U = \frac{Q}{A} = \frac{\text{Volume flowrate of one phase}}{\text{Total cross sectional area}} \left[ \frac{m}{s} \right]$$

### 2.7 Flow patterns influence on heat transfer

Thin falling film evaporators have advantageously high heat transfer even at low liquid flowrates, low evaporation temperature and temperature differences, and because the flow patterns influence heat transfer capabilities in the heat exchangers, it is important to take this

into consideration. The thickness of the fluid film and the flow distribution of the fluid is of great importance for the heat transfer coefficient. The goal is to have the fluid covering the tubes and the gas flowing in between, as the liquid phase has a higher convective heat transfer coefficient.

Important factors that influences shell side flow patterns are

- Phase properties of the liquid and gas and surface tension
- Vapor fraction
- Mass flow rate
- Evaporation and condensation (phase change)
- Shell-side geometry; inclination, spacing and diameters of tubes and so on.
- Finned or modified tubes

The possible different flow regimes in the shell side of the heat exchanger include the superheated vapor flow, where the sensible heat of the fluid gives the temperature difference, and no liquid fraction is present. More interestingly for this thesis is two phase flows, where both vapor and liquid components are present. The falling film flow and shear flow with low vapor shear have the characteristic that the liquid and the vapor flow separately and segregated in their own domains. The liquid flows over the tubes and the vapor in the space between the tubes. When the vapor shear is high the effect of gravity becomes more negligible and the flows become intertwined and flow together (Aunan, 2000). The three different flow regimes have different heat transfer capabilities and pressure drop performances.

### 2.7.1 Factors influencing the heat transfer coefficient

Parameter	Influence on $h$ as Parameter Increases	Physical Explanation	Studies
<b>Convective Evaporation Regime</b>			
Flow Rate	Increase, decrease, and increase again	Initial increase as dryout decreases, decrease due to thickening laminar film, and increase due to turbulence or boundary layer development	(Brumfield and Theofanous, 1976; Chyu and Bergles, 1987; Conti, 1978; Fujita and Tsutsui, 1998; Lee <i>et al.</i> , 2012; Li <i>et al.</i> , 2011a; Liu and Yi, 2001; Liu <i>et al.</i> , 2002; Lorenz and Yung, 1979; Mitrovic, 1986; Owens, 1978; Parken and Fletcher, 1982; Parken <i>et al.</i> , 1990; Putilin <i>et al.</i> , 1996; Rifert <i>et al.</i> , 1992; Rogers <i>et al.</i> , 1995; Tan <i>et al.</i> , 1990; Zeng <i>et al.</i> , 1995)
Dryout	Decrease	Very low local $h$ in dry areas	(Fujita and Ueda, 1978; Ganić and Getachew, 1986; Gross, 1994; Li <i>et al.</i> , 2011a; Li <i>et al.</i> , 2011b; Li <i>et al.</i> , 2010)
Heat Flux	No effect	No mechanism to influence $h$	(Conti, 1978; Fujita and Tsutsui, 1995b, 1996, 1998; Li <i>et al.</i> , 2011b; Liu and Yi, 2001, 2002; Liu <i>et al.</i> , 2002; Owens, 1978; Parken, 1975; Parken and Fletcher, 1982; Parken <i>et al.</i> , 1990)
Temperature	Increase	Decreased liquid viscosity decreases film thickness	(Kocamustafaogullari and Chen, 1988; Liu, 1975; Owens, 1978; Parken, 1975; Parken and Fletcher, 1982; Parken <i>et al.</i> , 1990)
Distributor Height / Tube Spacing	Increase	Increased local heat transfer coefficient at point of fluid impact, but at high spacings reduces film coverage	(Chyu, 1984; Chyu and Bergles, 1985, 1987; Liu, 1975; Liu and Yi, 2002; Mitrovic, 1986; Parken, 1975)
Angle Around Tube	Decrease	Fluid impingement and thermal boundary layer growth	(Hu and Jacobi, 1996b; Mitrovic, 1986; Putilin <i>et al.</i> , 1996; Rifert <i>et al.</i> , 1989; Rifert <i>et al.</i> , 1992; Rogers and Goindi, 1989; Tan <i>et al.</i> , 1990)
Tube Diameter	Decrease	Tube angle effects apply to larger portion of small diameter tubes	(Liu and Zhu, 2005; Parken, 1975; Parken and Fletcher, 1982; Parken <i>et al.</i> , 1990)
Vapor Flow	Increase, decrease, or no net effect	Increase due to waviness or reduced film thickness; decrease due to thicker film, entrainment or deflection, and dryout	(Garcia <i>et al.</i> , 1992; Liu, 1975; Ribatski and Jacobi, 2005; Yung <i>et al.</i> , 1980)

Parameter	Influence on $h$ as Parameter Increases	Physical Explanation	Studies
Surface Enhancement	Increase	Increased tube surface area, film waviness or tube coverage, decreased film thickness, modified velocity profile and boundary layer development	(Chien and Chen, 2012; Chien and Tsai, 2011; Lee <i>et al.</i> , 2012; Li <i>et al.</i> , 2011b; Liu and Yi, 2001, 2002; Putilin <i>et al.</i> , 1996; Rifert <i>et al.</i> , 1989; Rifert <i>et al.</i> , 1992; Sabin and Poppendiek, 1978)
Tube Bundle	Decrease or no effect	Minimal effect with complete wetting, but substantial decrease if film breakdown occurs	(Fujita and Tsutsui, 1998; Lorenz and Yung, 1982; Zeng <i>et al.</i> , 1997)
<b>Boiling Regime</b>			
Flow Rate	Increase, then no effect or increase	Initial increase as dryout decreases, no effect in areas of tube dominated by boiling, but convective effects persist	(Chien and Chen, 2012; Chien and Tsai, 2011; Chyu and Bergles, 1985, 1987; Habert and Thome, 2010a; He <i>et al.</i> , 2011; Moeykens, 1994; Moeykens and Pate, 1994; Parken, 1975; Parken <i>et al.</i> , 1990; Roques and Thome, 2007a; Yang and Shen, 2008; Zeng <i>et al.</i> , 1995)
Dryout	Decrease	Very low local $h$ in dry areas	(Armbruster and Mitrovic, 1995; Christians and Thome, 2012a; Fujita and Tsutsui, 1998; Habert and Thome, 2010a; Roques and Thome, 2007a, 2007b)
Heat Flux	Increase	Increased nucleation site density and boiling over larger portion of tube	(Chien and Chen, 2012; Chien and Tsai, 2011; Fletcher <i>et al.</i> , 1974; Fletcher <i>et al.</i> , 1975; Habert, 2009; Habert and Thome, 2010a; He <i>et al.</i> , 2011; Liu and Yi, 2001, 2002; Moeykens, 1994; Moeykens and Pate, 1994; Parken, 1975; Parken <i>et al.</i> , 1990; Roques, 2004; Roques and Thome, 2007a; Yang and Shen, 2008; Zeng <i>et al.</i> , 1995)
Temperature	Increase	Decreased film thickness and increased nucleation site density	(Chien and Chen, 2012; Chien and Tsai, 2011; Fletcher <i>et al.</i> , 1974; Fletcher <i>et al.</i> , 1975; Parken, 1975; Zeng <i>et al.</i> , 1995)
Distributor Height / Tube Spacing	No effect	Possible increased local heat transfer coefficients at point of impact, but minor influence relative to boiling	(Chyu, 1984; Chyu and Bergles, 1985, 1987; Danilova <i>et al.</i> , 1976; Roques and Thome, 2007b; Yang and Shen, 2008; Zeng <i>et al.</i> , 1995)

Parameter	Influence on $h$ as Parameter Increases	Physical Explanation	Studies
Angle Around Tube	Decrease then increase	Fluid impingement at top of tube and boiling at bottom	(Parken and Fletcher, 1982; Parken <i>et al.</i> , 1990)
Tube Diameter	Decrease or increase	With high boiling $h$ , increase due to more boiling area, otherwise convective evaporation trend is observed	(Fletcher <i>et al.</i> , 1974; Moeykens, 1994; Moeykens and Pate, 1994; Parken, 1975; Parken <i>et al.</i> , 1990)
Vapor Flow	Increase, decrease, or no net effect	Increase due to waviness or reduced film thickness; decrease due to thicker film, entrainment or deflection, dryout, and suppressed bubble nucleation	(Parken, 1975; Ribatski and Jacobi, 2005)
Surface Enhancement	Increase	Provides bubble nucleation sites and possible convective enhancement	(Bukin <i>et al.</i> , 1982; Chien and Chen, 2012; Chien and Tsai, 2011; Christians and Thome, 2012a; Chyu <i>et al.</i> , 1982; Chyu and Bergles, 1989; Habert and Thome, 2010a; Moeykens <i>et al.</i> , 1995a; Roques and Thome, 2007a; Tan <i>et al.</i> , 1990; Zeng <i>et al.</i> , 1998)
Tube Bundle	Decrease or no effect	Minimal effect with complete wetting, but substantial decrease if film breakdown occurs	(Chang and Chiou, 1999; Christians and Thome, 2012a; Habert and Thome, 2010a; Moeykens and Pate, 1995; Roques and Thome, 2007a)

*Table 2-1. Overview of parameters influencing the heat transfer coefficient, table and content credit to master thesis of (John G. Bustamente, 2014)*

### 3. CFD model setup

#### 3.1 CFD Governing Equations

The CFD software uses the Navier-Stokes equations for each control volume (cell) in order to establish the velocity and pressure field. The N–S equations are used for simulation of velocity and pressure.

##### 3.1.1 Continuity equations

Volume fractions and conservation of mass:

$$\frac{\partial}{\partial t} (\rho_v \alpha_v) + \nabla \cdot (\rho_v \alpha_v \vec{u}) = 0 \quad \text{Vapor}$$

$$\frac{\partial}{\partial t} (\rho_l \alpha_l) + \nabla \cdot (\rho_l \alpha_l \vec{u}) = 0 \quad \text{Liquid}$$

##### 3.1.2 Momentum equation

A single momentum equation is solved throughout the domain, and the resulting velocity field is shared among the phases. The momentum equation, shown below, is dependent on the volume fractions of all phases through the properties  $\rho$  and  $\mu$ .

(20)

$$\frac{\partial}{\partial t} (\rho \vec{u}) + \nabla \cdot (\rho \vec{u} \vec{u}) = -\nabla p + \mu \cdot \nabla^2 \vec{u} + \rho \vec{g} + F_\sigma$$

### 3.1.3 Surface tension

$$F_{\sigma} = \sigma \frac{\rho k_l \nabla \alpha_l}{1/2 (\rho_v + \rho_l)}$$

The surface tension is a force, acting only at the fluid interfaces that is required to maintain equilibrium in such instances. It acts to balance the radially inward inter-molecular attractive force with the radially outward pressure gradient force across the surface interface. In regions where two fluids are separated, but one of them is not in the form of spherical bubbles, the surface tension acts to minimize free energy by decreasing the area of the interface.

### 3.1.4 Material properties

The properties appearing in the transport equations are determined by the presence of the component phases in each control volume. In a two-phase system, for example, if the phases are represented by the subscripts *v* (*vapor*) and *l* (*liquid*), and if the volume fraction of the liquid is being tracked, the density in each cell is given by:

$$\rho = \alpha_l \rho_l + (1 - \alpha_l) \rho_v$$

Other properties, such as viscosity is calculated in the same manner. (20)

### 3.1.5 Energy Equation

$$\frac{\partial}{\partial t} (\rho E) + \nabla \cdot (\vec{u} (\rho E + p)) = \nabla \cdot (k_{eff} \nabla T) + S_h$$

The energy equation governs the heat transfer solutions in fluent. For this study, it is switched off. Flow pattern studies are usually performed under adiabatic conditions.

## 3.2 2D and 3D models

2D and 3D models have advantages and disadvantages when being used in fluent simulations. If the 3D models has the same grid mesh density as the 2D one it will contain an order of magnitude more nodes than the 2D model. This will result in an increased computing time. This means that the grid density can be higher for the 2D model giving more accurate results of an intersection. As for the accuracy, the two dimensional model cannot accurately simulate 3D phenomena such as bubble formation and effects such as columnar/jet flow, radial waves, bubble formation and inclination of tubes. For these the 3D models must be applied.

The 2D model can be used for initial tests and flow pattern estimates. Confirmation of flow modes, accurate calculation of mass transfer, and for heat transfer calculations CFD calculations should be based on simulations with 3D models.

### 3.3 Geometry

The x-y plane geometry of the 2D and 3D film flow simulations have dimensions similar to the heat exchanger from the experimental setup at SJTU and NTNU. Figure 3-1. Shows an illustration of the geometry, made in Autodesk Inventor.

The distance between inlet and the upper tube is kept small to reduce calculation time, using the same reasoning for the outlet section, the distance between the lower tube and the outlet is kept small. However, it was found that the exit region needed to be somewhat longer due to effects of the tail flow of the liquid film could have on the liquid above, and to be able to observe flow patterns close to the exit. The width is determined by the radial distance of the tubes and is defined such that the edges lies in the middle of hypothetical parallel tubes according to the constraint of 16mm distance of the tube centers in the radial direction.

*Table 3-1 model geometries*

Simple 2D and 3D model dimensions	
Tube outer Diameter (D)	12 mm
Tube center vertical spacing (P)	13 mm ( 14 and 16 mm)
P/D ratio	1,083 ( 1.17 and 1.33)
Radial tube center spacing	16 mm
Tube horizontal spacing (B)	4 mm
Tube vertical spacing	1 mm (2 mm and 4 mm)
Model width (x)	16 mm
Model Height (y)	42 mm ( 44 and 54 mm)
3D model depth (z)	10 mm

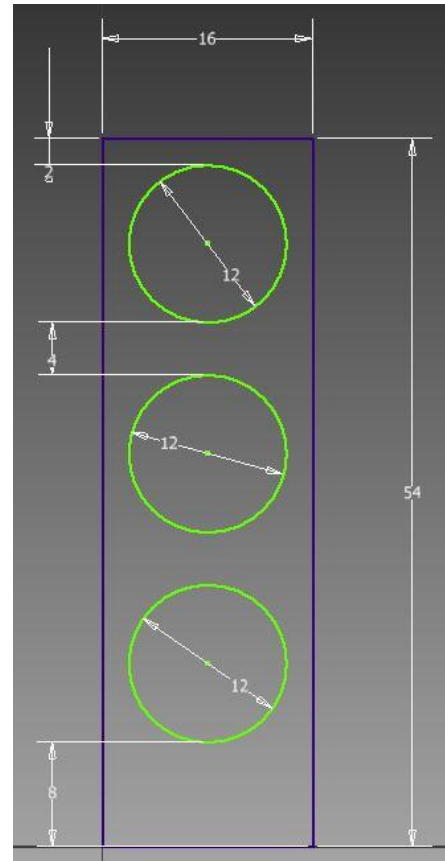
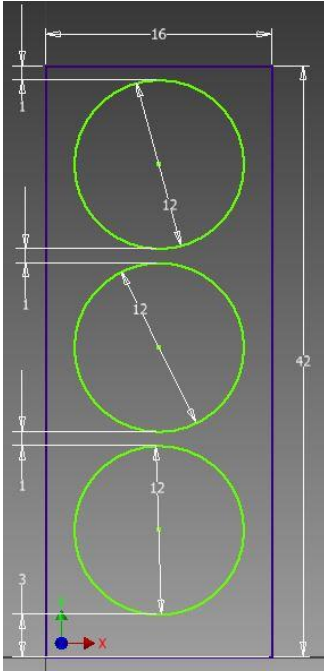


Figure 3-1- Inventor sketches (x-y-plane) of the 1mm and 4 mm vertical tube spacing model geometries. For 3D modelling an extrusion of 10mm depth is used in both cases.

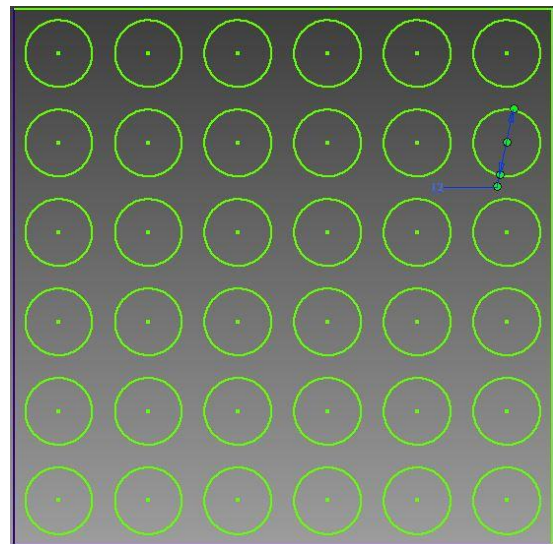
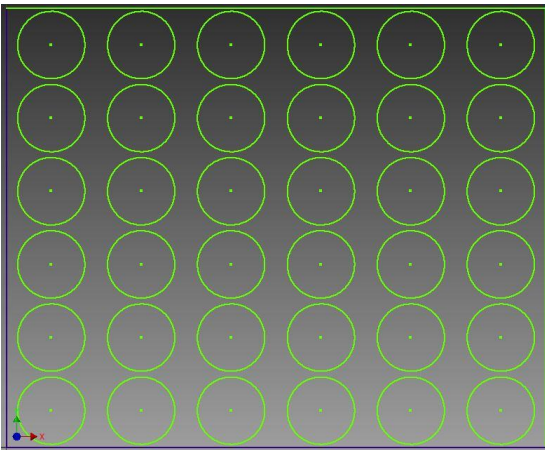


Figure 3-2- Illustration of what the tube bundles look like with all dimensions from Table 3-1 included.

As shown in Figure 3-2 the tube bundles simulated are arranged in an in-line formation, where the next tubes in both the directions are squarely placed directly beside or underneath. This is as opposed to staggered arrangement where no unobstructed line is found for the fluid

flow as the next tubes are shifted such that they are placed under the gap of the previous tubes.

### 3.4 Meshing

In order to make the appropriate hexa-mesh for the VOF multiphase simulations, ANSYS ICEM was used. To make sure that the solution is valid it was necessary to test a case with different mesh densities. The resulting meshes are shown below in Figure 3-3. An analysis of the validity of the different mesh size solutions is found on page 40. These meshes were used in a pre-study and medium mesh was sufficient for low vapor fraction flows.

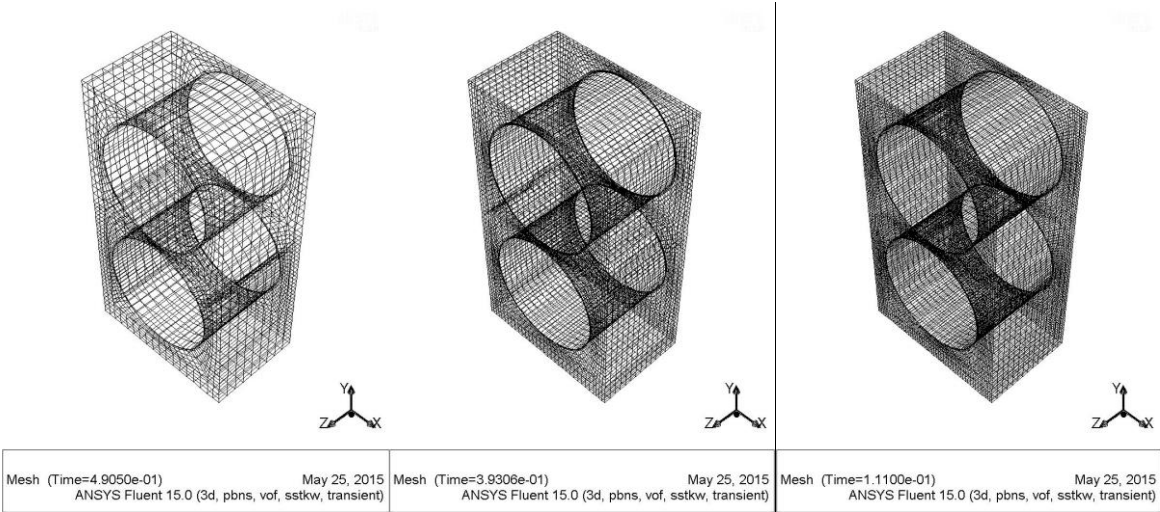
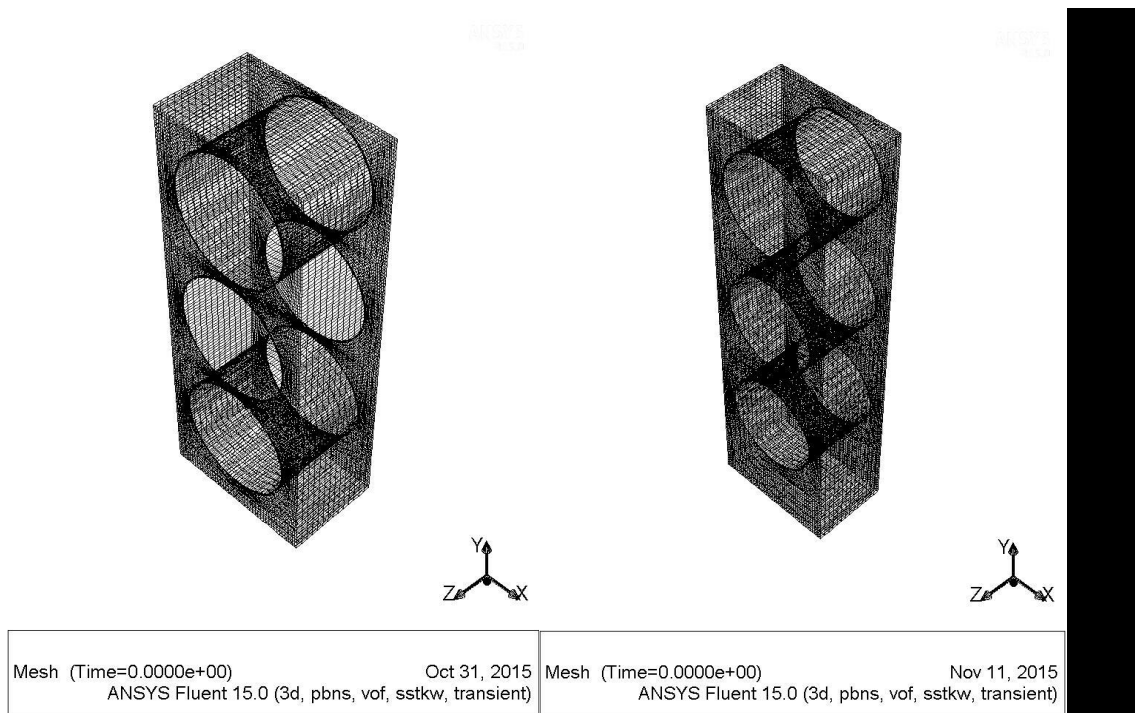


Figure 3-3-

(a) Coarse Mesh 4 Cells/mm<sup>3</sup>      (b) Medium Mesh 17 Cells/m      (c) Fine Mesh 32 Cells/mm<sup>3</sup>

However, most of the simulations in this study is with 3 tube models, and a mesh density of 33 Cells/mm<sup>3</sup> has been used depicted in Figure 3-4.



*Figure 3-4 – Mesh of tube bundle model with 3 tubes. Left: 1mm vertical tube gap ( $P/D=1.08$ ). Right: 4mm vertical tube gap ( $P/D$ ) 1.33.*

The left and right wall is modeled as a Periodic boundary. For a periodic boundary the exact same geometry exists on each side of the simulated area, i.e. if some fluid passes through the left boundary, it will reappear in the right boundary and vice versa, it will still contain the same properties as before. This is another measure to save calculation time and to add realism to the small model. Ideally a longer model in the tube direction ( $z$ ) would yield better results, but it is a very expensive measure with respect to calculation time as each  $x$ - $y$  grid of cells added contains a high number of cells and by each millimeter added in the  $z$  direction, more than one  $x$ - $y$  grid is needed to obtain satisfactory grid density especially for the finer mesh densities.

### 3.5 Fluent solver solution setup

After modelling and meshing, the solver used for calculating the solution is ANSYS fluent.

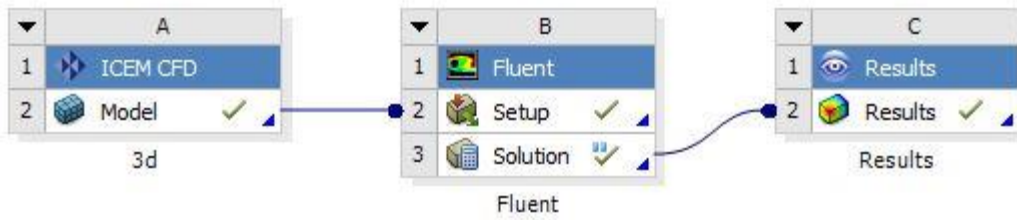


*Figure 3-5 – Overview of the software used in ANSYS workbench, from left ICEM CFD, Fluent and CFD Post.*

Because the flow pattern phenomena are multiphase and time dependent by nature, we have to use a transient solution model. Solver type is pressure based with absolute velocity formulation. Gravity function is turned on:  $g = -9.815 \frac{m}{s^2}$

### 3.6 Solution Models

#### 3.6.1 Multiphase flow simulation: The volume of fluid model (VOF)

The VOF model is an Euler–Euler model where the interface between the different phases is tracked. The model is suitable for stratified flow, free surface flows and movement of large bubbles in liquids. However, mixed internal flow systems with many small bubbles have many fluid interfaces, and because the interface between the fluids must be resolved, the VOF model is not suitable for these types of systems. For separated flows of immiscible fluids only the VOF model will work. The model predicts the location of the interface and uses single-phase models to predict the flow in each phase. The model requires a fine mesh to resolve the curvature of the interface (Andersson, 2012).

The VOF model uses the value of the volume fraction on a grid-cell basis to describe the position of the interface. The advective part of the equation is solved by special advection schemes, such as Lagrangian schemes, geometrical schemes and compressive schemes. These schemes can deal much better with cross-flow situations, and tend to be more mass conserving than their level-set counterparts.

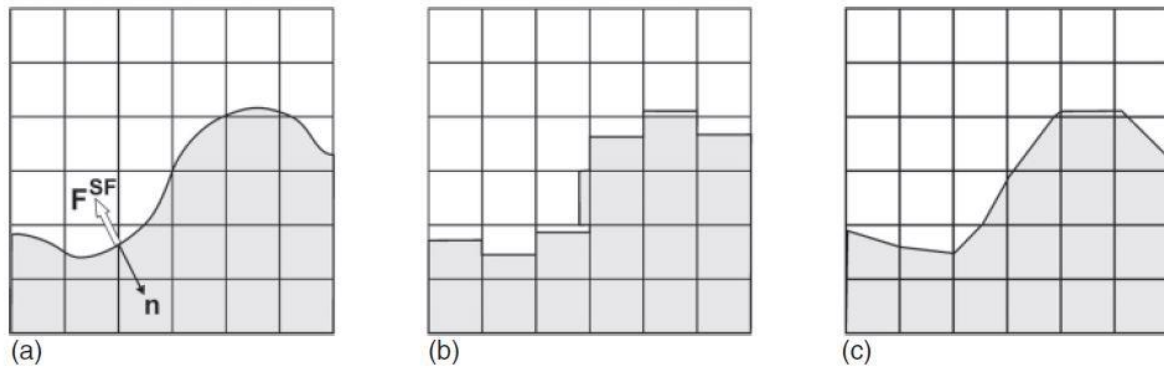


*Figure 3-6 -- VOF modelling of a fluid-fluid surface (a) represents the real surface, (b) the volume fraction calculated by the VOF model and (c) is the VOF models linear reconstruction of the surface*

Because of the linear reconstruction in each cell as seen in Figure 3-6, the model requires a large number of mesh cells, and Cartesian mesh cells makes VOF method more accurate. When generating the mesh for the simulation, a fine hexa-mesh is used, as this is the recommended mesh type for the VOF model. The flow from the inlet is separated, stratified flow, and thus the VOF model is the only applicable model for the simulations.

### 3.6.2 Viscous and turbulence model: Shear stress transport (SST) $k-\omega$

For turbulent and viscous model the SST  $k-\omega$  model is employed. SST model Uses  $k-\epsilon$  in the free stream and  $k-\omega$  in the wall-bounded region. This model works well with adverse pressure gradients and separating flow. However, it is required to use a fine mesh close to the wall, which in this case is the boundary layers around the tubes. Overprediction of turbulence in regions with large normal strain e.g. stagnation regions and strong acceleration regions still happen but it is more accurate than with the  $k-\epsilon$  model (Andersson, 2012)

The SST model was designed to give highly accurate predictions of the onset and the amount of flow separation under adverse pressure gradients by the inclusion of transport effects into the formulation of the eddy-viscosity. This results in a major improvement in terms of flow separation predictions. The superior performance of this model has been demonstrated in a large number of validation studies (Andersson, 2012). The SST model is recommended for high accuracy boundary layer simulations. (20) The medium mesh is depicted in Figure 3-7 and shows a zoomed view of the boundary layer.

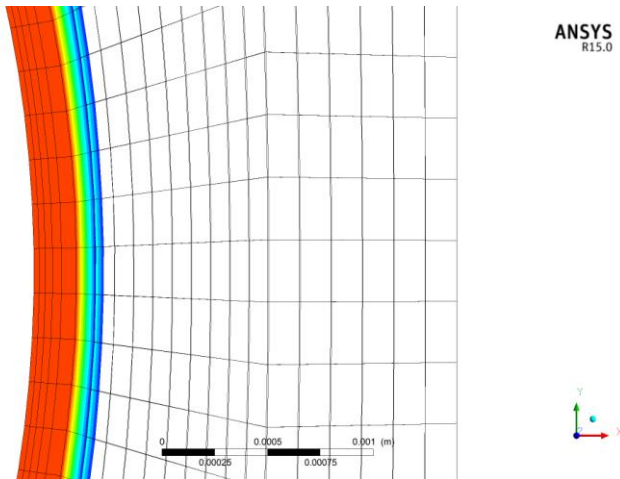


*Figure 3-7 boundary layer in the middle and tube interior at left. Extra fine mesh density. Red layer is liquid. Boundary layer thickness modeled at 0.2mm*

### 3.6.3 Energy equation

The energy equation is turned off in this preliminary study of flow patterns.

## 3.7 Materials and phases

It was preferred to use a single component refrigerant in the CFD simulations for simplifying reasons. And as the energy equation is not turned on, the effect of more than a single component can be neglected in the case of testing for different vapor fractions' influence on flow patterns.

### 3.7.1 Materials

Propane was used in all simulations. Relevant properties for liquid and vapor phase propane at was obtained using Refprop software with NIST Standard Reference database 23. The values at a pressure of 0.3MPa, shown in Table 3-2, were used in this preliminary study.

All material properties are assumed to be constants for simplicity.

Note that compared with air water standard properties, the density difference of liquid propane and liquid water are quite large and the surface tension  $7.28 \cdot 10^{-2} N/m$  for water at 20 degrees C is six times larger than the value looked at in this study for propane.

	Temperature (K)	Pressure (MPa)	Liquid Density (kg/m <sup>3</sup> )	Vapor Density (kg/m <sup>3</sup> )	Liquid Viscosity (μPa-s)	Vapor Viscosity (μPa-s)	Surf. Tension (mN/m)
1	230,74	0,10000	581,23	2,3868	197,89	6,3010	15,873
2	247,70	0,20000	561,15	4,5570	164,02	6,7417	13,526
3	258,97	0,30000	547,14	6,6780	145,49	7,0447	12,002
4	267,68	0,40000	535,89	8,7834	132,88	7,2884	10,847
5	274,88	0,50000	526,25	10,889	123,38	7,4990	9,9085
6	281,07	0,60000	517,67	13,005	115,78	7,6887	9,1129
7	286,55	0,70000	509,84	15,137	109,47	7,8644	8,4205
8	291,47	0,80000	502,59	17,291	104,08	8,0304	7,8063
9	295,96	0,90000	495,77	19,471	99,366	8,1894	7,2538
10	300,09	1,0000	489,30	21,681	95,187	8,3435	6,7515

*Table 3-2 Saturation points at equilibrium for Propane from 0.1Mpa to 1Mpa, generated using REFPROP Computer software.- NIST reference fluid properties*

### 3.7.2 Phases

Surface tension modeling is turned on. Wall adhesion is applied, Contact angle 30 degrees assumed between tube and liquid in all cases. Surface tension coefficient is kept constant at  $12,002 \cdot 10^{-3} N/m$ .

## 3.8 Boundary conditions

Temperature boundary conditions has been omitted from this study of flow patterns. No heat transfer is occurring, nor any evaporation or condensation.

### 3.8.1 Inlet

A velocity inlet is used. The normal settings for inlet conditions could not be met by merely using the inbuilt fluent functionality. A user defined function was needed to describe the inlet conditions. To determine the separate gas and liquid velocities and inlet void fraction, the method developed by (Feenstra et al., 2000) were implemented and found to improve the quality and consistency of the model.

#### 3.8.1.1 User defined function (UDF)

The UDF governs the inlet velocity, area and direction of the vapor and liquid phase and makes it possible to have two different phases enter through the same inlet. The width and position of the liquid film can be altered. The liquid film is positioned at the center of the inlet of the model. The inlet velocities are calculated separately for each case. This calculation is shown in section

4.2. The liquid is always entering from the center of the model inlet as a film directly over the center of the uppermost tube.

### *3.8.2 Outlet*

The outlet boundary layer is a pressure outlet. This allows for backflow of vapor phase, and is the most accurate option for VOF multi-phase flow models.

### *3.8.3 Tube walls*

Stationary wall boundary. Near wall no slip shear condition. The contact angle of liquid-vapor is modeled as 30°.

### *3.8.1 Left and right sides*

The left and right sides (along x-axis) are periodic. Fluid passing through the sides appear with the same properties and velocity at the other side. This is utilized to make the simulation more realistic. The solution should be the similar or the same as if the model had infinite periodic tube pairs along the x-axis.

### *3.8.2 Front and back sides*

The front and back (on the z axis) is modeled with the symmetry function. Ideally these boundaries should be periodic as well, but the software does not support more than one translational periodic boundary.

With the symmetry boundary employed, the fluid cannot pass through. However, the fluid has no friction with the boundary as it implies the fluid particle next to it outside the boundary has the exact same properties and velocity. This makes it more realistic than using a wall boundary.

## **3.9 Solution Methods:**

The SIMPLE scheme for pressure-velocity coupling is necessary due to turbulent flow modelling. SIMPLE is an algorithm that uses a relationship between velocity and pressure corrections to secure mass conservation and to obtain the pressure field. (20)

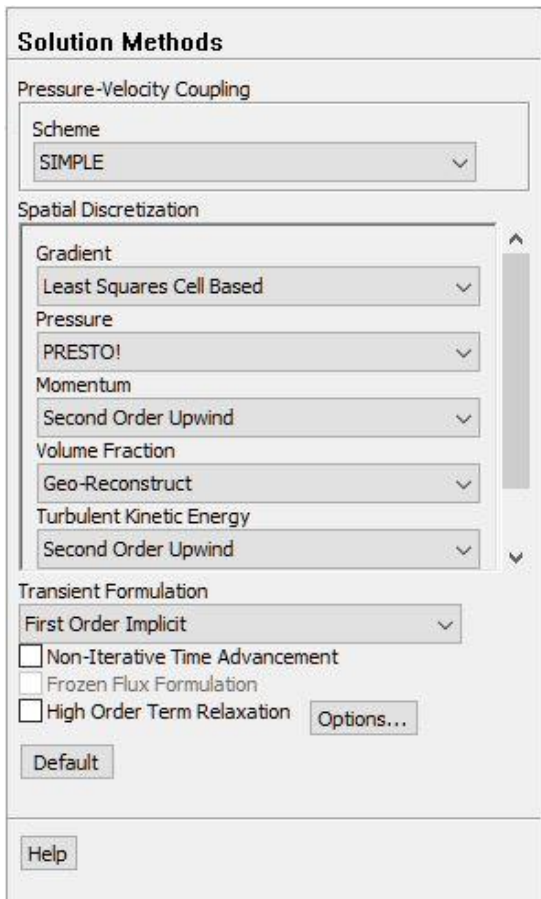


*Figure 3-8 Solution methods used for simulations*

The PRESTO! Scheme is recommended when using VOF. The PRESTO! Scheme calculates the pressure field on the faces of the model. It can do this by shifting the mesh so that the cell centers are where the faces of the original mesh was placed.

The geometric reconstruction scheme represents the interface between fluids using a piecewise-linear approach. In fluent this scheme is the most accurate and is applicable for general unstructured meshes. It assumes that the interface between two fluids has a linear slope within each cell, and uses this linear shape for calculation of the advection of fluid through the cell faces. However if the viscosity difference of the materials is high the Compressive Interface Capturing Scheme for Arbitrary Meshes (CICSAM) scheme might be better for convergence. The geometric

reconstruction interpolation scheme is typically used whenever you are interested in the time-accurate transient behavior of the VOF solution and

is thus chosen as the model for calculating volume fraction. However this scheme is more time consuming than other options. (20)

### 3.10 Calculation Activities

The time step used in all calculations are  $3e-5$  s and the number of time steps calculated are no more than 20 000. This gives a time interval between 0 - 0.6 s. Each solution is saved after 50 time steps, such that the incremental results can be viewed in the post processing software and animations of the flow can be made.

## 4. Methodology

### 4.1 Determining the inlet void fraction

An iterative method of determining the inlet cross sectional void fraction developed by (Feenstra et al., 2000) and described in Void fractions 2.4.1 was used. Initially a void fraction value is guessed and input in the mean gas velocity equation:

$$u_v = \frac{xG}{\varepsilon\rho_v} \quad \text{Equation 2-11}$$

This makes it possible to gain a value for S by using

$$S = 1 + 25.7 (Ri Cap)^{0.5} \left(\frac{P}{D}\right)^{-1} \quad \text{Equation 2-8}$$

And ultimately the output for void fraction can be found using

$$\text{Void fraction } \varepsilon = \left(1 + S \frac{\rho_v}{\rho_l} \left(\frac{1}{x} - 1\right)\right)^{-1} \quad \text{Equation 2-7,}$$

and the new value for the void fraction as put into  $uv = \frac{xG}{\varepsilon\rho_v}$

Equation 2-11 until finally the input and output are converged to the same number and the solution is found. The Void fraction number is then utilized in the inlet boundary condition to determine the inlet starting velocities of the liquid and vapor phases and their inlet cross sectional area. In addition the model developed by Feensra et al. (2000) operates as such that when the vapor quality is increased both the liquid and vapor inlet velocities are increased while the inlet width is reduced. This overcomes the problem of determining the starting inlet void fraction and will make the simulations closer to reality compared to increasing/decreasing the inlet liquid width linearly based on vapor quality. This is thought to shorten the needed length of the CFD model to obtain satisfactory data results.

### 4.2 Determining Inlet vapor and liquid velocities

Microsoft Excel was used to calculate and create table of the gas and liquid inlet velocities for the model. Two equations in addition to the aforementioned void fraction model were used to obtain the velocities; the vapor quality equation 4-1 and the conservation of mass equation 4-2.

$$X = \frac{\dot{m}_{vapor}}{\dot{m}_{vapor} + \dot{m}_{liquid}} = \frac{u_v \rho_v W_v}{\dot{m}_{TOT} W_{TOT}} \quad \text{Equation 4-1}$$

$$\dot{m}_{TOT} W_{TOT} = \dot{m}_l W_l + \dot{m}_v W_v = u_l \rho_l W_l + u_v \rho_v W_v \quad \text{Equation 4-2}$$

Total width  $W_{TOT}$  of inlet is 0.016 m. and the depth of the model is 0.010 m at all points of the model and can thus be neglected in calculations.

#### 4.2.1 Variables

The first variable to change gas and liquid velocities are the **vapor quality X**, ranging from 0-1 [dimensionless]. Range included this study is **0.01-0.7**

The second variable is the **Pressure**; which changes density, viscosity and surface tension between the liquid and vapor phases. In this study the pressure has been kept constant at **3 Bar**. This is similar and comparable to lab experiments.

Third variable is the **Total mass flux G**  $G = \frac{\dot{m}}{A} = 10 - 50 \frac{kg}{m^2s}$ . The range chosen is based on being comparable to lab experiments and that data is lacking in this range and is an important range for refrigeration purposes.

Equation 4.1 can then rearrange to give us the vapor velocities for the different variables as such:

$$u_v = \frac{X \cdot G \cdot W_{TOT}}{\rho_v W_v} \quad \text{Equation 4-3}$$

As the vapor velocity is then known, the liquid velocity can now be calculated using the conservation of mass in the control volume. A rearranging of equation 4.2 to yield  $u_l$ :

$$u_l = \frac{G W_{TOT} - u_v \rho_v W_v}{\rho_l W_l} \quad \text{Equation 4-4}$$

### 4.3 Test for Mesh independent solution

In order to save calculation resources and time, an evaluation of the necessary number of mesh cells for the 3D cases was conducted. Calculations with the same initial conditions are compared to check for deviations in flow pattern.

It was found that the mesh density significance of simulation quality, is dependent on the vapor quality of the simulation. Higher vapor quality means higher vapor flow rate. To satisfy the continuity equations the velocity of the vapor phase must thus increase as the vapor quality is increased. The flow is then more turbulent and a finer mesh will capture irregularities better.

#### *4.3.1 Operating conditions*

The different mesh densities; coarse mesh, medium mesh fine mesh and extra fine mesh were tested at

...vapor qualities of 0.1 and 0.3

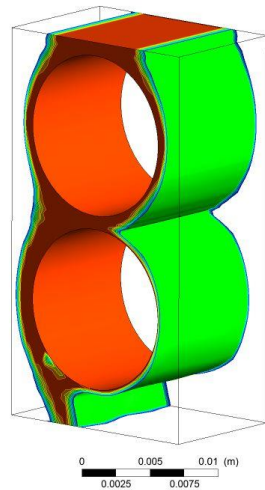
...a pressure of 0.6MPa and time step is set to  $3e-5$  for all cases.

#### *4.3.2 Quality 0.1*

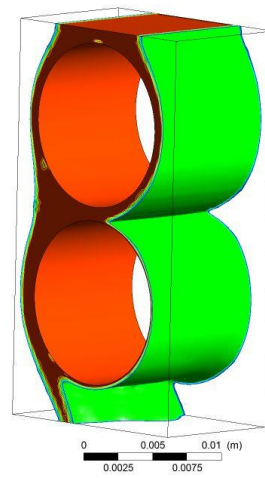
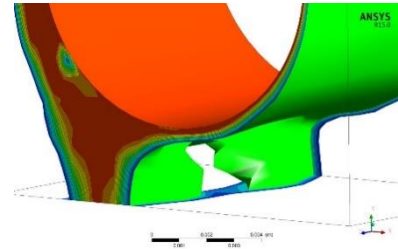
For this vapor quality, the vapor velocity is relatively small and the sheet falling film flow was established for all mesh cases, however, the coarse mesh resolution was found to be too low, which lead to inaccuracies in the depiction of the flow when the liquid sheet was discontinuous.

The medium mesh case shows acceptable resolution and a continuous sheet falling film flow is clearly established. After reaching a stable result in about 0.3s, the sheet never breaks up. The fine mesh was then tested to see if there were any discrepancies and to verify the medium mesh solution. The same result was obtained, however the liquid mostly flowed over the opposite side of the lower tube, compared to the coarse and medium solution. As the meshes are symmetric, the side of flow tendency is expected to be random. The fine mesh had a better resolution for the liquid film sheet and is thus chosen as the solution.

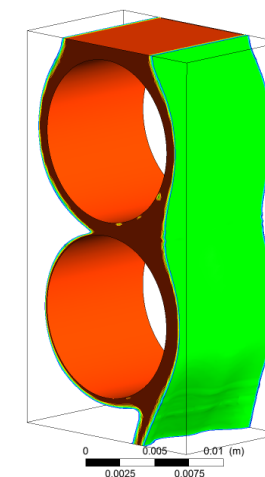
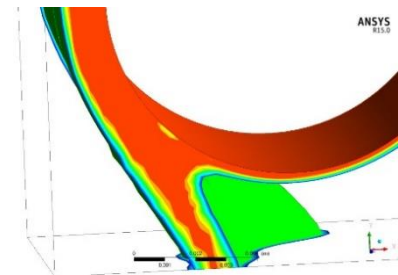
In conclusion, as shown in Figure 4-1, all meshes gave a similar result. However, in order to trust the accuracy of the solution, an acceptable resolution should use the medium mesh as a minimum for this and similar cases.



ANSYS  
R15.0



ANSYS  
R15.0



ANSYS  
R15.0

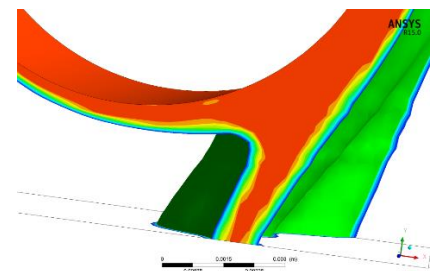


Figure 4-1 -- comparison of mesh solutions for vapor quality  $X=0.1$ . From top: coarse mesh, medium mesh and fine mesh. At the right side, a zoomed perspective of the outlet is shown.

### 4.3.3 Quality 0.3

#### 4.3.3.1 Coarse mesh: 4 cells/mm<sup>2</sup>

The simulation shows a twist phenomenon where the liquid mass-flow over the second tube is greatest at opposing sides in the z direction. The twist is shown in Figure 4-2 a). Almost all of the liquid mass flow exits at the sides of the model close to z=0mm and z=10mm. It is also evident that compared to the medium mesh, droplets of fluid are much less prevalent. The reason behind this being that the mesh cells are too large to capture and render droplets in the flow.

#### 4.3.3.2 Medium mesh: 17 cells/mm<sup>2</sup>

As is shown in Figure 4-2 b) the flow twist is even more pronounced in the case of the medium mesh. The flow is also generally more chaotic around the second tube. The gas-liquid interfaces are sharper, which yields more realistic results using the VOF multiphase method.

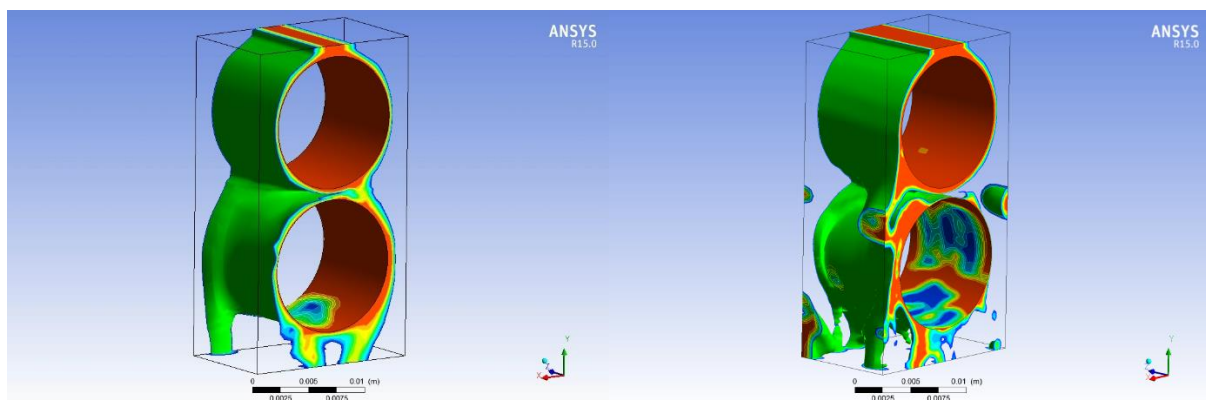
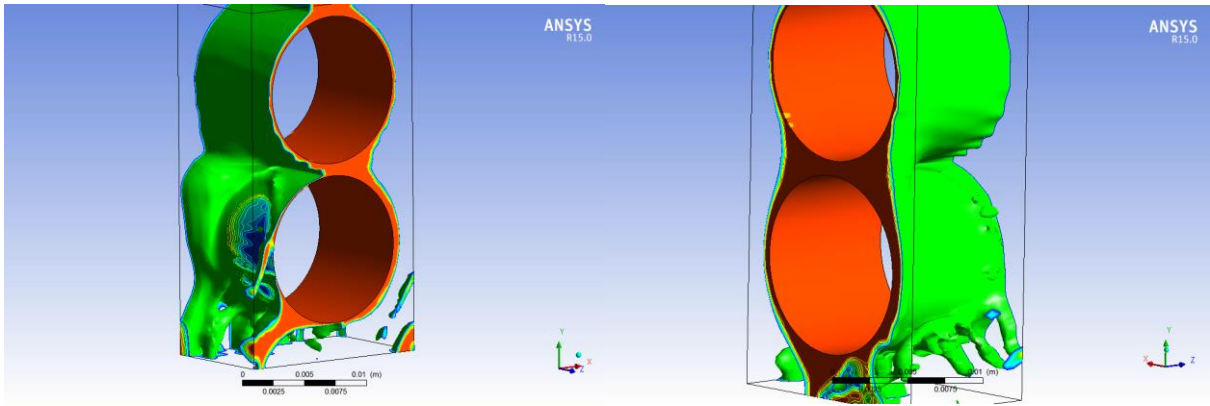


Figure 4-2 a) Coarse mesh at 0.4 seconds

b) Medium mesh at 0.4s

#### 4.3.3.3 Fine mesh: 32 cells/mm<sup>2</sup>

For this mesh density, the solution also involved the forming of a twist flow distribution. Interestingly the twist eventually stabilized at one of the sides in the Z direction. Here the flow on each side of the lower tube became more symmetric as seen in Figure 4-3.



*Figure 4-3 – Fine mesh solution at seen from front at time 0.4 seconds (left), and seen from the back side at 0.6 seconds when one side has become almost symmetrical in the x-y plane(right)*

#### *4.3.3.4 Extra Fine mesh: 47 cells/mm<sup>2</sup>*

At this mesh density the twist phenomena was seen again. This verifies that this phenomenon or something similar to it is likely to be realistic. However, the twist had a periodic back and forth motion. Additionally the tube surface is almost entirely wetted for the whole simulation period of 0.4s.

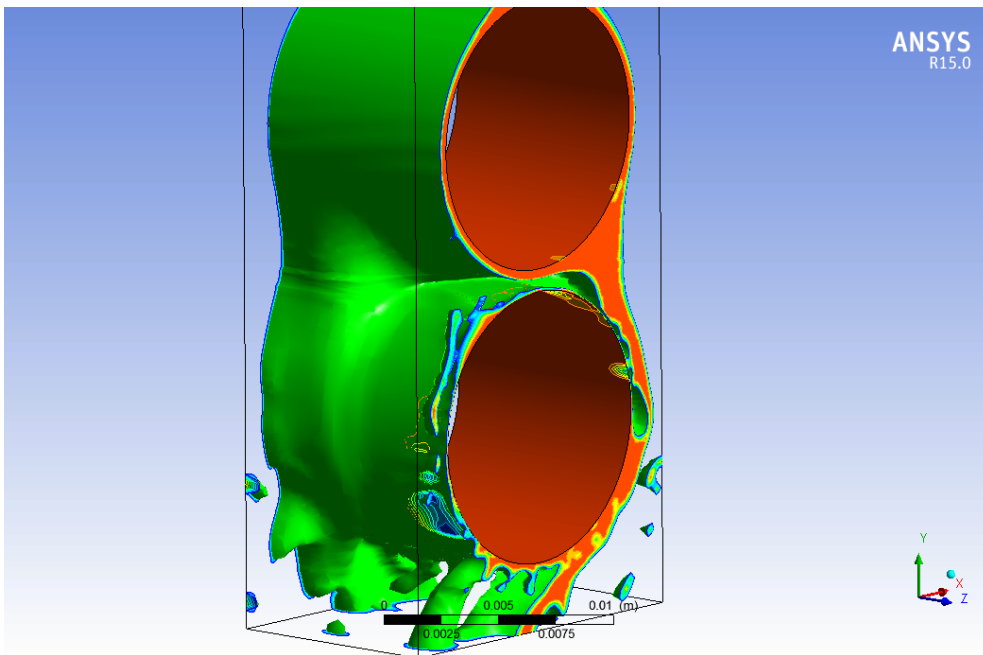


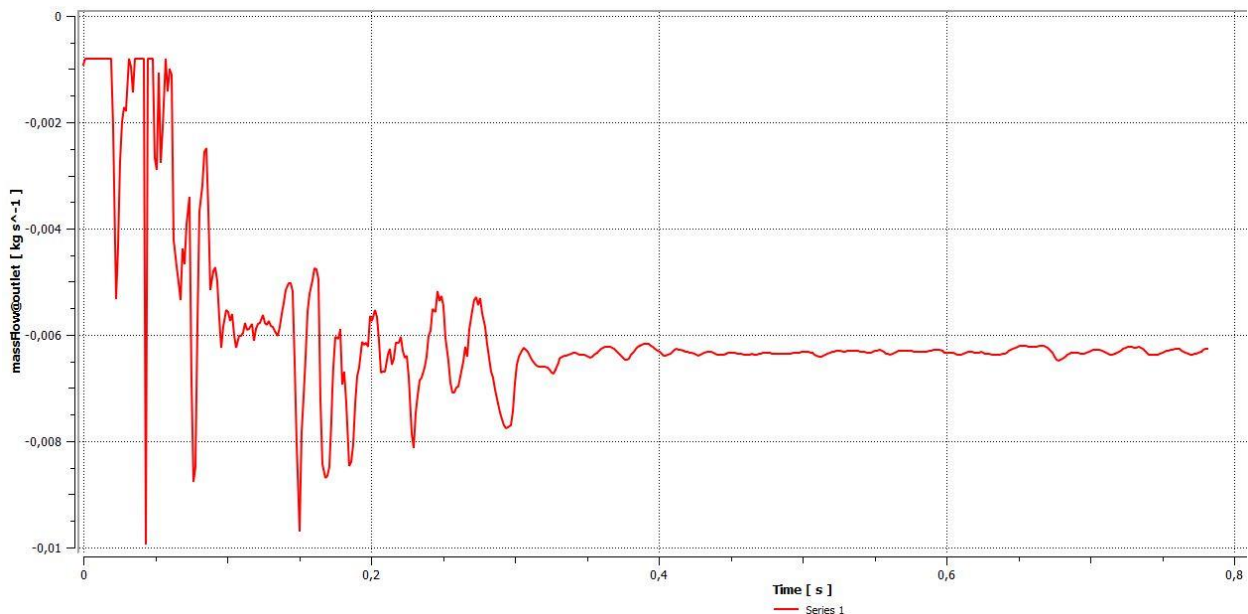
*Figure 4-4 -- extra fine mesh at 0.4s Twist phenomena occurring.*

#### 4.3.3.5 Conclusion:

The Fine mesh, with 32 cells/mm<sup>2</sup> works as the minimum mesh density for obtaining the flow patterns for the vapor fraction X=0.3 – 0,7 cases. For the purpose of consistency this mesh density will be used for all simulations with the 3 tube models.

#### 4.4 Verifying Mass flow integrity of simulations

A plot of the mass flow rate can be obtained by using the CFD Post software in ANSYS Workbench. The mass flowrate in the first milliseconds are low due to that the liquid has not yet reached the outlet. Later, as the liquid exits the outlet the graph jumps and drops violently due to liquid outflow intermittenencies. In the graph shown below the mass flow rate becomes quite stable after about 0,4s. The example given is the medium mesh 3D simulation with Z = 10mm, P= 0,6MPa and Vapor quality X = 0,1 where a continuous sheet flow was established after about 0.4 seconds.



*Graph 4-1 -- Mass flowrate for 3D simulation, quality X=0,1, Pressure P=0.6MPa, Specific mass flowrate 40kg/m<sup>2</sup>s medium mesh.*

The 3D model has an inlet and outlet area of:

$$A = 16\text{mm} \cdot 10\text{mm} = 160\text{mm}^2 = 0.000160 \text{ m}^2 = 1.6 \text{ e} - 4 \text{ m}^2$$

The correct mass flow rate through the outlet should then be:

$$-40 \frac{kg}{m^2s} \cdot 1,6 e - 4 m^2 = -0.0064 \frac{kg}{s} = -6.4 e - 3 \frac{kg}{s}$$

Graph 4-1 shows that the mass flow re-stabilizes around  $-6.4e-3 \frac{kg}{s}$  as expected. This particular graph shows a quite stable mass flowrate due to the continuous sheet flow established at this low vapor fraction.

After this stage it is important to check for the average mass flowrate of the simulation at the time interval used for the results. The data points of the graph is exported to MS Excel and the average mass flow rate can easily be averaged. Using this method the result obtained at the stable time interval is:  $0.4 s < t < 0.78 s = 6.32 e-3 \frac{kg}{s}$

The error of the mass flow is then  $0.08 e-3 \frac{kg}{s}$  and is a -1.25 % error compared to the desired value of  $6.40 e-3 \frac{kg}{s}$ . This value is then within the limits to simulate the  $40 \frac{kg}{m^2s}$  mass flowrate as 1-5% difference is expected to have negligible impact on flow patterns.

#### 4.5 Extracting measurements on the simulation models

The following procedure was used in order to obtain measurement data for void fractions both volumetrically and cross-sectional on the simulations.

The cross sectional area and velocity of the liquid phase and of the vapor phase was extracted and averaged. The measurements was taken at two different locations, in between the tubes and at 90 degrees of the lower tube as seen in Figure 4-5 marked with the purple and black cut planes respectively. The time interval measured in this way are between 0.50s to 0.60s. At this time interval the correct mass flowrate along the whole model is ensured.

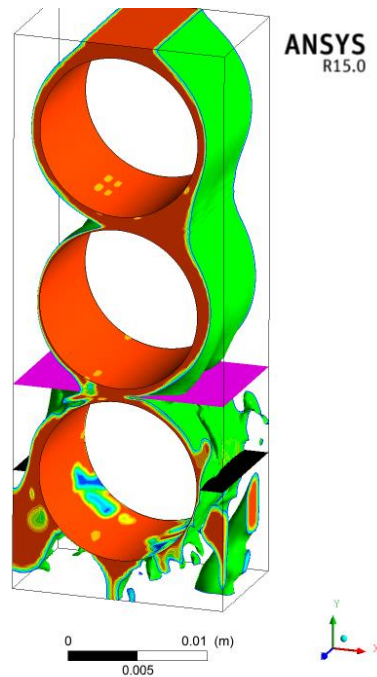


*Figure 4-5 – Measurement locations of vapor and liquid velocities and area fractions used to calculate superficial velocities. Black cut plane and purple cut plane was used and averaged. Quality X0.1 and flowrate G30 used as example here.*

Cross sectional void fraction measurements, vapor and liquid velocities were measured at these cut planes. In addition, the volumetric void fraction of the whole model was measured at the same time intervals.

## **5. Results and Discussion**

To improve the accuracy of the model an expansion to include a 3. tube was chosen in order to increase the accuracy of the results without too much of an extra calculation time cost.

### **5.1 Flow patterns**

The range of Reynolds numbers for the flow in this study are one order of magnitude higher than for the studies generally done on droplet-jet-sheet flow transition. This means that the flow patterns and terms coined by Mitrovich (1986) and expanded upon by Hu and Jacobi (1996) does not generally apply to these simulations. No strictly droplet, jet or sheet flow could be observed in the investigated ranges.

The previous researchers on flow patterns in tube bundle two phase flow have used many terms to describe their flow pattern observations, the terms best fitting and confirmed found in these simulations are those which can be called falling film (FF), intermittent flow (IN) and

Shear flow (or spray flow). The FF and IN have quite segregated liquid and vapor flow, with most of the liquid flowing over the tubes causing a film. For the SH however, all the liquid becomes fine droplets upon exiting the bottom of the liquid distributor tube (top tube).

- Falling film flow (FF): The liquid flow is continuous and have less disturbances by the vapor flow. The tube walls are almost completely wetted. Wavy patterns may form in the axial direction of the tube at higher flowrates. Few to no droplets flow with the vapor.
- Intermittent flow (IN): The vapor flow causes a more severe shear. The tubes are not always wetted and more serious dry spots can occur on the tubes. The slip ratio is increased and is the largest for this flow regime. Some liquid droplets are entrained in the vapor flow and the flow between tubes is much more disturbed.
- Shear flow/spray flow (SH): In This flow regime is easy to differentiate from the falling film flow and the intermittent flow. All the liquid is entrained in the vapor flow as small droplets. The slip ratio decreases again compared to (IN). No liquid film can be observed.

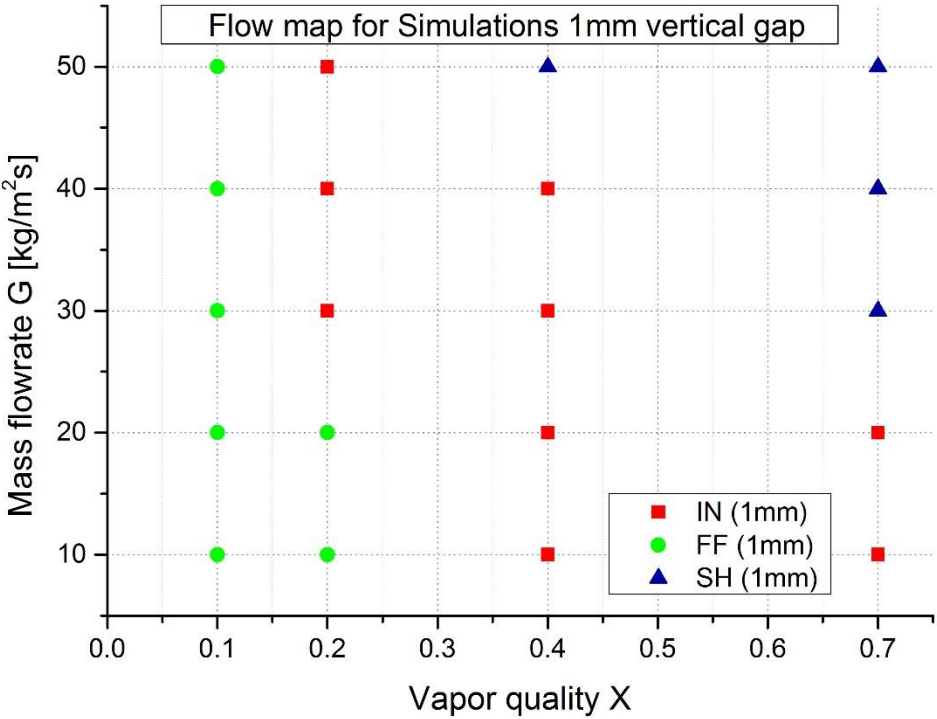


Figure 5-1 Flow map indicating flow mode transitions based on vapor quality and Mass flux over the in line tube bundle with 1mm vertical tube spacing.

### 5.1.1 Capillary length influence:

The capillary length of this fluid mixture is found to be shorter than that of the 1 mm tube gap model. According to  $\lambda_c = \sqrt{\frac{\sigma}{\rho_l g}}$

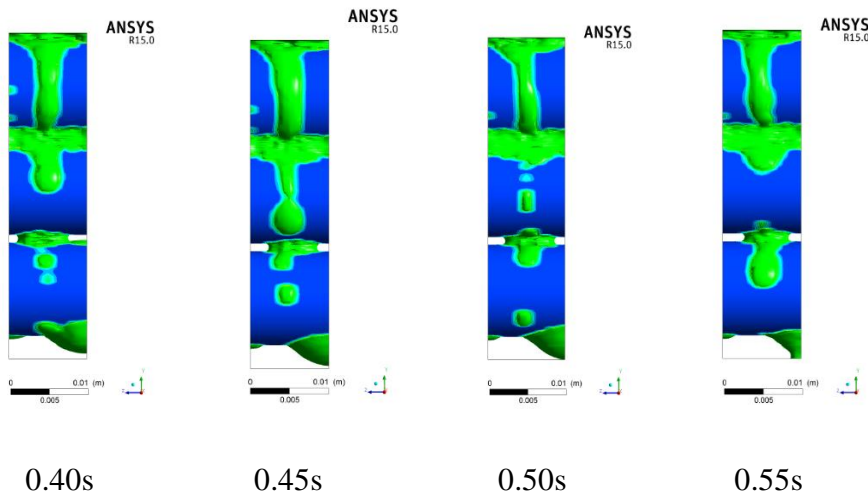
Equation 2-3, the capillary length of the propane at 3 Bar was calculated to be 1.5 mm. The 1 mm vertical tube gap model therefore has no way to demonstrate droplet flow. As the gap is not long enough for the droplets to form and slip from the upper tube without first hitting the tube below.

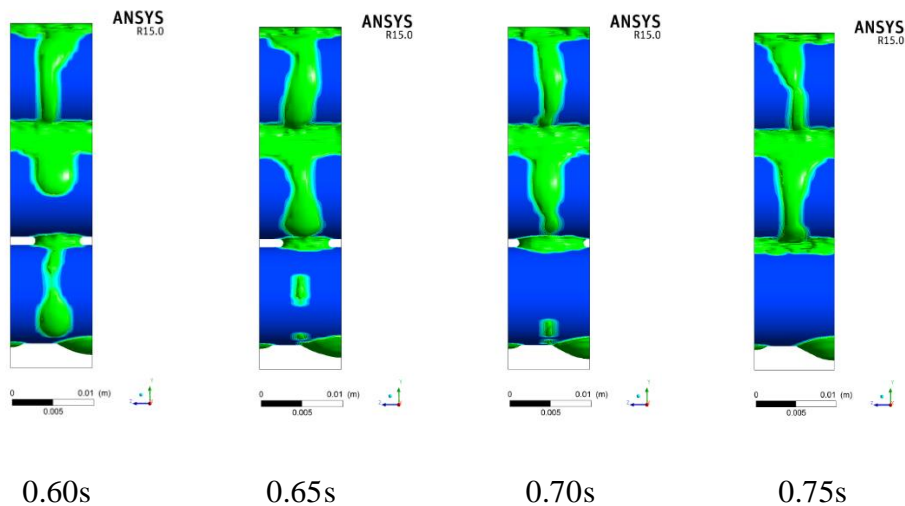
### 5.1.2 Droplet flow with water-air Simulation

In an attempt to produce droplet flow with the model, an Air-Water two phase flow was introduced at the inlet of the 1 mm gap model. Water was chosen as fluid as it was possible to achieve droplet flow at higher mass flows than for propane and the  $Ga^{0.25} = 443$ .

Following Figure 2-3 - Flow mode transitions when neglecting hysteresis (Hu and Jacobi, 1996) the Reynolds number for water should be below 100 and 25 was chosen to be safe within the limits of producing droplet flow.

Figure 5-2 - Water air simulation do induce droplet flow.  $X=0.0001$  and  $G=0.75 \text{ kg/m}^2\text{s}$ .  $Re_L = 25$





The simulation shows a tendency for the liquid to gather between the tubes, due to surface tension forces overcoming gravity. A layer is produced between the tubes until a droplet flows from the top of one tube and to the next along the side of the tube. At 0.55s a droplet has escaped the outlet and the liquid flowing from the 1. Gap to the 2. Gap starts filling the second gap until the gap is fully covered in water.

To see if the flowrate could be increased and still observe droplet flow the flowrate  $G$  was changed to  $1.785 \text{ kg/m}^2\text{s}$ . However the tube gap is too small to observe traditional columns of fluid between the tubes.

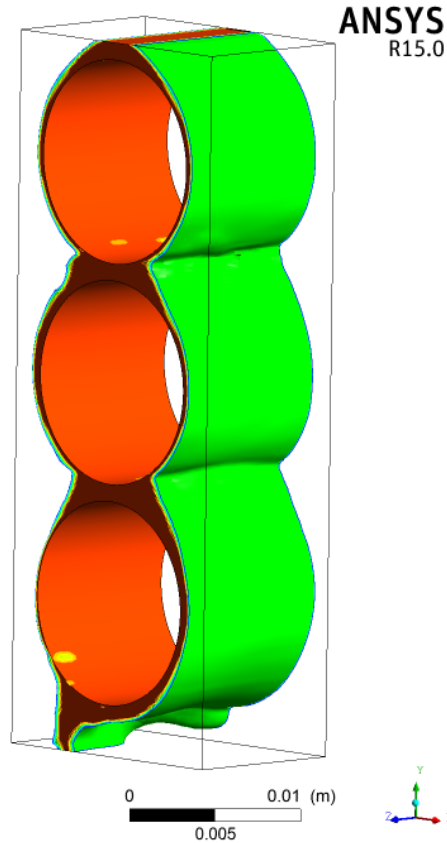


*Figure 5-3: Attempt to have wetted tube walls and droplet flow.  $X=0.0001$  and  $G=1.75$ .  $Re_L = 50$*

It is more similar to sheet flow, however the film thickness meets a drastic change at the bottom of the tubes where the liquid makes a sharp bend almost 90 degrees. The strong surface tension of water keeps a thick layer of water between the tubes.

For Propane at 3 Bar which is the target fluid in this study  $Ga^{0.25} = 681$  which is outside the range of Figure 2-3. Additionally the Reynolds numbers in this study ranges from 2000 – 11000. This means sheet flow, droplet flow and jet flows are not applicable terms for describing the flow in the tube bundle or the SWHE for the fluid, mass fluxes and vapor qualities tested in this study.

The largest difference between studies on falling film over open tubes and the aim of this study is that the vapor flow can in no way be neglected and that the flow is closed in a shell with neighboring tubes.

## 5.2 Slip ratio results

At the falling film flow regime, the slip ratios are quite small and reasonably within the range predicted by the Feenstra model.

However as the intermediate flow regime is approached a large discrepancy between the predicted S value and the measured S value is observed. The slip ratio can be huge locally, and reach values up to more than 200.

Then as the flow mode moves on to shear flow and vapor qualities typically are high, the two phase flow starts acting more homogeneously as droplets are caught and atomized in the vapor flow and the slip ratios become smaller for Quality 0.7 cases than for 0.1 cases.

CFD simulations have the advantage that Slip ratios can quite easily be measured, which can be very difficult in a real experiment. And thus little research has been done on the influence of this important parameter.

Table 5-1 – Results and predictions of velocity ratios/slip ratios in the simulated range. Flow modes marked with different colors: Green fields are FF, orange fields are Transition area (IN), and red is Spray flow (SH).

Averaged Slip ratios S Measured						
Quality/G	10	20	30	40	50	100
0.01			0.723			
0.05			2.7			
0.1	4.9	3.8	4.9	4.9	5.6	4
0.2	6.9	6.2	10.1	2.8	10.1	
0.4	23.9	23.1	12.4	48.6	40.3	
0.7	40.8	93.9	4.8	3.1	5	

Feenstra predicted S						
Quality/G	10	20	30	40	50	100 [kg/m <sup>2</sup> s]
0.01			3.2			
0.05			4.1			
0.1	8.5	5.9	4.9	4.3	3.9	3
0.2	10.4	6.2	6	5.3	4.8	
0.4	13	9.3	7.7	6.7	6.1	

0.7	15.9	11.4	9.5	8.3	7.5
-----	------	------	-----	-----	-----

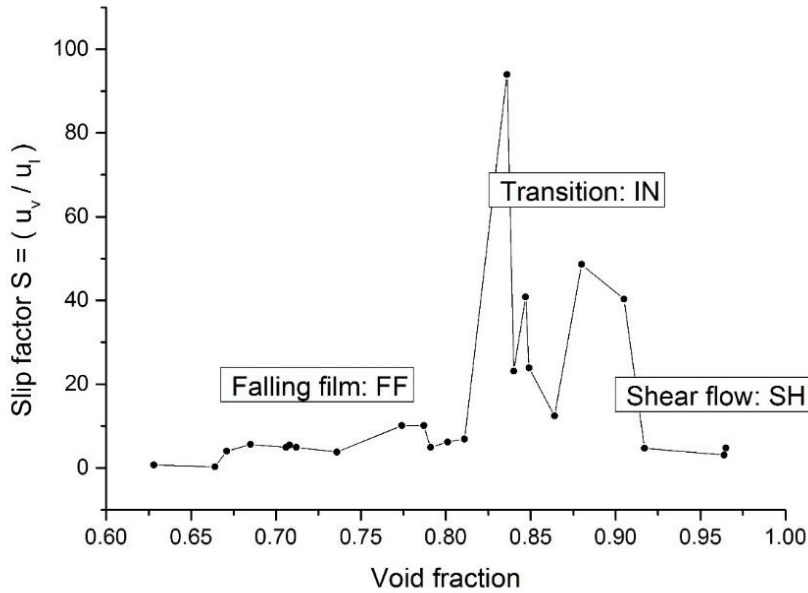


Figure 5-4 Slip factors  $S$  for all 1mm vertical tube gap simulations arranged after measured volumetric void fractions.

### 5.3 Void fraction results

Volumetric void fraction measurements gave a higher void fraction value than the measurement of the cross sectional averaged void fraction. Based on the volumetric void fraction, a pattern from the simulations occurred.

- Void fraction  $\epsilon$  1.00 – 0.9 : Shear flow, Spray flow (SH)
- Void fraction  $\epsilon$  0.90 – 0.75 : Intermittent flow (IN) , transition regime
- Void fraction  $\epsilon$  0.80 – 0.57 : Falling film flow (FF)

Table 5-2 – Void fraction measurement results

Volumetric void fraction measurement						
Quality/G	10	20	30	40	50	100 [kg/m <sup>2</sup> s]
0.01			0.628			
0.05			0.664			
0.1	0.791	0.736	0.712	0.706	0.685	0.671
0.2	0.811	0.801	0.774	0.719	0.787	
0.4	0.849	0.840	0.864	0.880	0.905	
0.7	0.847	0.836	0.965	0.964	0.917	

Cross sectional void fraction measurements						
Quality/G	10	20	30	40	50	100 [kg/m <sup>2</sup> s]
0.01			0.593			
0.05			0.596			
0.1	0.713	0.737	0.645	0.659	0.631	0.569
0.2	0.757	0.773	0.712	0.777	0.728	
0.4	0.762	0.738	0.884	0.829	0.948	
0.7	0.772	0.734	0.994	0.993	0.979	

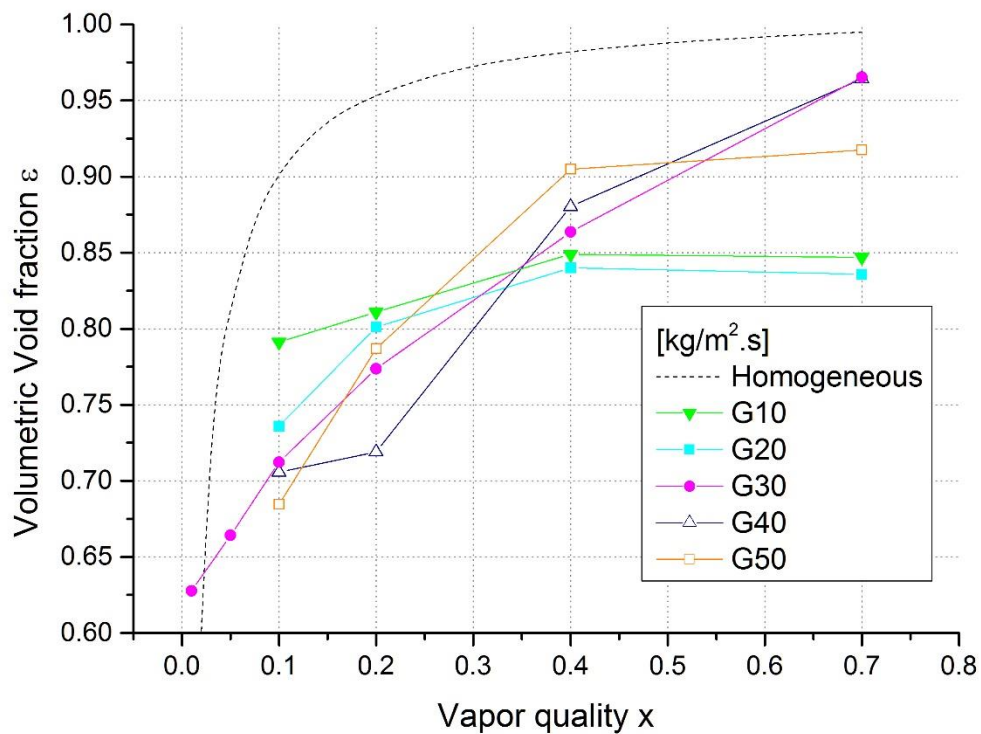
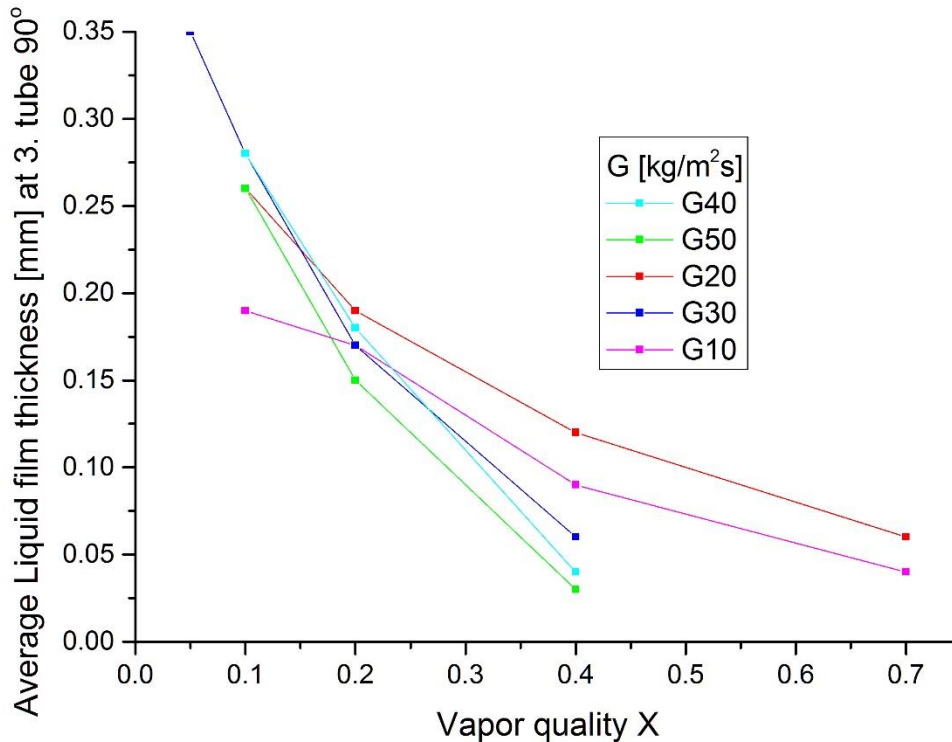


Figure 5-5 – Volumetric void fraction measurements for 1mm vertical tube spacing case

As the void fraction increased the liquid film thickness on the tube walls became thinner. This was an expected find. However the influence of the mass flux on the film thickness did not give any clear result. One pattern can be found at quality  $X = 0.4$  where increasing mass flow *decreased* the film thickness. This finding is coinciding with the finding that void fractions also increases with mass flow at this quality.



*Figure 5-6 – Film thickness measured at the lowest tube at the thinnest cross sectional area and where the velocity and thus film thickness were usually thinnest. Measurements for 1mm vertical tube spacing case*

### 5.3.1 Shear flow results $0.9 \leq \epsilon \leq 1$

As was expected, the void fractions increased as the vapor quality was increased. A sharp and most significant change in flow patterns occurred from intermediate to shear flow. No longer was there any liquid film flowing on the tubes. The liquid is entrained in the vapor flow as small droplets. The velocity of the liquid is now closer to the velocity of the vapor than at lower intermediate transition regime. Shown in Figure 5-7 is an example of the flow pattern of shear flow in the simulations. The liquid and vapor comes segregated in through the inlet but after the distribution tube the liquid is torn into small droplets by the vapor. The vapor flow can be seen by the streamlines on the right side of the figure.

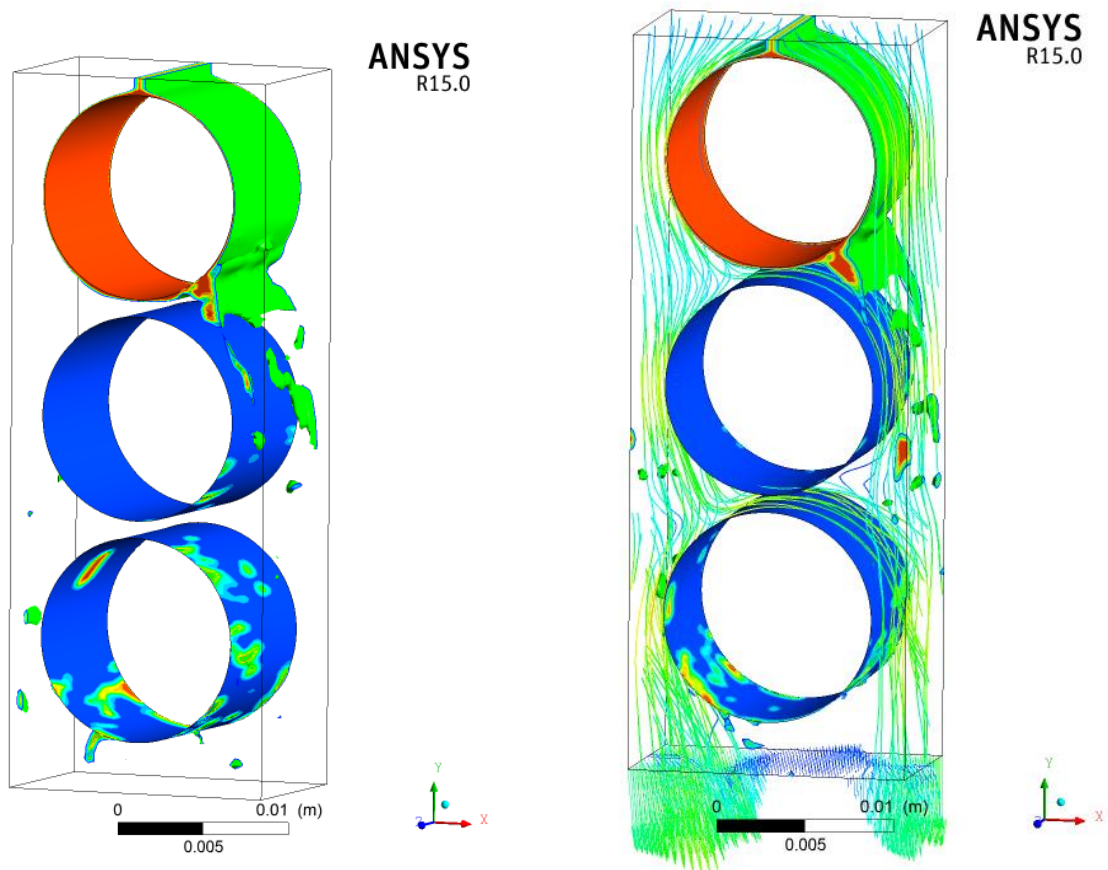


Figure 5-7 – Shear flow case example. Simulation vapor quality  $X = 0.7$  and mass flowrate  $G = 40 \text{ kg/m}^2\text{s}$

The Feenstra model predicted better than the homogeneous model in most cases. However at high vapor qualities the difference between the Feenstra and homogeneous model becomes less as the flow starts to act more like a homogeneous flow as can also be seen by the simulation results.

### 5.3.2 Intermittent flow/transition flow regimes $0.75 \leq \epsilon \leq 0.9$

Interestingly, in the case of  $G = 10 \text{ kg/m}^2\text{s}$  and  $G = 20 \text{ kg/m}^2\text{s}$ , the void fraction did not change significantly between quality  $x = 0.4$  to  $x = 0.7$ . The void fraction remained quite constant and even the different mass flow rate did not significantly influence the void fraction. The slip ratio was the highest measured of all the cases in these transition cases between intermittent flow and shear flow. Figure 5-8 shows an example of this type of flow. Vapor flows rapidly along the unobstructed middle but the liquid is quite stagnant in the middle

between the tubes with a very low average velocity. The tubes are wetted with a very thin film, and occasionally dry spots occur.

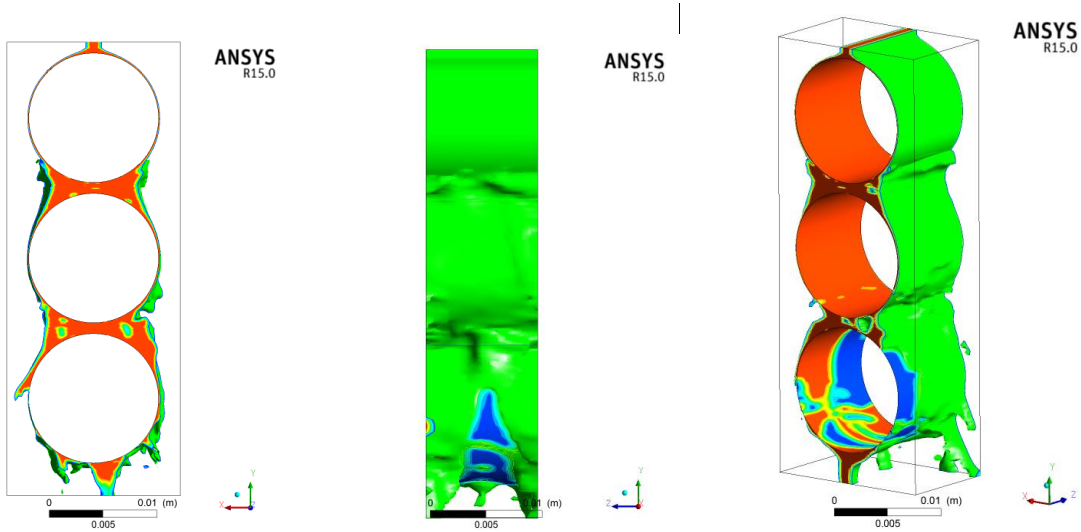
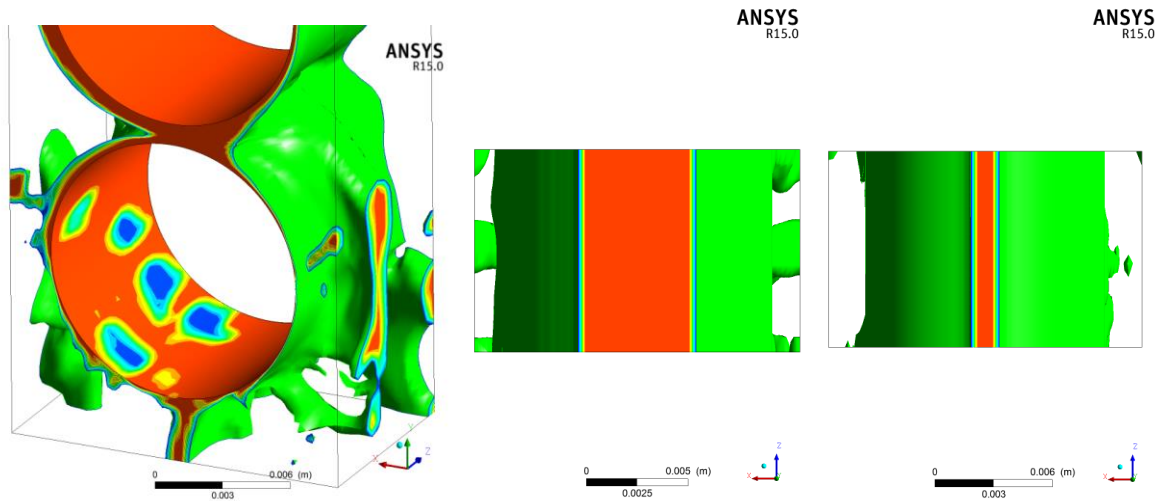


*Figure 5-8 – Quality 0.7 mass flux 20 kg/m<sup>2</sup>s – liquid film thickness is very low on the sides but liquid aggregates between the tubes in a larger degree. Occasional dry spots on the lower tube.*

The phase velocity difference is most dramatic in the largest cross section at the gap between the tubes as the average liquid flow is very slow here compared to the liquid flow before. This is what results in the extreme slip ratios of these cases. The vapor flow is only approximately halved between the thickest and the thinnest cross sections while the liquid velocity is reduced with a factor around more than 30.

5.3.3 *Falling film flow regime*  $\epsilon \leq 0.80$

In the falling film flow regime the liquid is flowing wavily along the tube. This means that along the Z direction (inward/outward) the liquid film layer has wave troughs and wave crests. This can be observed in Figure 5-9 a) and b). The liquid wave crest is often so high that it touches the next tube in the horizontal direction. As seen in b) this makes a channel where the vapor flows in the wave troughs.



a) Side view view comparison

b) Top view

c) Top view

Figure 5-9 – a) and b) Falling film flow regime  $G 30 \text{ kg/m}^2\text{s}$  and quality  $X = 0.1$ . c) compared to intermittent flow regime with high gas velocities represented by  $G 20 \text{ kg/m}^2\text{s}$   $X = 0.7$ .

This effect was even more pronounced as the vapor quality was set even lower than 0.1. For qualities 0.05 and 0.01 these waves were larger and less interrupted, in addition this made the average film thickness the highest measured at 0.35mm.

Another finding was that the liquid tends to go in a zig zag route down the tubes where most of the liquid flow passes on one side of the tube but still wets the side with a thinner film flow reasonably well. However, dry spots occur easier on the thin film flow side and usually in the bottom half of the tubes. This effect can be observed in Figure 5-10.

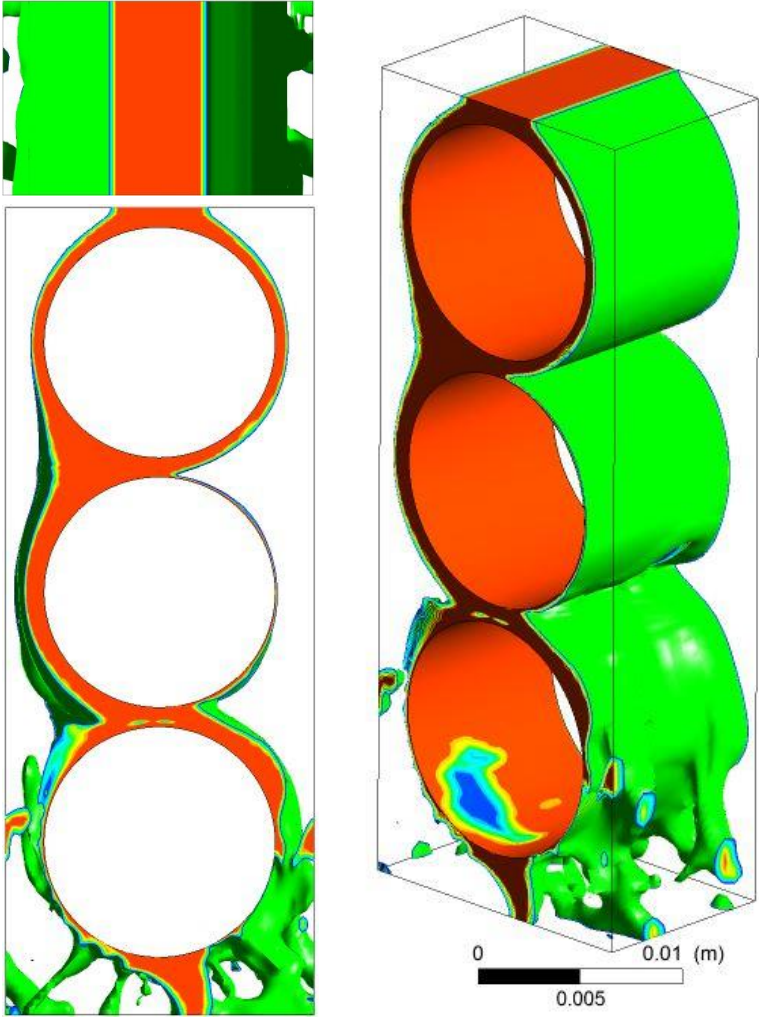


Figure 5-10 Falling film flow. G50 and X0.1 top front and side view at  $t=0.66s$

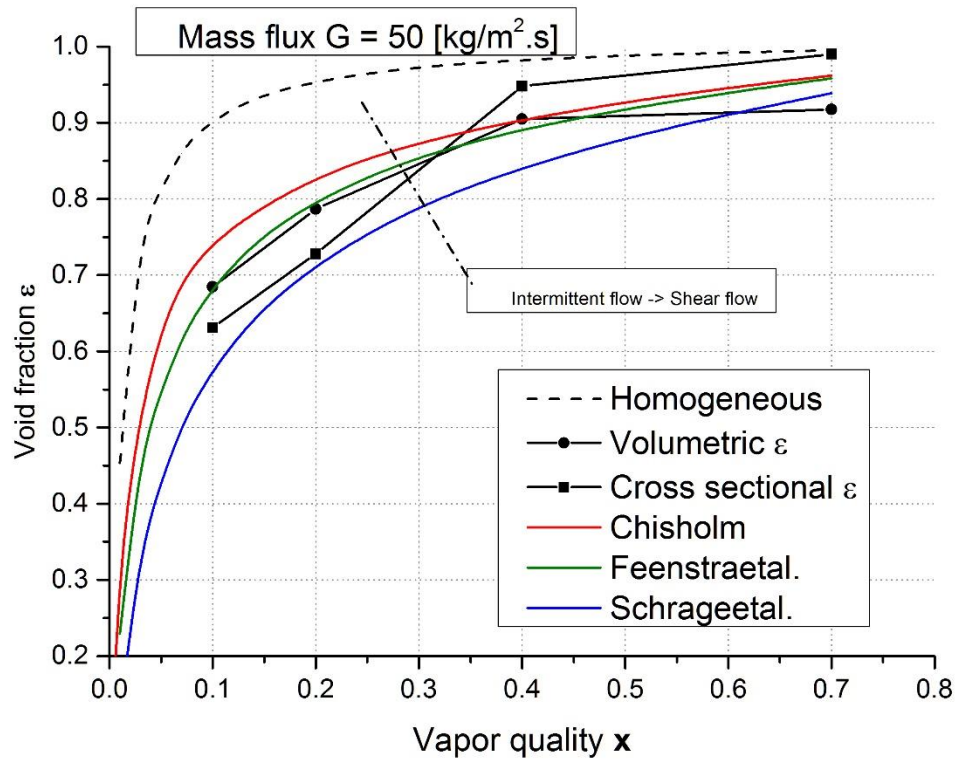
**5.4 Comparison with Void fraction prediction models**

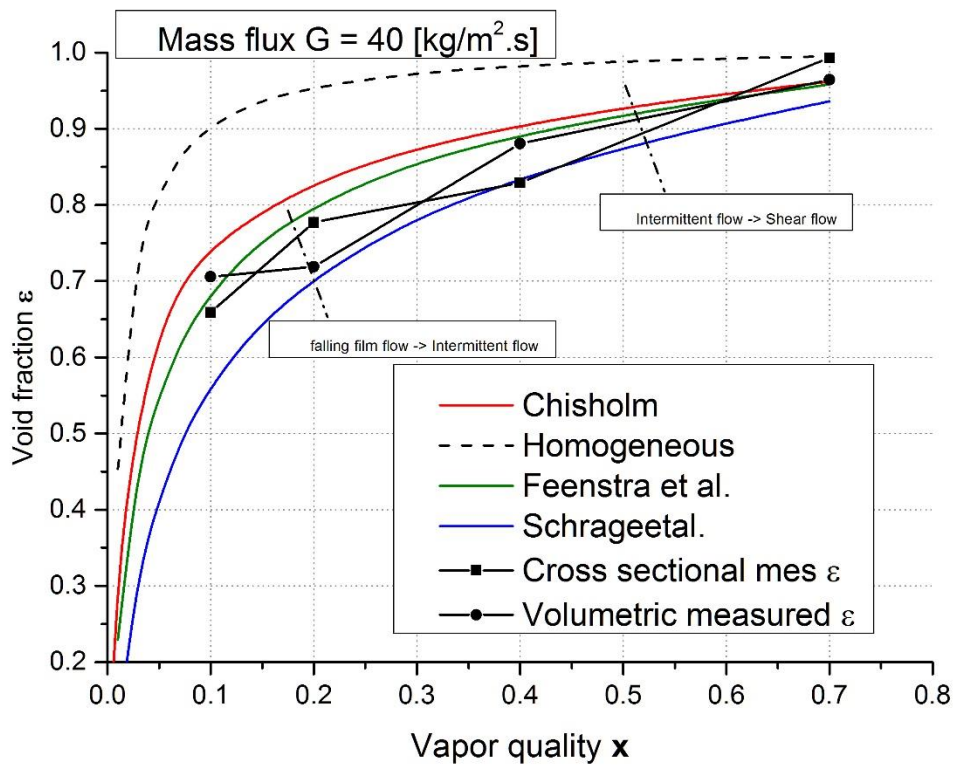
The most extensive prediction model is that of Feenstra-Weaver-Judd (2000) however, none of the prediction models fit the simulations perfectly. Special diversion of results was found at low vapor qualities. For vapor qualities  $X=0.1$  and below the Feenstra model under predicted the void fraction of the model quite drastically. But as mass flux was increased this result was better predicted again. Therefore it was observed that higher mass flow rates increase the accuracy of the prediction model drastically. This can be observed in Table 5-3

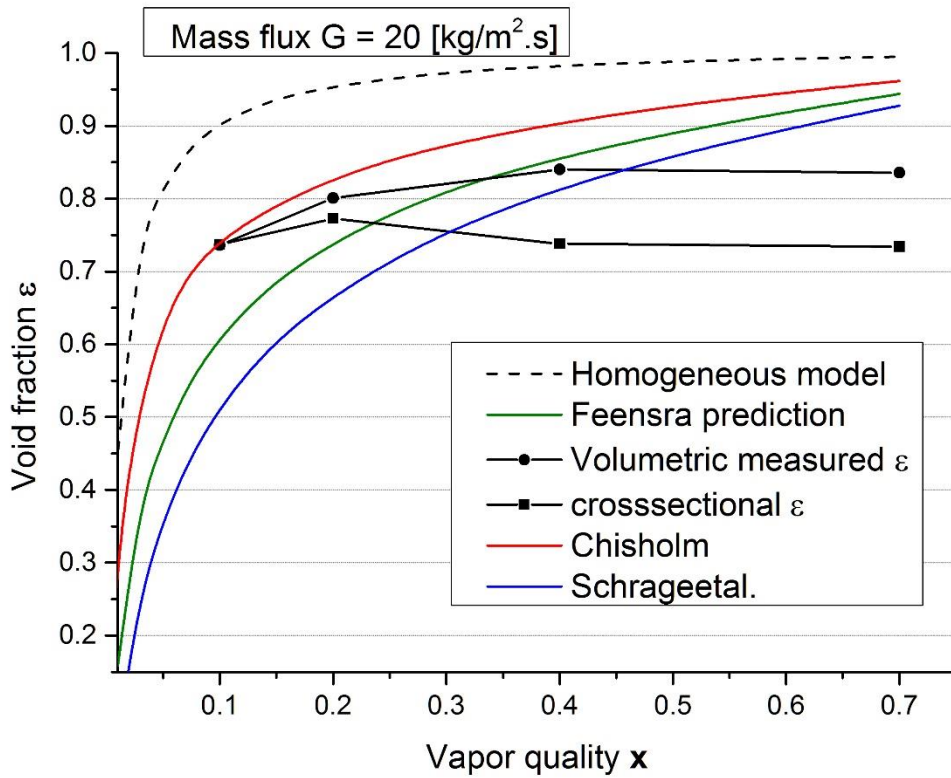
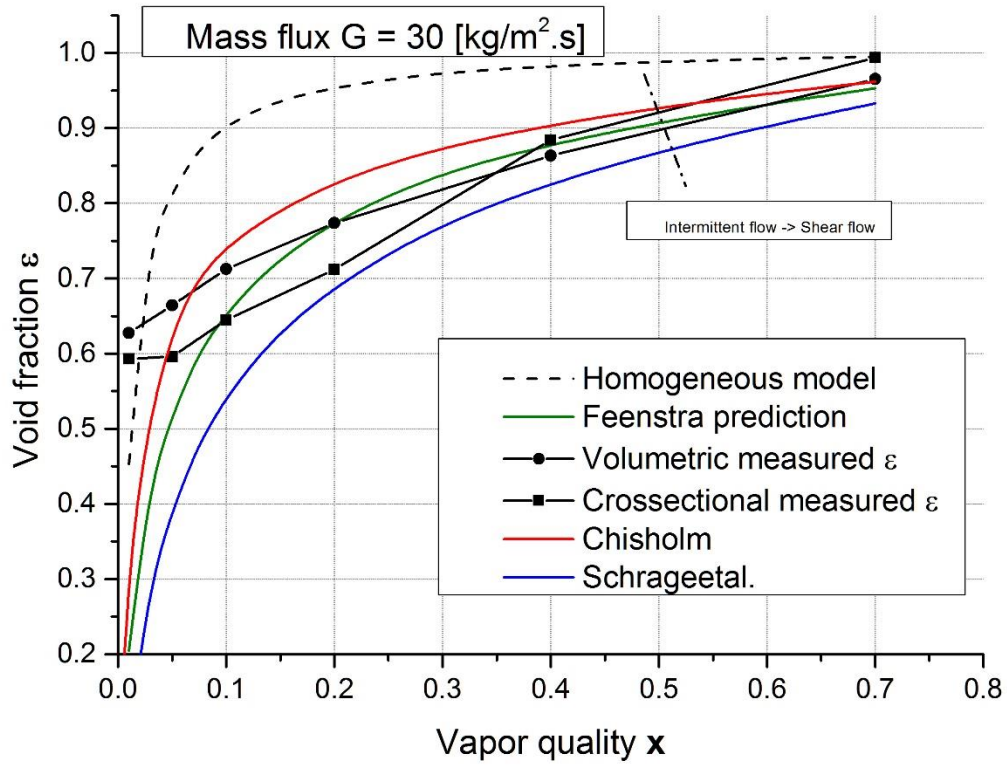
Table 5-3 Percentage difference between measured volumetric void fractions and the Feenstra-Weaver-Judd prediction model.

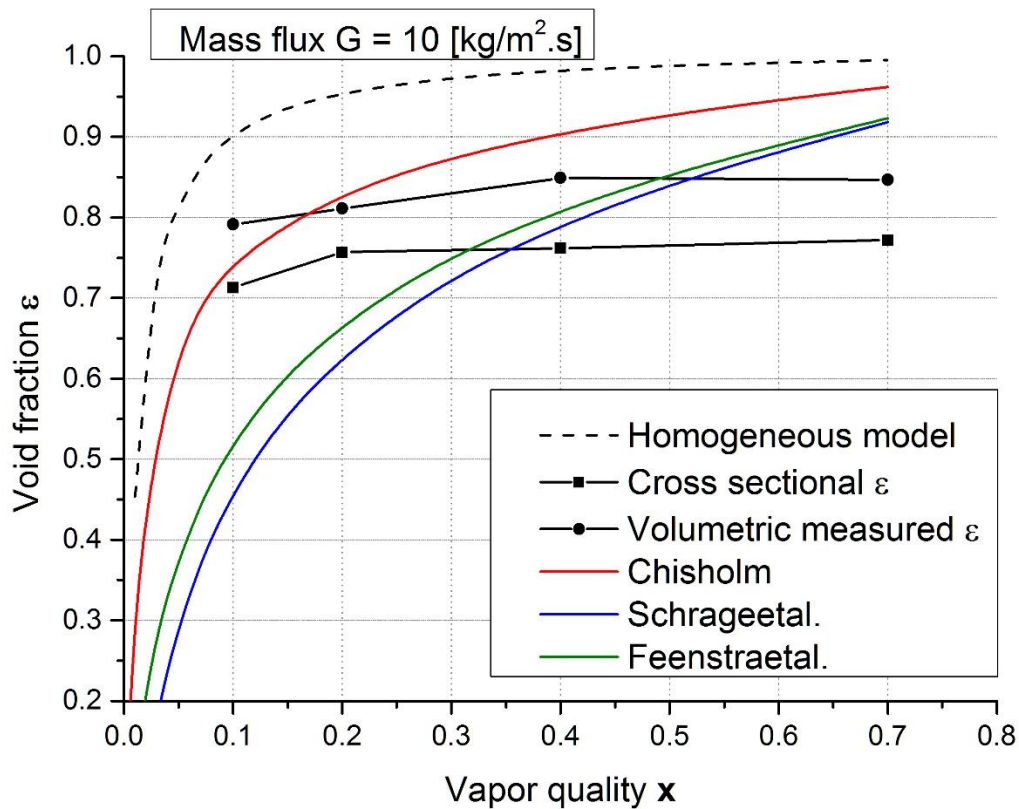
% difference Vol. Void fraction and Feenstra						
Quality/G	10	20	30	40	50	100
0.01			203.2			
0.05			28.7			
0.1	53.4	21.5	9.4	3.8	-2.3	-11.1
0.2	22.3	8.7	0.1	-11.0	-2.8	
0.4	5.2	-1.8	-1.5	-1.1	0.7	
0.7	-8.3	-11.5	1.3	0.7	-4.6	

Figure 5-11 - Comparisons of void fraction prediction methods for 1mm tube gap case, black lines and points are results obtained from simulations colored are estimations:









From the graphs it seems that the Chisholm correlation is better at predicting the void fraction at the lower vapor qualities and lower mass fluxes where the Feenstra model is not accurate enough. This can be observed in the G10 and G20 graphs where the Chisholm relation is much more accurate. However the Chisholm correlation does not include the influence of mass flow on the void fractions. The investigation of void fraction models by Harbin university (Wu et al., 2014) resulted in a recommendation of the Chisholm relation for alkaline flows in shell side of SWHEs. They did not however include the Feenstra-Weaver-Judd method in their analysis of 11 correlations for void fraction prediction.

It is clear that it is most problematic to estimate the void fractions for the falling film flow mode compared to the shear flow / spray flow regime. This is due to that at spray flow conditions the fluid acts more like a homogeneous flow and separation of the phases is not as dramatic as during film flow.

### 5.5 Results from 4mm tube gap

Only one flow rate was tested in the case of 4mm tube gap, 20 kg/m<sup>2</sup>s. As shown in the graph below the Chisholm correlation is most accurate in predicting the void fraction of the mass

flux G20 case. However the Chisholm correlation does not include any difference between different mass fluxes and is the simplest of the tested prediction models tested.

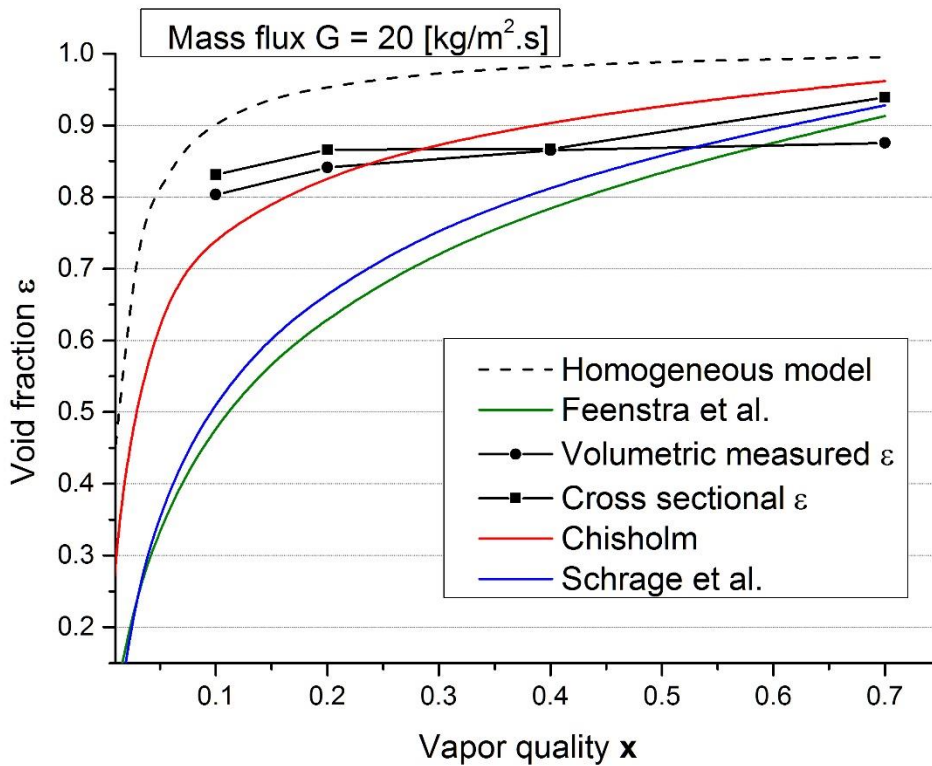
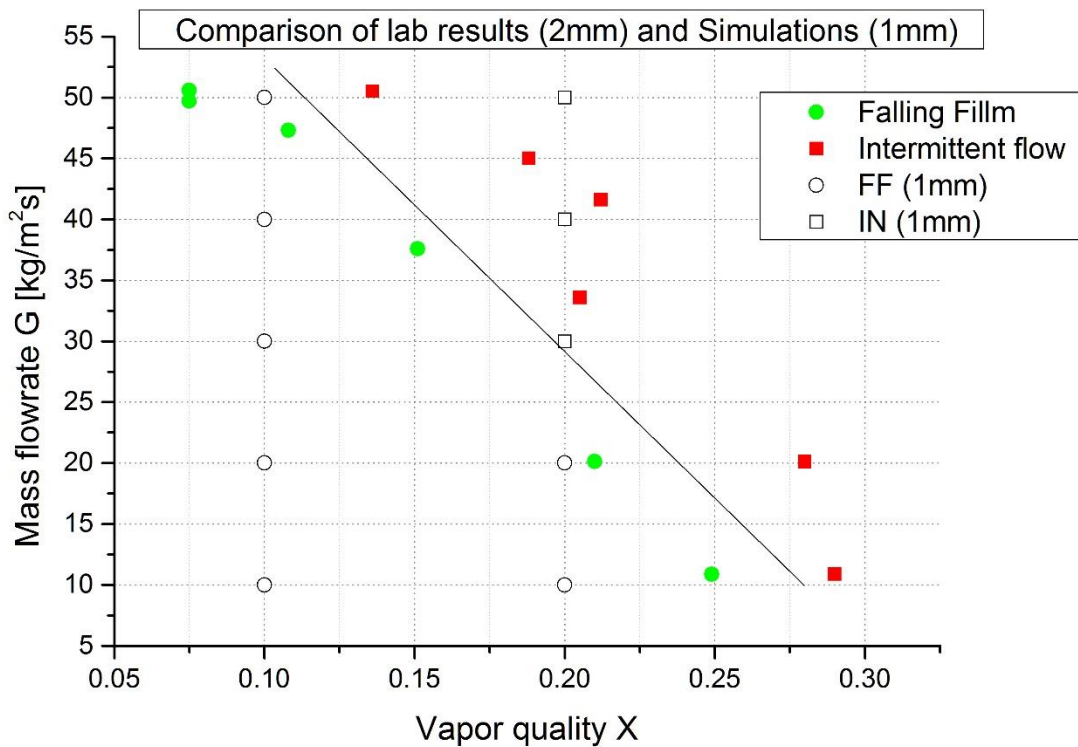


Figure 5-12 Comparison of void fraction prediction methods for 4mm tube gap case

The same void fraction relation to separate shear flow from falling film flow as described in section 5.3 applies to this geometry as well, meaning that the flow modes transition at similar Void fraction values. However, all simulations in this case have a higher void fraction than that of the 1mm case. Therefore the flow patterns are also different from the cases of G20 1mm. The larger tube spacing made it possible to achieve spray flow for the case of vapor quality X0.7, which was not observed in the 1mm tube gap case.

## 5.6 Comparison with results from laboratory experiment



*Figure 5-13 A comparison of the flow modes observed at specific vapor qualities and mass fluxes. The 1mm vertical tube gap simulations fit well with the 2mm Lab experiment observations.*

The main differences between the simulation and the lab experiment lies in that the lab experiment has angled tubes in alternating fashion, one single whole tube in the middle and half tubes spiraling in the opposite direction along the wall of the test section. In addition the lab experiment has more tubes in front of the tested area which gives better flow stabilization before measurement.



*Figure 5-14 – left: Falling film flow and Right: Intermittent flow. Propane at 4.5 bar from observations at the Lab set up in SJTU.*

## **5.7 Sources of error**

### *5.7.1 CFD Model*

The geometry is made as simple as possible to reduce calculation times, inlet entrance length and outlet exit length from tube to outlet and inlet is kept as small as possible to conserve time. Also only three horizontal tubes are used in most of the simulations for simplicity, more tubes would obtain clearer results of flow patterns and measurement data, but would come at a substantial processing cost. More tubes would stabilize the flow better and reduce entrance and exit effects on the measurements.

Another source for error is the length of the model in the z direction. 10mm was chosen but in reality the longer the model would be in the z direction the more accurate the obtainable results would be. The reason behind this being interference from the front and back wall of the simulation, which interferes due to the fact that liquid cannot cross this boundary. Also the flow patterns in the z direction could be more easily observed and shown to be repeated along the whole tube or if this boundary also could be made periodic, which as to the authors' knowledge is not possible. Results such as the columnar flow may need a longer tube in the Z direction to be observed in the simulations.

## 6. Conclusions

Correlations for flow patterns and void fractions have been made using a CFD model of a horizontal, in-line arranged, tube bundle. The simulation results in flow patterns have been compared to the measurements done on an experimental lab at Shanghai Jiao Tong University. The CFD model is a simplified model of the lab experiment, which is made to resemble conditions in a SWHE. Propane has been used as the primary fluid component in this study and in all included measurements.

The work can be split into two topics; flow pattern theory over horizontal tubes and two-phase CFD modelling and simulation.

As much of the knowledge and studies with the purpose of improving the process of designing SWHEs are of proprietary nature, this study adds valuable insights and methods which can be expanded and built upon. In the field of multi-phase flows most of the attention and knowledge are about internal flows in tubes, while less is known about shell side flows. Shell side flows are more complicated and variable in geometry and hydrodynamics than typical in-tube flows and are thus more challenging to predict and simulate.

Previous research on two phase flow modes over horizontal tube bundles and horizontally aligned tubes have been the foundation of much of the findings.

Previous researchers have focused little on the flow rates 10-50 kg/m<sup>2</sup>.s and Propane. This study have expanded the knowledge on flow modes in this range.

Little available research with such a small pitch to diameter ratio have been done.

- Confirmed that: as vapor shear get higher by increasing vapor quality the influence of gravity becomes more negligible, eventually resulting in spray flow.
  - This transition of flow modes took place for the most part in a void fraction range of  $0.84 \leq \epsilon \leq 0.9$
- Feenstra-Weaver-Judd model predicts void fraction values best at higher mass fluxes and vapor qualities in the tested range and is recommended for future predictions. However, at mass flows below G20 caution is advised in the low quality range where Chisholm's method is more applicable.

- In the transition from film flow to spray flow the velocity difference (Slip ratio)  $S$  of liquid and vapor become very high before lowering itself when finishing the transition to shear flow and the flow becomes more homogenic as the spray flow pattern ensues.
- Increasing the mass flux at constant vapor quality hurries the transition to the next flow pattern, this is due to higher vapor velocities for these cases.
- Increasing the Pitch (tube gap) was found to increase the void fraction and therefore hurry the onset of flow mode transitions.
  - The low pitch in the 1 mm vertical tube gap case postpones the onset of spray flow. This was observed when comparing the data between 4mm and 1 mm tube gap for  $G=20 \text{ kg/m}^2\text{s}$  quality 0.7 and 0.4.

## 7. Recommendations for future work

Investigate the void fractions influence on the flow pattern in the lab heat exchanger. If the void fractions at different locations inside a live SWHE could be measured during operation, then it could be possible to determine the transitional points of flow modes and the location of these transitions in the heat exchanger. The gamma ray attenuation method could be a serving candidate for doing that kind of measurements as it is totally non-intrusive to the system and no windows or sight glass is necessary.

The use of these CFD models to predict void fractions in tube bundles could be improved by increasing the number of tubes. Three tubes are experienced as a minimum requirement for obtaining this data.

The model can be expanded to include heat transfer and phase change as well as pressure drop simulations.

More studies are needed to develop a better and more extensive model for predicting void fractions and pressure drop for a wider range of fluids geometries, flowrates, and vapor qualities for shell-side two phase flow, there is still work to be done in making a model that takes all fluid and geometrical properties into account and that can produce a reliably good estimate of the void fraction for the whole range of mass fluxes and vapor qualities.

## References

- ANSYS *Fluent user guide* [Online].  
<https://www.sharcnet.ca/Software/Fluent6/html/ug/node888.htm>.
- ANDERSSON, B. 2012. *Computational Fluid Dynamics for Engineers*
- ARMBRUSTER, R. & MITROVIC, J. Patterns of falling film flow over horizontal smooth tubes. INSTITUTION OF CHEMICAL ENGINEERS SYMPOSIUM SERIES, 1994. HEMISPHERE PUBLISHING CORPORATION, 275-275.
- AUNAN, B. 2000. *Shell-side Heat Transfer and Pressure Drop in Coil-Wound LNG Heat Exchangers, laboratory measurements and modelling*. Ph.D. Experimental NTNU.
- BG-GROUP. 2014. *Global LNG Market Outlook 2014-15* [Online]. Available: <http://www.bg-group.com/480/about-us/lng/global-lng-market-outlook-2014-15/> [Accessed 15.04 2015].
- CHEN, X. Y. 2014. *Pipeline natural gas supply affects liquefied natural gas carriers* [Online]. marketrealist.com. Available: <http://marketrealist.com/2014/05/why-pipeline-natural-gas-supply-affects-lng-trade-and-carriers/> [Accessed 15.04.2015].
- FEENSTRA, P. A., WEAVER, D. S. & JUDD, R. L. 2000. An improved void fraction model for two-phase cross-flow in horizontal tube bundles. *International Journal of Multiphase Flow*, 26, 1851-1873.
- FERNÁNDEZ-SEARA, J. & PARDIÑAS, Á. Á. 2014. Refrigerant falling film evaporation review: Description, fluid dynamics and heat transfer. *Applied Thermal Engineering*, 64, 155-171.
- GRANT, I. & CHISHOLM, D. 1979. Two-phase flow on the shell-side of a segmentally baffled shell-and-tube heat exchanger. *Journal of Heat Transfer*, 101, 38-42.
- HU, X. & JACOBI, A. M. 1996. The Intertube Falling Film: Part 1—Flow Characteristics, Mode Transitions, and Hysteresis. *Journal of Heat Transfer*, 118, 616-625.
- JAFAR, F. A., THORPE, G. R. & TURAN, Ö. F. 2010. Falling Film Transition and Heat Transfer on Horizontal Circular Cylinders. *Australasian Fluid mechanics conference*. Auckland, New Zealand.
- JOHN G. BUSTAMENTE. 2014. *Falling-Film Evaporation over Horizontal Rectangular Tubes*. Master, Georgia Institute of Technology.
- JOHN R. THOME 2010. *Engineering Data Book III*, Wolverine Tube, Inc.
- KONDO, M. & NAKAJIMA, K.-I. 1980. Experimental investigation of air-water two phase upflow across horizontal tube bundles: Part 1, flow pattern and void fraction. *Bulletin of JSME*, 23, 385-393.
- MITROVIC, J. 1986. Influence of tube spacing and flow rate on heat transfer from a horizontal tube to a falling liquid film. *Proceedings of the 8th International Heat Transfer Conference*, 4, pp. 1949–1956.
- MITROVIC, J. 2005. Flow structures of a liquid film falling on horizontal tubes. *Chemical engineering & technology*, 28, 684-694.
- MOKHATAB, S. 2013. *Handbook of LNG*.
- NOGHREHKAR, G. R., KAWAJI, M. & CHAN, A. M. C. 1999. Investigation of two-phase flow regimes in tube bundles under cross-flow conditions. *International Journal of Multiphase Flow*, 25, 857-874.
- PETTERSEN, J. 2012. *Compendium LNG Technology*.
- RIBATSKI, G. & JACOBI, A. M. 2005. Falling-film evaporation on horizontal tubes—a critical review. *International Journal of Refrigeration*, 28, 635-653.

- SCHRAGE, D., HSU, J. & JENSEN, M. 1988. Two-phase pressure drop in vertical crossflow across a horizontal tube bundle. *AIChE journal*, 34, 107-115.
- THOMLINSON, C. 2015. *Japan's resumption of nuclear power bad news for natural gas* [Online]. [www.houstonchronicle.com](http://www.houstonchronicle.com). Available: <http://www.houstonchronicle.com/business/outside-the-boardroom/article/Japan-s-resumption-of-nuclear-power-bad-news-for-6437472.php> [Accessed 28.10 2015].
- WU, Z.-Y., CAI, W.-H., QIU, G.-D. & JIANG, Y.-Q. 2014. Prediction of Mass Transfer Time Relaxation Parameter for Boiling Simulation on the Shell-Side of LNG Spiral Wound Heat Exchanger. *Advances in Mechanical Engineering*, 6, 275708.
- XU, G. P., TSO, C. P. & TOU, K. W. 1998. Hydrodynamics of two-phase flow in vertical up and down-flow across a horizontal tube bundle. *International Journal of Multiphase Flow*, 24, 1317-1342.

## Appendix A.1 - Experimental setup and results

Simulations using CFD software emulates the parameters and dimensions of the shell-side of a SWHE from a lab set-up at SJTU. The lab experiments are influenced by the previous experiments done by Aunan in 2000 the Norwegian University of Science and Technology (Aunan, 2000).

### *Important lab experiment parameters*

The experiment has min max values for pressure, temperature, vapor fraction and mass transfer which will be reflected in the simulations.

property	value
<b>Temperature</b>	-150°C ~ 0°C
<b>Pressure</b>	0,2 - 0,6 MPa
<b>Mass flowrate</b>	$10 \frac{kg}{m^2s} \sim 60 \frac{kg}{m^2s}$
<b>Vapor fraction</b>	0 – 1
<b>Heat transfer coefficient</b>	0 ~ 10 000 W/m <sup>2</sup>

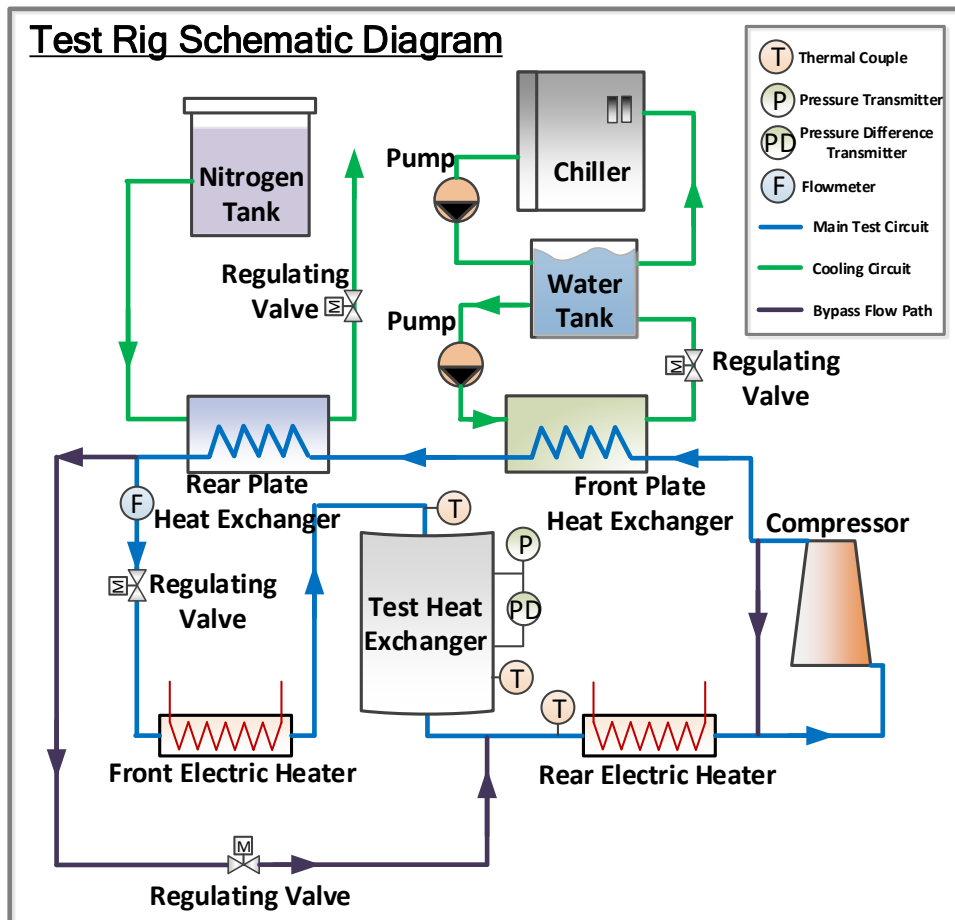
*Table A.1. – Lab experiment parameters and constraints*

### *SWHE geometry*

The CFD model is based on the lab experiments and uses similar dimensions as used in the lab.

Part	Dimension
<b>Tube diameter</b>	12 mm
<b>Pipe wall thickness</b>	1 mm
<b>Vertical distance between tube centers</b>	14
<b>Winding angle</b>	8°
<b>Radial distance of tubes</b>	16mm

*Table A.2 Lab Heat exchanger geometries*



The test rig is consisted of main test circuit, cooling circuit and bypass flow path.

The main test circuit is highlighted by blue line. It is consisted of compressor, plate heat exchanger, regulating valve, electric heater and test heat exchanger. The temperature of the working fluid coming out from the compressor is around 90 to 120°C. Then the working fluid is cooled by the front plant heat exchanger and the rear plate heat exchanger which will make the fluid reach a temperature range from -35 to -160°C. Then the subcooled working fluid go through the regulating valve to reduce pressure and temperature. After heated by the front electric heater to get the test conditions of the temperature and quality, the working fluid will go into the test heat exchanger to do the measurement of the heat transfer coefficient and the frictional pressure drop. Then the working fluid will be heated to superheat state to go back to the compressor.

There are 2 cooling circuits which are highlighted by green line. One is chilled water cooling circuit and the other is liquid nitrogen cooling circuit. The chilled water cooling circuit will refrigerate the working fluid to -35°C and the liquid nitrogen cooling circuit will refrigerate the working fluid to -160°C.

The bypass flow paths are highlighted by purple line. One is compressor bypass flow path and the other is main test bypass flow path. The functions of them are to regulate the working fluid's mass flow rate in the main test circuit.

## Appendix B.1 – Tables and results Propane @ 3 bar saturation point

Diameter of the tubes in the bundles are 12mm. Radial distance is 16 mm which leaves a 4mm gap between the tubes side by side each other in horizontal direction. All tubes are arranged in a square, in-line arrangement. Two different vertical tube spacing cases tested for 13 mm and 16mm, (1mm or 4mm vertical tube gap)

### Geometry: 1mm vertical tube spacing

In the right is the percentage over predicted difference from the Feenstra prediction model used in the inlet and the measured volumetric and cross sectional void fractions respectively. The light yellow shows a good result, while red is unacceptable result.

Color code on measured table data:

Green color code is Falling film flow (FF), orange color code is Intermittend flow (IN) and red color code is vapor Shear flow/Spray flow (SH).

Massflux G10											
Measured					Prediction						
Quality	Vol. Void fraction	Cross s. Vol Fr.	S	Film [mm]	Feenstra	Homogeneous	S				
0.1	0.791	0.713	4.9	0.19	0.516	0.901	8.5	53	38		
0.2	0.811	0.757	6.9	0.17	0.663	0.953	10.4	22	14		
0.4	0.849	0.762	23.9	0.09	0.807	0.982	13.0	5	-6		
0.7	0.847	0.772	40.8	0.04	0.923	0.995	15.9	-8	-16		

Massflux G20											
Measured					Prediction						
Quality	Vol. Void fraction	Cross s. Vol Fr.	S	Film [mm]	Feenstra	Homogeneous	S				
0.1	0.736	0.737	3.8	0.26	0.606	0.901	5.9	21	22		
0.2	0.801	0.773	6.2	0.19	0.737	0.953	6.2	9	5		
0.4	0.840	0.738	23.1	0.12	0.855	0.982	9.3	-2	-14		
0.7	0.836	0.734	93.9	0.06	0.944	0.995	11.4	-11	-22		

Massflux G30											
Quality	Measured					Prediction			S	S	S
	Vol. Void fraction	Cross s. Vol Fr.	S	Film [mm]	Feenstra	Homogeneous	S				
0.01	0.628	0.593	0.72	0.35	0.207	0.453	3.2	203	30.9		
0.05	0.664	0.596	2.7	0.35	0.516	0.812	4.1	29	-27		
0.1	0.712	0.645	4.9	0.28	0.651	0.901	4.9	9	-28		
0.2	0.774	0.712	10.1	0.17	0.773	0.953	6.0	0	-25		
0.4	0.864	0.884	12.4	0.06	0.877	0.982	7.7	-2	-10		
0.7	0.965	0.994	4.8	NA	0.953	0.995	9.5	1	0		

Massflux G40											
Quality	Measured					Prediction			S	S	S
	Vol. Void fraction	Cross s. Vol Fr.	S	Film [mm]	Feenstra	Homogeneous	S				
0.1	0.706	0.659	4.9	0.28	0.680	0.901	4.3	4	-3		
0.2	0.719	0.777	2.8	0.18	0.795	0.953	5.3	-10	-2		
0.4	0.880	0.829	48.6	0.04	0.89	0.982	6.7	-1	-7		
0.7	0.964	0.993	3.1	NA	0.958	0.995	8.3	1	4		

Massflux G50											
Quality	Measured					Prediction			S	S	S
	Vol. Void fraction	Cross s. Vol Fr.	S	Film [mm]	Feenstra	Homogeneous	S				
0.1	0.685	0.631	5.6	0.26	0.701	0.901	3.9	-2	-10		
0.2	0.787	0.728	10.1	0.15	0.81	0.953	4.8	-3	-10		
0.4	0.905	0.948	40.3	0.03	0.899	0.982	6.1	1	5		
0.7	0.917	0.990	5	NA	0.962	0.995	7.5	-5	3		

Volumetric void fraction measurement						
Quality/G	10	20	30	40	50	100
0.01			0.628			
0.05			0.664			
0.1	0.791	0.736	0.712	0.706	0.685	0.671
0.2	0.811	0.801	0.774	0.719	0.787	
0.4	0.849	0.840	0.864	0.880	0.905	
0.7	0.847	0.836	0.965	0.964	0.917	

Color intensity related to high void fractions

Cross sectional void fraction measurements						
Quality/G	10	20	30	40	50	100
0.01			0.593			
0.05			0.596			
0.1	0.713	0.737	0.645	0.659	0.631	0.569
0.2	0.757	0.773	0.712	0.777	0.728	
0.4	0.762	0.738	0.884	0.829	0.948	
0.7	0.772	0.734	0.994	0.993	0.990	

Averaged Slip ratios S Measured						
	10	20	30	40	50	100
0.01			0.723			
0.05			2.7			
0.1	4.9	3.8	4.9	4.9	5.6	4
0.2	6.9	6.2	10.1	2.8	10.1	
0.4	23.9	23.1	12.4	48.6	40.3	
0.7	40.8	93.9	4.8	3.1	5	

Color coded by Green: Falling Film flow, Orange: Intermittent flow and Red: Spray flow

Film thickness @ lower tube 90°						
	10	20	30	40	50	100
0.01			0.35			
0.05			0.35			
0.1	0.19	0.26	0.28	0.28	0.26	0.35
0.2	0.17	0.19	0.17	0.18	0.15	
0.4	0.09	0.12	0.06	0.04	0.03	
0.7	0.04	0.06	NA	NA	NA	

% difference Vol. Void fraction and Feenstra						
Quality/G	10	20	30	40	50	100
0.01			203.2			
0.05			28.7			
0.1	53.4	21.5	9.4	3.8	-2.3	-11.1
0.2	22.3	8.7	0.1	-9.6	-2.8	
0.4	5.2	-1.8	-1.5	-1.1	0.7	
0.7	-8.3	-11.5	1.3	0.7	-4.6	

Color coded by percentage deviation from simulated and feenstra model predicted values

**Geometry 4mm vertical tube spacing**

Massflux G20											
Measured					Prediction						
Quality	Vol. Void fraction	Cross s. Vol Fr.	S	Film [mm]	Feenstra	Homogeneous	S				
0.1	0.803	0.831	2.1	0.266	0.476	0.901	10	69	75		
0.2	0.841	0.866	4	0.171	0.629	0.953	12.1	34	38		
0.4	0.865	0.867	10.2	0.102	0.784	0.982	15	10	11		
0.7	0.875	0.939	9.3	0.03	0.913	0.995	18.2	-4	3		